MARINE PROPELLERS IN UNSTEADY FLOW

by

DAVID P. KEENAN

B.S., Worcester Polytechnic Institute (1976)
S.M., Massachusetts Institute of Technology (1985)

SUBMITTED TO THE DEPARTMENT OF OCEAN ENGINEERING
IN PARTIAL FULFILLMENT OF THE REQUIREMENTS
FOR THE DEGREE OF

DOCTOR OF PHILOSOPHY
at the
MASSACHUSETTS INSTITUTE OF TECHNOLOGY

May 1989

Signature of Author ______________________________
Department of Ocean Engineering
1 June 1989

Certified by ______________________________
Justin E. Kerwin
Thesis Supervisor

Accepted by ______________________________
A.Douglas Carmichael
Chairman, Department Committee on Graduate Students

MARINE PROPELLERS IN UNSTEADY FLOW

by

DAVID P. KEENAN

Submitted to the Department of Ocean Engineering
on 1 June 1989 in partial fulfillment of the
requirements for the Degree of Doctor of Philosophy in
Fluid Mechanics

ABSTRACT

A vortex lattice lifting surface model is developed and applied to the analysis of marine propellers in both steady and unsteady flow. The model employs Lan's so-called quasi-continuous method to capture more accurately the square-root character of the lifting surface's loading. A vortex wake model is incorporated which allows for spanwise vorticity resulting from the time varying blade loading. Local self-induction of the finite-core tip vortices is included. Vortex amalgamation is used to avoid the difficulties connected with representing the detailed structure of the sheet rollup.

Measurements of the instantaneous geometry of the tip vortices from a propeller operating in a nonuniform flow field are described. The techniques of laser doppler anemometry are employed to map the vortex structures.

The code which implements the numerical model, called PUF5, is exercised with four problems. First, comparison is made to unsteady propeller thrust and side force measurements with good agreement. Second, calculations are made of the wake geometry corresponding to the tip vortex measurements reported here. Finally, PUF5 is applied to the problem of a helicopter rotor in hover.

Thesis Supervisor: Prof. Justin E. Kerwin
Title: Professor of Naval Architecture

Acknowledgements

Many people contributed to the progress of this work, some in the obvious way of offering technical counsel at critical points, but most in a more subtle fashion. There are many highs and lows during the evolution of a project such as this. The knowledgeable, friendly and enthusiastic support of my thesis committee — Professors Justin E. Kerwin, Earll M. Murman and Dick K. P. Yue was especially appreciated when things got tough. The spirited and collegial atmosphere created by the members of the Propeller Group — Dr. Spyros Kinnas, Mr. S. Dean Lewis, Dr. Jin-Tae Lee, Dr. Jean-Luc Guermond, William Coney, Ching-Yeh Hsin and Neal Fine made trying out unformed ideas fun if sometimes humbling.

I extend special thanks to Dr. Wei-Zin Shih whom I count as a valued colleague and my close friend. Our countless long and wide-ranging talks sharpened my understanding of many things.

Support for this research was provided by the MIT Sea Grant College Program and the David Taylor Research Center, Department of the Navy, grant number NA86AA-D-SG089, project R-T-24, Hydrodynamics of Marine Propulsors.

The CRAY X/MP and Y/MP at the Pittsburgh Supercomputer Center were used for a number of the larger calculations.

Joan and Marion showed me the wonder of learning. Walter and Ted taught me the value of a thing done well. Finally, Katie and Ruth are, simply, my *raison d'être.*

Contents

List of Figures

List of Tables

Chapter 1

Introduction

This work addresses the need to understand the unsteady behavior of marine propellers and, in particular, the vortex wake structures they produce. The flow regime in which the typical marine propeller operates is highly nonuniform. The propeller is located in close proximity to the ship's hull. Figure 1.1 shows a typical stern configuration. The flow field around the hull provides a nonaxisymmetric inflow to the propeller which is often quite pronounced in its variation around the propeller disc. As an example, the wake in Figure 1.2 is characteristic of a large, single screw commercial ship. The severe unsteadiness this will present to the propeller is apparent in the $\sim 70-80$ percent wake defect near zero degrees.

The ship's wake is not the only cause of nonuniformity in the flow to the propeller. There will often be struts to support the propeller shaft. These cause local deformations in the velocity field, particularly if they are acting as lifting devices as well as supports. There may be an inclination of the shaft to the main flow either because of the design or, transiently, such as during a maneuver. Multistage devices such as pre-swirl stators and vane wheels (e.g., the so-called Grim wheel) are now being used more frequently. Counter-rotating propellers are also of current interest. The downstream stage in these arrangements encounters multiple localized wake defects from the upstream blades.

From these complicated environments, the naval architect and marine engineer will

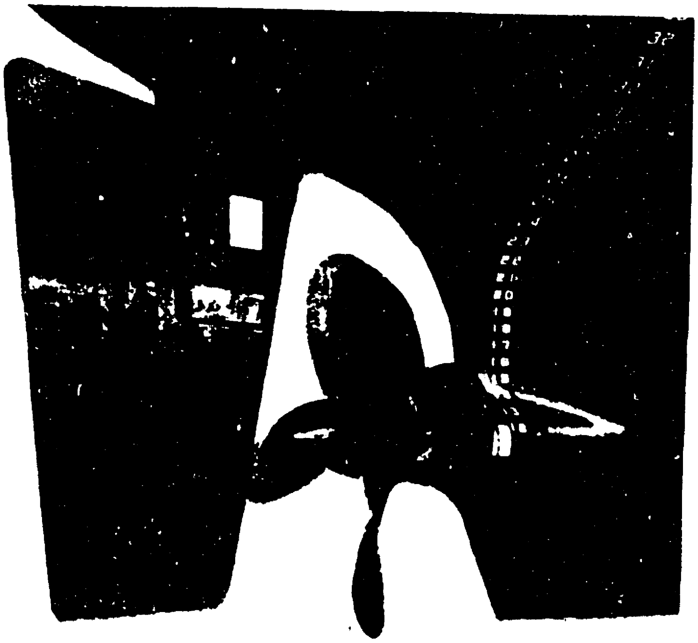

Figure 1.1: Typical geometry of propeller installation.

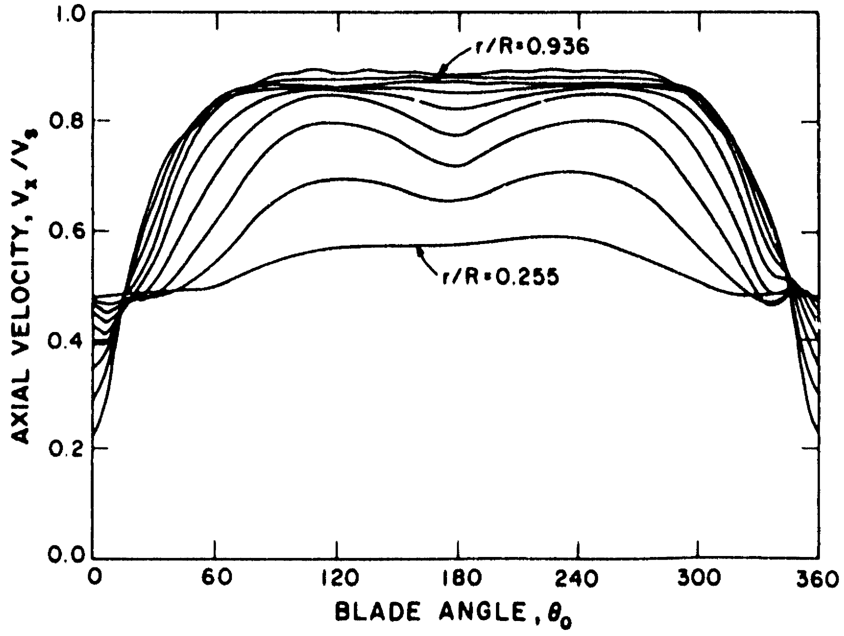

Figure 1.2: Wake distribution of RoRo ship.

typically want to know the magnitudes of the unsteady forces as input to fatigue strength studies of the propellers' blades as well as for the thrust and journal bearings. The environmental consequences of unsteadiness must also be considered. Various regulatory bodies place limits on noise levels within the ship. The noise may be transmitted from the propeller as machinery vibration. It may also arise from cavitation on the propeller and be transmitted through the water and hull surface. In all of these phenomena, the interaction of the vortex wake with downstream structures, including other blades on the same propulsor stage, must be understood.

It can be imagined from the forgoing that the accurate analysis of marine propellers in unsteady flow is a complicated problem which will provide engineers with tests of their skills for many years to come. Nevertheless, there have been some significant advances in the last twenty-five years. Most of these advances have been brought about by the application of increasingly powerful computers to numerical propeller models of growing sophistication.

1.1 Momentum Theory

Marine propellers of the screw type have been in use for over a hundred years. Rankine [66] probably was the first to give a legitimate analysis of their function. He was followed some years later by Greenhill [23] and Froude [16]. These were so-called momentum theories or actuator disk theories. A more accessible presentation of the essentials of the theory can be found in Milne-Thomson [52].

1.2 Lifting Line Theory

Around the turn of the century the work by Helmholtz and Kelvin on vortex flows was introduced into propeller analysis. Theories treating the blades of propellers as lifting devices are said to have their foundation in Lanchester's vortex theory of flight

[43]. While not specific to propellers, this is the first known work to invoke the concept of circulation in connection with lifting bodies. Milne-Thomson notes that Lanchester presented this work in 1894.

The "German school" of Joukowski, Prandtl, Kutta, von Mises and others established this lifting line construct on more solid mathematical footing. Circulation theory found its way to propeller analysis in works by Betz, Glauert, Lerbs and others [6,5,18,47,19]. With some elaborations, these theories dominated propeller design and analysis until very recently. In fact, they are still the basis of even the newest preliminary design techniques such as in [35] by Kerwin, Coney and Hsin.

1.3 Lifting Surface Theory

The germ of lifting surface theory can be seen in much of the work mentioned above but its application had to wait for the arrival of the modern computer. Strscheletzky and Guilloton presaged this movement but had to work their calculations on hand calculators [73,25]. Sparenberg presented a theory of lifting surfaces [72] in 1959. This was programmed later for computer. Modern numerical propeller lifting surface theory begins in 1961 with Kerwin [34] and Pien [63] who were quickly followed by Cox, English and Nelson [10,13,59]. An unsteady lifting surface theory for propellers was first put forward in 1968 by Tsakonas, Jacobs and Rank [77] using an acceleration potential approach. The linearized problem was treated in the frequency domain. *A priori* knowledge of the wake geometry is required. Tsakonas, Breslin and Jacobs [76] have extended the method to permit perturbations of the wake geometry from the linearized position.

In 1978, Kerwin and Lee published a signal work in modern propeller analysis [36]. The blades and wake sheets were represented by vortex lattices. Rollup of the vortex wake into hub and tip vortices was modelled. Both steady and unsteady motions were considered. The code derived from that work, PUF2, has been very successful and serves as a baseline against which other codes are compared. The PUF2 model was extended to incorporate unsteady cavitation by Lee [45]. That code, called PUF3, has also been well received.

1.4 Free Wake Models

It was understood from the beginning that the vortex wake shed behind a lifting surface has a prominent role in the hydrodynamics of the problem. All of the propeller lifting line analyses assumed that the vortices shed from the lifting surface are convected downstream along constant radius and pitch helices. Indeed, until Kerwin and Lee's 1978 paper all lifting surface models made those same assumptions. The "lifting-liners" knew that the pitch of the vortices was not constant but the nonlinear coupling of the wake geometry with the loading on the lifting surface prevented any direct analytical attack on the problem. Significant progress had to await the development of the modern computer.

Nevertheless, the problem of predicting the ultimate confguration of a lifting body's vortex wake was of sufficient interest that as early as 1935 Westwater [78] attempted to compute the Trefftz plane structure of the vortex sheet behind an elliptically loaded wing. He discretized the sheet into a small number of point vortices and then integrated their motions due to mutual induction by hand calculation. The results were plausible but fortuitous. The small number of vortices and the short time interval of their motion cloaked the chaotic behavior which was later observed when Takami [74] and Moore [53] repeated the calculation.

These first few efforts have bred an entire industry of "vortex chasers". The body of work associated with this field is enormous and cannot be completely reviewed here. For those interested, two reviews of the literature can be especially recommended. These are by Hoeijmakers and Fokkerweg [27] and Sarpkaya [68]. The reader will find several hundred references in those works.

The classical problems in the field of free wake analysis are three. One is the Westwater problem of computing the Trefftz plane structure of the wake from a lifting line with a specified steady load. Besides Westwater, Takami, and Moore, the problem has been examined by Chorin and Benard [9], Fink and Soh [15], and Krasny [39]. Another classical problem is leading edge vortex sheet separation. Here one wishes to compute the trajectory of the vortex sheet which comes off the swept leading edge of a delta-wing lifting surface. The details of the sheet roll-up close aboard the delta wing greatly affect its lift characteristics. An unsteady variant of this is also reported by McCune and Tavares [51]. Vortex shedding from bluff bodies, such as from the bilges of ship hulls, is closely related to this problem in that one must model fairly well developed vortices in close proximity to the body. Faltinsen and Pettersen [14] describe a method which they have applied to a number of problems of interest to naval architects.

These problems, while appearing different at first, share the common feature that they may, with suitable assumptions, be treated as two-dimensional. The third type of problem requires the computation of vortex wake evolution in fully three-dimensional circumstances. A typical problem falling into this category is predicting the transient forces and moments on complete airframes during maneuvers, such as reported by Katz and Maskew [31]. Helicopter aerodynamics is another field rich with applications that require fully three dimensional treatment. Graber and Rosen [21] have looked at rotors in hover. Morino and Bharadvaj [56,57] and Morino, Kaprielian and Sipcic [58] have developed a comprehensive potential based panel method applicable to rotors in general maneuvers. Katz and Maskew also applied their methods to the helicopter rotor in hover.

The earliest free wake analysis applied to marine propellers was in 1968 by Cummings [11]. He was able to compute the steady geometry of a propeller's tip vortex. The propeller was represented as a lifting line. Gradients in the streamwise direction were assumed to be small so that the problem could be transformed into an unsteady one in two dimensions. Cummings' calculated values for the tip vortex' radial position agreed well with observations. He also attempted to implement a fully three dimensional wake relaxation scheme for a lifting line wing but at that early date the computational burden was deemed to be excessive.

Greeley and Kerwin [22] developed a semi-free wake model for propellers in steady flow. In their work, radial positions for the trailing vortices are prescribed. The pitch is then obtained from requiring that the vortices line up with the local axial and tangential components of the flow. By using clever interpolation of induced velocities along with assigned parameters to describe the radial distribution of the wake, they were able to keep the computational effort small enough so that the model could be implemented in an interactive design method.

In the remainder of this work a model of marine propellers is developed which incorporates the nonlinear behavior of the vortex wakes. A vortex lattice numerical model is chosen. Such a representation is desirable for several reasons. Experience with similar models shows them to be robust. They have good convergence properties; thus, fairly accurate results can be obtained with reasonable computational effort. Earlier codes developed at MIT use similar representations so extending the current code to handle cavitation and ducted propellers can be done from a familiar foundation.

Chapter 2

Lifting Surface Theory for Marine Propellers

The purpose of this chapter is to place the vortex lattice representation of marine propellers on a rational basis. In the development which follows, three key components of the flow will be examined. The first aspect of the problem which needs to be considered is the rotational nature of the flow. As noted in Chapter 1, the model of the propeller and wake will depend fundamentally on potential theory so the rotational part of the flow must be separated out. Next, representation of the propeller and wake in terms of vortex segments lying on their surfaces will be derived. This will follow in a natural way from consideration of Green's 2^{nd} Identity. Lastly, the rules governing the evolution of the wake vorticity will be established. After this development, some ancillary formulae will be derived in order that forces may be computed.

2.1 Inflow to the Propeller

To begin, it is assumed that the fluid is incompressible and inviscid (except insofar as viscosity is required to produce the lifting phenomena of interest), that only one phase of the fluid is present (i.e. cavitation is ignored) and that the domain is unbounded. A fluid flow meeting these assumptions obeys the vorticity equation

$$\frac{\partial \omega}{\partial t} + \mathbf{V} \cdot \nabla \omega = \omega \cdot \nabla \mathbf{V}. \tag{2.1}$$

The vorticity can be thought of as arising from two sources: that generated at the surfaces in the flow, especially, on the lifting body, and that carried into the region of interest from elsewhere. The vorticity from the lifting surface will be confined to thin sheets with dimensions comparable to the boundary layer thickness on the body. The vorticity transported from upstream into the region of interest will generally be diffuse and weak relative to the body's vortex wake. It comes from the boundary layer of the ship's hull. These observations motivate the following development.

Divide the flow into two parts so that

$$\mathbf{V} = \mathbf{v}_1 + \mathbf{v}_2$$

for which

$$\omega_n = \nabla \times \mathbf{v}_n, \qquad n = 1, 2.$$

Then

$$\begin{aligned} \frac{\partial \omega_1}{\partial t} + \mathbf{v}_1 \cdot \nabla \omega_1 - \omega_1 \cdot \nabla \mathbf{v}_1 &= -\frac{\partial \omega_2}{\partial t} - \mathbf{v}_1 \cdot \nabla \omega_2 - \mathbf{v}_2 \cdot \nabla \omega_1 - \mathbf{v}_2 \cdot \nabla \omega_2 \\ &\quad + \omega_1 \cdot \nabla \mathbf{v}_2 + \omega_2 \cdot \nabla \mathbf{v}_1 + \omega_2 \cdot \nabla \mathbf{v}_2. \end{aligned} \tag{2.2}$$

The velocity field $\mathbf{v}_2$ represents the background flow which is assumed to satisfy

$$\frac{\partial \omega_2}{\partial t} + \mathbf{v}_2 \cdot \nabla \omega_2 = \omega_2 \cdot \nabla \mathbf{v}_2. \tag{2.3}$$

That being the case, the perturbation flow must satisfy

$$\begin{aligned} \frac{\partial \omega_1}{\partial t} + \mathbf{v}_1 \cdot \nabla \omega_1 - \omega_1 \cdot \nabla \mathbf{v}_1 &= -\mathbf{v}_1 \cdot \nabla \omega_2 - \mathbf{v}_2 \cdot \nabla \omega_1 \\ &\quad + \omega_1 \cdot \nabla \mathbf{v}_2 + \omega_2 \cdot \nabla \mathbf{v}_1. \end{aligned} \tag{2.4}$$

Let Γ be some measure of the circulation on the propeller blade, U_0 be a measure of the background flow velocity, Δ be a length scale which characterizes the spacial extent of the background vorticity *c.g.*, the width of the viscous dent of the ship's wake, and δ measure the thickness of the vortex sheet from the propeller. If the terms in equation (2.4) are estimated by these quantities, the following ratios may be formed

$$\begin{aligned}
\frac{|\mathbf{v}_1 \cdot \nabla\boldsymbol{\omega}_2|}{|\mathbf{v}_1 \cdot \nabla\boldsymbol{\omega}_1|} &\approx \left(\frac{\delta}{\Delta}\right)^2 \frac{\delta}{\Gamma}U_0 \\
\frac{|\mathbf{v}_2 \cdot \nabla\boldsymbol{\omega}_1|}{|\mathbf{v}_1 \cdot \nabla\boldsymbol{\omega}_1|} &\approx \frac{\delta}{\Gamma}U_0 \\
\frac{|\boldsymbol{\omega}_1 \cdot \nabla\mathbf{v}_2|}{|\mathbf{v}_1 \cdot \nabla\boldsymbol{\omega}_1|} &\approx \left(\frac{\delta}{\Delta}\right) \frac{\delta}{\Gamma}U_0 \\
\frac{|\boldsymbol{\omega}_2 \cdot \nabla\mathbf{v}_1|}{|\mathbf{v}_1 \cdot \nabla\boldsymbol{\omega}_1|} &\approx \left(\frac{\delta}{\Delta}\right) \frac{\delta}{\Gamma}U_0 \ .
\end{aligned}$$

Retaining terms to $o(U_0\delta/\Gamma)$ reduces equation (2.4) to

$$\frac{\partial\boldsymbol{\omega}_1}{\partial t} + \mathbf{v}_1 \cdot \nabla\boldsymbol{\omega}_1 = \boldsymbol{\omega}_1 \cdot \nabla\mathbf{v}_1 - \mathbf{v}_2 \cdot \nabla\boldsymbol{\omega}_1$$

or

$$\frac{\partial\boldsymbol{\omega}_1}{\partial t} + \mathbf{V} \cdot \nabla\boldsymbol{\omega}_1 = \boldsymbol{\omega}_1 \cdot \nabla\mathbf{v}_1. \tag{2.5}$$

Equation (2.5) shows that the background flow enters the problem only through the boundary conditions for the perturbation flow, either by modifying the normal velocity on the body or the convection velocities for the wake sheets. The terms that have been dropped represent the stretching and convection of the background vorticity by the perturbation flow. The effective wake problem described by Kerwin [33] and Shih [69] has its origin in these phenomena.

It should be understood that the division of the flow does not necessarily correspond to propeller/wake flow and background flow. It may be that upstream phenomena produce compact regions of vorticity that are carried into the propeller flow as from an upstream lifting device. Although not generated by the propeller, this vorticity would be included in $\boldsymbol{\omega}_1$.

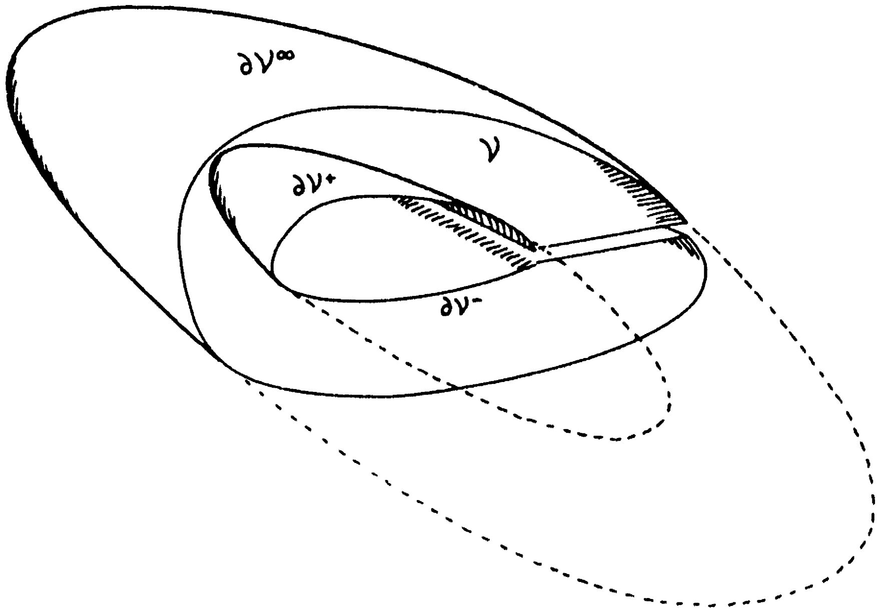

Figure 2.1: General arrangement for the application of Green's 2^{nd} Identity.

2.2 Green's Theorem Formulation for the Perturbation Flow

At large Reynold's numbers, the vorticity generated at the body surface will not propagate out into the flow domain in time scales important to the other aspects of the problem. Thus, the regions where ω_1 is significant are confined to thin layers adjacent to the body surface and trailing downstream from its aft edges. The bulk of the perturbation flow is effectively irrotational. This circumstance permits application of the formalisms of potential theory.

The development of the perturbation problem is begun by considering a volume $\mathcal{V}$ in R^3 with the boundary $\partial\mathcal{V}$. As sketched in Figure 2.1, the boundary is composed of the surface $\partial\mathcal{V}^\infty$ and the surfaces $\partial\mathcal{V}^+$ and $\partial\mathcal{V}^-$. The surfaces $\partial\mathcal{V}^\pm$ are chosen to exclude the rotational regions of the flow from $\mathcal{V}$.

The perturbation flow $\mathbf{v}_1$ in $\mathcal{V}$, being incompressible, inviscid and irrotational is governed by Laplace's equation

$$\nabla^2\varphi = 0 \tag{2.6}$$

with

$$\mathbf{v}_1 = \nabla\varphi. \tag{2.7}$$

The application of Green's 2^{nd} Identity to such an arrangement is classical [4,30,40,55,60]. For a point $\mathbf{x}$ in $\mathcal{V}$ and not on the surface $\partial\mathcal{V}$ it gives

$$-4\pi\varphi(\mathbf{x}) = \int_{\partial\mathcal{V}} \left[\frac{1}{|\mathbf{x}-\boldsymbol{\xi}|}\mathbf{n}(\boldsymbol{\xi})\cdot\nabla_\xi\varphi(\boldsymbol{\xi}) - \varphi(\boldsymbol{\xi})\mathbf{n}(\boldsymbol{\xi})\cdot\nabla_\xi\frac{1}{|\mathbf{x}-\boldsymbol{\xi}|}\right]d\sigma. \tag{2.8}$$

The velocity potential at $\mathbf{x}$, $\varphi(\mathbf{x})$, is produced by the distribution of sources and normal dipoles over the surface $\partial\mathcal{V}$. The gradient ∇_ξ is taken with respect to the source point coordinates $\boldsymbol{\xi}$.

Taking $\partial\mathcal{V}^\infty$ far enough away so that

$$\nabla\varphi \longrightarrow 0 \qquad \text{on } \partial\mathcal{V}^\infty$$

eliminates the contribution to equation (2.8) from the integral over $\partial\mathcal{V}^\infty$. Thus, $\partial\mathcal{V}$ is identified henceforth as being the combination of $\partial\mathcal{V}^+$ and $\partial\mathcal{V}^-$ only. Then, for a point $\mathbf{x}$ on $\partial\mathcal{V}$

$$-2\pi\varphi(\mathbf{x}) = \int_{\partial\mathcal{V}} \left[\frac{1}{|\mathbf{x}-\boldsymbol{\xi}|}\mathbf{n}(\boldsymbol{\xi})\cdot\nabla_\xi\varphi(\boldsymbol{\xi}) - \varphi(\boldsymbol{\xi})\mathbf{n}(\boldsymbol{\xi})\cdot\nabla_\xi\frac{1}{|\mathbf{x}-\boldsymbol{\xi}|}\right]d\sigma. \tag{2.9}$$

Taking the gradient of equation (2.9) with respect to the field point $\mathbf{x}$ results in

$$-2\pi\nabla_x\varphi(\mathbf{x}) = \int_{\partial\mathcal{V}} \left[\nabla_x\frac{1}{|\mathbf{x}-\boldsymbol{\xi}|}\mathbf{n}(\boldsymbol{\xi})\cdot\nabla_\xi\varphi(\boldsymbol{\xi}) - \varphi(\boldsymbol{\xi})\nabla_x\mathbf{n}(\boldsymbol{\xi})\cdot\nabla_\xi\frac{1}{|\mathbf{x}-\boldsymbol{\xi}|}\right]d\sigma \tag{2.10}$$

In the limit of zero body thickness the surfaces $\partial\mathcal{V}^+$ and $\partial\mathcal{V}^-$ coincide and

$$\mathbf{n}^+\cdot\nabla_\xi\varphi^+(\boldsymbol{\xi}) = \mathbf{n}^-\cdot\nabla_\xi\varphi^-(\boldsymbol{\xi})$$

so that

$$-2\pi\mathbf{v}_1(\mathbf{x}) = \int_{\partial\mathcal{V}}(\varphi^+ - \varphi^-)\nabla_x\left[\mathbf{n}\cdot\nabla_\xi\frac{1}{|\mathbf{x}-\boldsymbol{\xi}|}\right]d\sigma. \tag{2.11}$$

Now the integral is restricted to one side of ∂V. The normal velocity at $\mathbf{x}$ is

$$-2\pi \mathbf{n}(\mathbf{x})\cdot \mathbf{v}_1(\mathbf{x}) = \int_{\partial V} \mu(\boldsymbol{\xi})\mathbf{n}(\mathbf{x})\cdot\left[\nabla_x(\mathbf{n}(\boldsymbol{\xi})\cdot\nabla_\xi\frac{1}{|\mathbf{x}-\boldsymbol{\xi}|})\right]d\sigma. \tag{2.12}$$

The bracketted expression represents the velocity induced at $\mathbf{x}$ by a normal dipole at $\boldsymbol{\xi}$. The quantity μ is the potential jump across the surface, equal to $\varphi^+ - \varphi^-$.

The surface ∂V is again split into two parts. The first is the blade surface S_B on which $V\cdot\mathbf{n}$ will be specified and μ is to be determined. The second part is the wake surface S_W on which μ is known as a function of the body's history. Finally, the governing equation to be solved is

$$\begin{aligned}\int_{S_B} \mu(\boldsymbol{\xi})\mathbf{n}(\mathbf{x})\cdot\left[\nabla_x(\mathbf{n}(\boldsymbol{\xi})\cdot\nabla_\xi\frac{1}{|\mathbf{x}-\boldsymbol{\xi}|})\right]d\sigma = \\ -\int_{S_W} \mu_W(\boldsymbol{\xi})\mathbf{n}(\mathbf{x})\cdot\left[\nabla_x(\mathbf{n}(\boldsymbol{\xi})\cdot\nabla_\xi\frac{1}{|\mathbf{x}-\boldsymbol{\xi}|})\right]d\sigma \\ -2\pi\mathbf{n}(\mathbf{x})\cdot\mathbf{v}_1(\mathbf{x})\end{aligned} \tag{2.13}$$

where $\mathbf{n}\cdot\mathbf{v}_1$ is specified on S_B and μ is to be determined.

2.3 Wake Evolution

Because of the interaction of the sharp trailing edge of the body with the fluid's viscosity, a surface of discontinuity will develop behind the body. This surface is S_W referred to in equation (2.13). Mass conservation requires that for an incompressible fluid

$$\mathbf{n}\cdot\mathbf{v}^+ - v_s^+ = \mathbf{n}\cdot\mathbf{v}^- - v_s^- \tag{2.14}$$

where $\mathbf{n}$ is the unit normal to S_W, $\mathbf{v}^\pm$ are the fluid velocities evaluated on one or the other side of S_W and v_s is the velocity of the surface itself. Since obviously

$$v_s^+ - v_s^- = 0 \tag{2.15}$$

it must be that

$$\mathbf{n} \cdot (\mathbf{v}^+ - \mathbf{v}^-) = 0. \tag{2.16}$$

Likewise, conservation of momentum requires

$$\rho(\mathbf{n} \cdot \mathbf{v}^+ - v_s^+)\mathbf{v}^+ + p^+\mathbf{n} = \rho(\mathbf{n} \cdot \mathbf{v}^- - v_s^-)\mathbf{v}^+ + p^-\mathbf{n} \tag{2.17}$$

from which equations (2.15) and (2.16) permit the conclusion that

$$p^+ - p^- = 0. \tag{2.18}$$

There is no pressure jump across the wake sheet. Furthermore, returning to equation (2.17) one finds

$$(\mathbf{n} \cdot \mathbf{v}^+)\mathbf{v}^+ - (\mathbf{n} \cdot \mathbf{v}^-)\mathbf{v}^- - v_s^+\mathbf{v}^+ + v_s^-\mathbf{v}^- = 0 \tag{2.19}$$

or again using (2.15) and (2.16)

$$(v_n - v_s)(\mathbf{v}^+ - \mathbf{v}^-) = 0. \tag{2.20}$$

One conclusion that may be drawn from Equation (2.20) is that $\mathbf{v}^+ - \mathbf{v}^- = 0$. This is the trivial result corresponding to no discontinuity at all. More useful is the alternative that

$$v_n = v_s \tag{2.21}$$

indicating that the sheet moves with the normal component of local velocity.

To complete the development, it is useful to introduce a Lagrangian curvilinear coordinate system, following Morino and Bharadvaj [56]. Imagine a set of curvilinear coordinates defined with reference to the surface S_W. In this coordinate system each fluid particle on S_W is to have constant position, $\boldsymbol{\xi}$: *i.e.*,

$$\frac{\partial \boldsymbol{\xi}}{\partial t} = 0.$$

The base vectors for this coordinate system are given by

$$\mathbf{a}_i = \frac{\partial \mathbf{x}}{\partial \xi^i}, \qquad i = 1, 2, 3, \tag{2.22}$$

where $\mathbf{x}$ is the position of a fluid particle in Cartesian coordinates. Setting $\boldsymbol{\omega}_1 = \omega^i \mathbf{a}_i$ (with summation implied) and recalling from equation (2.5) that

$$\frac{D\boldsymbol{\omega}_1}{Dt} = (\boldsymbol{\omega}_1 \cdot \nabla)\mathbf{v}_1$$

leads to

$$\frac{D}{Dt}(\omega^i \mathbf{a}_i) = \omega^i \frac{\partial \mathbf{v}_1}{\partial \xi^i}.$$

Noting that

$$\frac{D\mathbf{a}_i}{Dt} = \frac{\partial}{\partial t}\left(\frac{\partial \mathbf{x}}{\partial \xi^i}\right) = \frac{\partial \mathbf{V}}{\partial \xi^i}$$

one finds the vorticity must satisfy

$$\mathbf{a}_i \frac{D\omega^i}{Dt} + \omega^i \frac{\partial \mathbf{V}}{\partial \xi^i} = \omega^i \frac{\partial \mathbf{v}_1}{\partial \xi^i} \tag{2.23}$$

or

$$\mathbf{a}_i \frac{D\omega^i}{Dt} = -\omega^i \frac{\partial \mathbf{v}_2}{\partial \xi^i}. \tag{2.24}$$

The right hand side has already been assumed negligible so

$$\frac{D\boldsymbol{\omega}_1}{Dt} \approx 0. \tag{2.25}$$

This is the important result that the vorticity associated with the perturbation is convected as a material property of the fluid particles in S_W. Points in the wake sheet move with the local velocity.

2.4 Tip Vortex Kinematics

The model described thus far represents the vortex wake as a sheet of infinitesimal thickness. Later, this will be discretized into a net of vortex filaments. In general, the

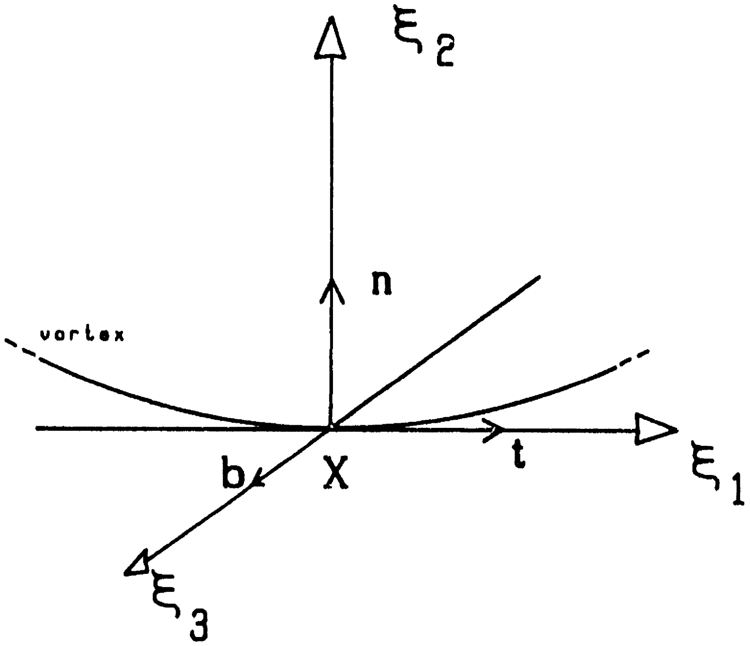

Figure 2.2: The coordinate system for calculating local self induction of a vortex filament.

sheet will be curved, implying that the filaments should be as well. It is well known that a curved vortex filament induces infinite velocities on itself [2,3,4,40,75].

To see the contribution from this self-induction, imagine a local coordinate system to be set up on the filament at the point **X**. As shown in Figure 2.2, the base vectors for this coordinate system are the tangent **t** to the filament's space curve, the normal **n** and the binormal **b**. Let **x** be a point near the filament. Following Batchelor, the local coordinates of the point **x** may be expressed as

$$\mathbf{x} = \xi_2 \mathbf{n} + \xi_3 \mathbf{b}.$$

The position of a point $\boldsymbol{\xi}$ on the filament near **X** is

$$\boldsymbol{\xi} = s\mathbf{t} + \frac{1}{2}\kappa s^2 \mathbf{n}$$

with κ being the curvature of the filament at **X**. Recall Biot-Savart's law for the velocity induced by a vortex filament:

$$\mathbf{v}(\mathbf{x}) = -\frac{\Gamma}{4\pi}\int \frac{\mathbf{r} \times d\mathbf{s}(\boldsymbol{\xi})}{r^3}; \qquad (2.26)$$

$\mathbf{r} = \mathbf{x} - \boldsymbol{\xi}$. Upon substituting the local expressions into equation (2.26) and integrating over a range of $-L \leq s \leq L$ one finds the near field contribution to velocity to be

$$\frac{\Gamma}{2\pi\varepsilon}\boldsymbol{\vartheta} + \frac{\kappa\Gamma}{4\pi}\ln\left(\frac{L}{\varepsilon}\right)\mathbf{b} + O(\varepsilon^0); \tag{2.27}$$

$\varepsilon = |\mathbf{x} - \mathbf{X}|$ and $\boldsymbol{\vartheta}$ is the tangential unit vector in local cylindrical coordinates.

The first term in (2.27), although the more singular, is easily dismissed. Since its induction is anti-symmetric across the filament it is reasonable to conclude that no translation of the filament occurs due to its action. The more important term is the second. This term describes a velocity of the fluid near the filament that is normal to the plane of the filament and symmetric across the filament. A familiar consequence of this term is the motion of a smoke ring along its axis of symmetry. Loukakis [48] showed that it also plays a role in establishing the pitch of the vortex wake from a propeller.

One should note that this term (henceforth called the LIA term for 'local induction approximation') is logarithmically singular. Thus, the velocity of an idealized filament is undefined. The usual procedure for circumventing this difficulty is to assume a finite core size and vorticity distribution for the filament. This approach "desingularizes" the vortex velocity but it requires knowledge of the core size and the instantaneous vorticity distribution. The vortex core size depends on the details of the boundary layer evolution on the propeller blade and its interior vorticity distribution evolves according to the Navier-Stokes equations. The development of the tip vortex from the boundary layer of the propeller blade was studied by Govindan, *et. al.*, [20]. Ting [75] has examined the dynamics of vortex filaments using LIA with an inner Navier-Stokes solution. These are complex calculations in their own right and are beyond the scope of this work. For the purposes of this model it will be sufficient to prescribe a fixed core size. The LIA contribution to the motion of the filament is taken as that at the core radius. The value to set for the core radius will be discussed in the next chapter.

2.5 Boundary Conditions

Because the solution of equation (2.3) was decoupled from that of equation (2.13), $\mathbf{v}_2$ may be considered as known, at least for the time being. The following kinematic boundary conditions may be stated for the perturbation:

$$\mathbf{v}_1 \cdot \mathbf{n} = (\mathbf{U} - \mathbf{v}_2) \cdot \mathbf{n} \qquad \text{on } S_B, \tag{2.28}$$

$$\mathbf{v}_1 \rightarrow 0 \qquad \text{at infinity.} \tag{2.29}$$

where $\mathbf{U}$ is the velocity of the body surface S_B. The conditions on the wake surface have already been described.

2.6 Bernoulli's Equation

While the boundary conditions given above formally complete the statement of the problem, there are still some important details to work out before the problem can be said to be solved in an engineering sense. Once the dipole distribution μ is found, forces on the propeller remain to be computed. For reasons that will be discussed in Chapter 3, these forces will be obtained from integration of the surface pressure distribution. In a purely potential flow, one may obtain pressure immediately from Bernoulli's equation. To obtain Bernoulli's equation one normally assumes that the flow is steady but possibly rotational or unsteady but irrotational as in, *e.g.*, [60]. Here the flow is unsteady and rotational. Without further assumption, it can be show from Euler's equation that pressure satisfies Poisson's equation, [1,62]:

$$\nabla^2 p = -4\pi g. \tag{2.30}$$

The source function g depends on velocities. To obtain pressure from this expression one must supply a set of boundary conditions, solve for velocity throughout the flow domain to obtain the forcing term and then solve equation (2.30). This is an unacceptable amount of computation.

However, a second look at Euler's equation with the specific nature of the flow of interest in mind reveals some useful results. Recall Euler's equation:

$$\frac{\partial \mathbf{V}}{\partial t} + \mathbf{V} \cdot \nabla \mathbf{V} = -\frac{1}{\rho} \nabla p. \tag{2.31}$$

The flow is separated as before into the background flow and a perturbation. The background flow was assumed to be unaffected by the perturbation. Such being the case, it is a small further assumption to say that the background flow is steady, *i.e.*,

$$\frac{\partial \mathbf{v}_2}{\partial t} = 0. \tag{2.32}$$

The vorticity associated with the perturbation flow is assumed to be entirely contained in the boundary layer on the body and in the thin wake sheets. The perturbation flow exterior to these thin layers is irrotational:

$$\nabla \times \mathbf{v}_1 = 0. \tag{2.33}$$

Equation (2.31) becomes

$$\frac{\partial \mathbf{v}_1}{\partial t} + (\mathbf{v}_1 + \mathbf{v}_2) \cdot \nabla (\mathbf{v}_1 + \mathbf{v}_2) = -\frac{1}{\rho} \nabla p. \tag{2.34}$$

By virtue of equation (2.33)

$$\mathbf{v}_1 = \nabla \varphi$$

so

$$\nabla \left[\frac{\partial \varphi}{\partial t} + \frac{p}{\rho} \right] = -\Big(\mathbf{v}_1 \cdot \nabla \mathbf{v}_2 + \mathbf{v}_1 \cdot \nabla \mathbf{v}_1 + \mathbf{v}_2 \cdot \nabla \mathbf{v}_2 + \mathbf{v}_2 \cdot \nabla \mathbf{v}_1 \Big). \tag{2.35}$$

Integrating (2.35) along a streamline produces

$$\frac{\partial \varphi}{\partial t} + \frac{p}{\rho} + \frac{1}{2} \mathbf{V} \cdot \mathbf{V} = C_{\psi}(t). \tag{2.36}$$

The streamline dependence is emphasized by the subscript on C_{ψ}. The final expression for pressure is

$$p - p_a = \frac{1}{2} \rho \Big(\mathbf{V}_\infty \cdot \mathbf{V}_\infty - \mathbf{V} \cdot \mathbf{V} - 2 \frac{\partial \varphi}{\partial t} \Big) \tag{2.37}$$

where p_a is the ambient pressure far enough upstream so that $\partial\varphi/\partial t$ may be assumed small. This differs from the normal Bernoulli equation derived for unsteady, purely potential flow in that the velocities involved are not merely $\nabla\varphi$ but include the contribution from the rotational background flow. Equation (2.37) also differs from Bernoulli's equation for steady rotational flow because of the $\partial\varphi/\partial t$ term.

2.7 Leading Edge Suction

A normal lifting body will have finite thickness and, especially, a rounded leading edge. Pressures acting on the actual body surface give rise to forces which may be resolved into components normal to the body's camber surface and in-plane with it. Local to the leading edge, the surface normal is mostly in-plane with the camber surface. If there is flow around the leading edge there will be a large pressure drop. The combined effect is to produce a significant in-plane force acting on the body at the leading edge. If, as has been done here, the body is idealized as a zero-thickness surface, there can be no in-plane component of force from pressures but this significant contributor to total body forces must be included somehow. These considerations lead to the well known leading edge suction force.

Derivations of this force may be found in many classical references. One such is by Milne-Thomson [52]. The leading edge suction force $\mathbf{F}_S$ is

$$\mathbf{F}_S = -\frac{1}{4}\pi\rho C_S^2\,\mathbf{i} \tag{2.38}$$

where

$$C_S = \lim_{s\to 0}\sqrt{s}\,\gamma(s)\cdot\mathbf{l} \tag{2.39}$$

and $\mathbf{l}$ is a unit vector directed towards the tip along the leading edge, $\mathbf{i}$ is directed streamwise normal to the leading edge and in the surface S_B. The quantity s is the arc length from the leading edge measured along a curve on S_B in the $\mathbf{i}$ direction; γ is the vortex density on S_B.

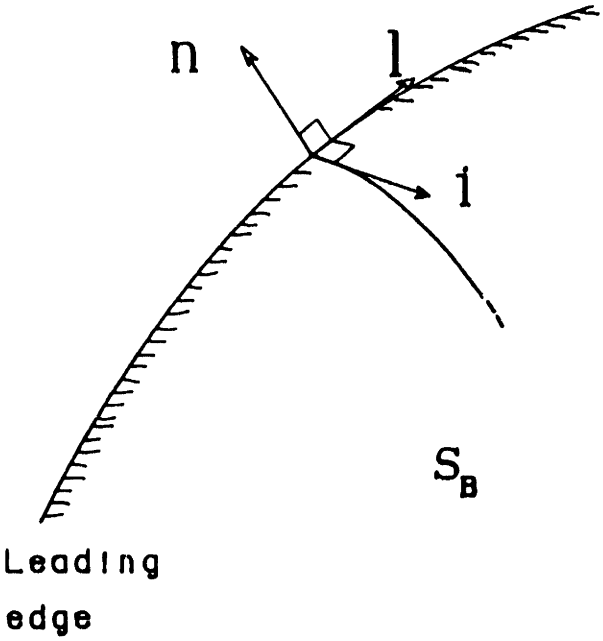

Figure 2.3: Definition of vectors appearing in expressions for leading edge suction.

Chapter 3

Numerical Formulation

This chapter sets out the method by which the equations of Chapter 2 are implemented in discretized form. First, equation (2.13) will be approximated by dipole quadrilateral panels of constant strength. An advantageous arrangement for these panels will be deduced from consideration of the functional form of μ on the blade. The proper location for control points at which $\mathbf{n} \cdot \mathbf{V}$ will be specified will also come out of that discussion. By making a small assumption regarding the flow at the trailing edge, a simple and quick method for the solution of the matrix resulting from the discretized equation (2.13) can be found.

Forces must be computed once the matrix solution is obtained. These will be gotten from integration of pressures on the blades. To complete the calculation of forces equation (2.38) will be expressed in appropriate discretized form. The free-wake model, comprising a vortex lattice representation of the geometry and vorticity distribution of the vortex sheets, will be described. The details of computing induced velocity in the interior of the sheet and on the tip vortices will be developed and a means to control the numerical difficulties associated with rollup will be suggested.

3.1 Propeller Geometry

The geometry of the propeller blades is described in a simple way detailed in [36] and [22]. Figure 3.1 shows how the various quantities are defined. A space curve, the generator line, is described within the blade-fixed Cartesian coordinate system. This is done parametrically by the radial distribution of skew, $\theta_m(r)$, and rake, $x_m(r)$. The blade sections are built-up from this line by specifying the values of pitch angle, $\phi(r)$, chord length, $c(r)$, and camber, $f(r,s)$; s is arc length along the pitch helix measured from the generator line.

Following this procedure, one obtains the coordinates of the leading and trailing edges,

$$\begin{aligned}
x_{l,t} &= x_m \mp \frac{c(r)}{2} \sin\phi(r) && (3.1)\\
\theta_{l,t} &= \theta_m \mp \frac{c(r)}{2r} \cos\phi && (3.2)\\
y_{l,t} &= r\cos\theta_{l,t} && (3.3)\\
z_{l,t} &= r\sin\theta_{l,t}, && (3.4)
\end{aligned}$$

and the coordinates of any point on the camber surface:

$$\begin{aligned}
x_c &= x_m + c(s-1/2)\sin\phi - f\cos\phi && (3.5)\\
\theta_c &= \theta_m + c(s-1/2)\cos\phi + f\frac{\sin\phi}{r} + \delta_k && (3.6)\\
y_c &= r\cos\theta_c && (3.7)\\
z_c &= r\sin\theta_c && (3.8)
\end{aligned}$$

where δ_k gives the angular offset for the k^{th} blade relative to the first (equal spacing is not assumed).

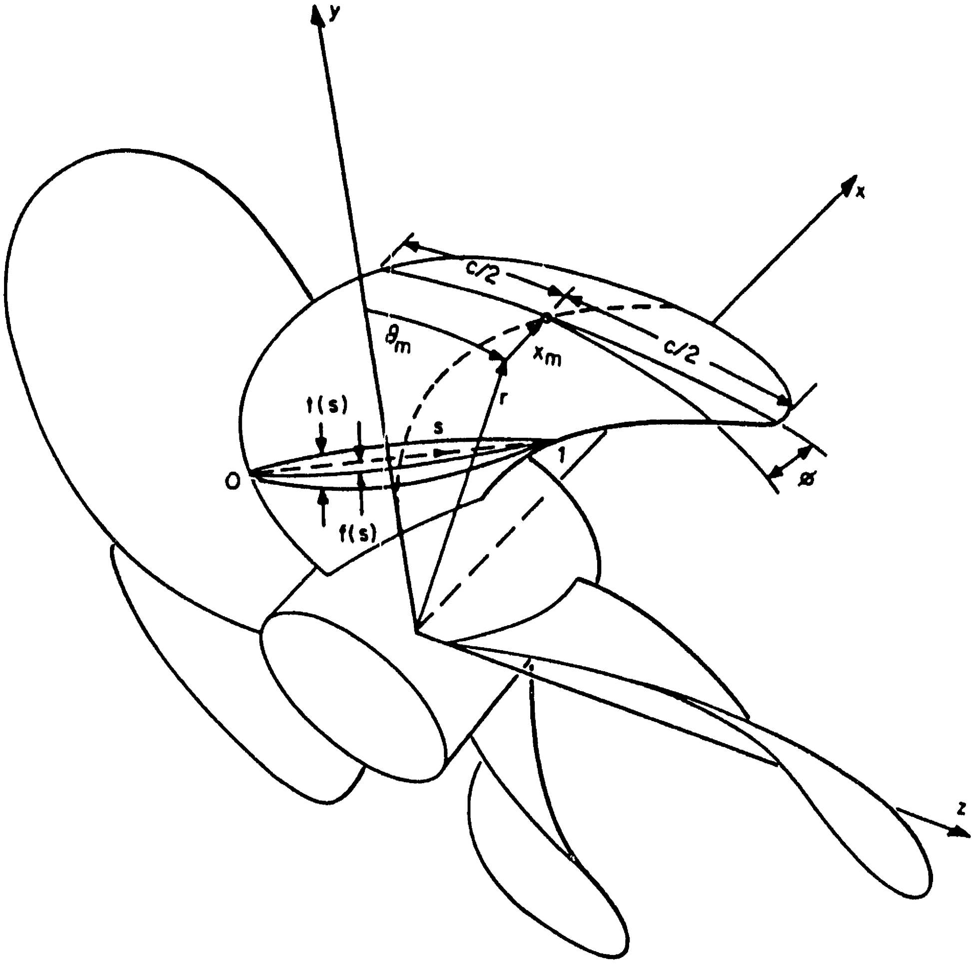

Figure 3.1: Notation for describing blade geometry.

3.2 Discretization of the integral equation

There are two integrals in equation (2.13); one, I_B, over the body surface and one, I_W, over the wake sheets. The integration over the body is

$$I_B = \int_{S_B} \mu(\boldsymbol{\xi})\mathbf{n}(\mathbf{x}) \cdot \left[\nabla_x(\mathbf{n}(\boldsymbol{\xi}) \cdot \nabla_\xi \frac{1}{|\mathbf{x} - \boldsymbol{\xi}|})\right] d\sigma. \tag{3.9}$$

The surface S_B is divided into quadrilateral panels whose vertices are placed on the camber surface according to equations (3.5). The following section will describe how these panels are to be arranged. The details are not important now. Within each panel, the dipole strength μ is assumed to be constant. The integral I_B becomes

$$I_B = \sum_i \mu_i \int_{S_i} \mathbf{n}(\mathbf{x}) \cdot \left[\nabla_x(\mathbf{n}(\boldsymbol{\xi}) \cdot \nabla_\xi \frac{1}{|\mathbf{x} - \boldsymbol{\xi}|})\right] d\sigma. \tag{3.10}$$

The surface S_B is replaced by the collection of surfaces S_i. Each panel has an influence at $\mathbf{x}$ given by the integral in the expression above. This influence coefficient,

$$\int_{S_i} \mathbf{n}(\mathbf{x}) \cdot \left[\nabla_x(\mathbf{n}(\boldsymbol{\xi}) \cdot \nabla_\xi \frac{1}{|\mathbf{x} - \boldsymbol{\xi}|})\right] d\sigma, \tag{3.11}$$

must be evaluated for each panel. It would seem that the shape of the panel would be required to do this. There is a fortunate relationship between dipole and vortex distributions that removes this inconvenience. It can be shown that the following theorem, taken from Lee [46], is true. Referring to Figure 3.2:

> Let S be a surface in R^3 bounded by a simply closed curve C. Suppose this surface to be covered with a distribution of dipoles of strength μ oriented normal to S. Then
>
> $$\begin{aligned}\int_S \mu(\boldsymbol{\xi})\nabla(\mathbf{n}(\boldsymbol{\xi}) \cdot \nabla_\xi \frac{1}{|\mathbf{x} - \boldsymbol{\xi}|}) d\sigma = & \\ & \int_S (\nabla_S \mu(\boldsymbol{\xi}) \times \mathbf{n}(\xi)) \times \nabla \frac{1}{|\mathbf{x} - \boldsymbol{\xi}|} d\sigma \\ & - \oint_C \mu \nabla \frac{1}{|\mathbf{x} - \boldsymbol{\xi}|} \times dl\end{aligned} \tag{3.12}$$

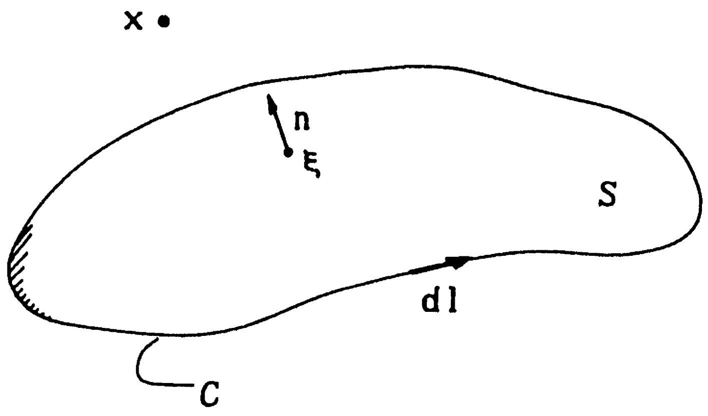

Figure 3.2: General open surface in R^3.

where ∇_S is the surface gradient on S, ∇_ξ is the gradient in R^3 with respect to the source point $\boldsymbol{\xi}$, and ∇ with no subscript is the R^3 gradient with respect to the field point $\mathbf{x}$.

The proof may be found in [46].

In this application, the integral over S on the right side of equation (3.12) vanishes since μ is constant. The remaining integral over C is simply Biot-Savart's law for a vortex filament of strength μ lying along C. Thus, the influence coefficient may be rewritten so that equation (3.10) becomes

$$I_B = \sum_i \mu_i \mathbf{n}(\mathbf{x}) \cdot [\oint \frac{\mathbf{x} - \boldsymbol{\xi}}{|\mathbf{x} - \boldsymbol{\xi}|^3} \times d\mathbf{l}]. \tag{3.13}$$

The integrals over the surfaces S_i have been replaced by path integrals around the perimeters of the panels. The reader should keep this equivalence in mind. Sometimes physical insight is more readily grasped when expressed in terms of one or the other type of singularity so references to dipole panels and vortex loops will be used interchangeably hereafter.

The wake integral can be treated in exactly the same fashion so that equation (2.13) in (semi-)discretized form becomes

$$\begin{aligned}\sum_i \mu_i \mathbf{n}(\mathbf{x}) \cdot \Big[\oint \frac{\mathbf{x}-\boldsymbol{\xi}}{|\mathbf{x}-\boldsymbol{\xi}|^3} \times d\mathbf{l}\Big] = \\ &\sum_j \mu_W \mathbf{n}(\mathbf{x}) \cdot \Big[\oint \frac{\mathbf{x}-\boldsymbol{\xi}}{|\mathbf{x}-\boldsymbol{\xi}|^3} \times d\mathbf{l}\Big] \\ &-2\pi \mathbf{n}(\mathbf{x}) \cdot \mathbf{v}_1(\mathbf{x}).\end{aligned} \tag{3.14}$$

The summation on the left side extends over all panels on the propeller and that on the right extends over all wake panels.

3.3 QCM Panelling

Equation (3.14) was referred to as semi-discretized because collocation points at which $\mathbf{n} \cdot \mathbf{V}$ will be specified are still needed. This has been kept until now because the location of these points is closely linked to the panel arrangement.

At first glance, it would seem reasonable to place collocation points at the centroids of the panels and then to lay out panels to minimize the geometric error — that is, to place more where surface curvature is greatest. This is common practice with potential based panel methods such as in [30,46,55,56]. However, one gets into trouble with velocity based methods if this approach is used. Kerwin and Lee [36] demonstrated that an injudicious placement of the collocation points can badly hamper convergence to an acceptable solution.

In 1974, Lan [42] showed that one must consider more than geometry when laying out panels. The nature of the function to be represented plays at least an equal role. In thin wing problems, the dipole panels are being asked to capture a singularity at the leading edge which behaves like $1/\sqrt{x}$ as $x \rightarrow 0$ in the chordwise direction. In the spanwise direction the loading on the wing goes to zero like $\sqrt{x}$. Lan showed that these features can be captured accurately and the Cauchy singularity in equation (2.13) avoided.

In two dimensions, the downwash at any point on the foil is given by

$$w(x) = \frac{1}{2\pi}\int \frac{\gamma(\xi)d\xi}{x-\xi}. \tag{3.15}$$

The coordinate transformation

$$x = (1-\cos\theta)/2 \tag{3.16}$$

allows the integral in (3.15) to be written as

$$w(\theta) = \frac{1}{2\pi}\int_0^\pi \frac{g(\theta')}{\cos\theta - \cos\theta'}d\theta'. \tag{3.17}$$

where $g(\theta) = \gamma(\theta) sin\theta$. To eliminate the Cauchy singularity, the Glauert integral

$$G_n(\theta) = \int_0^\pi \frac{\cos n\theta'}{\cos\theta' - \cos\theta}d\theta'. \tag{3.18}$$

is introduced. This vanishes for $n = 0$. Adding and subtracting $g(\theta)\,G_0(\theta)/2\pi$ to (3.17) results in

$$w(\theta) = -\frac{1}{2\pi}\int_0^\pi \frac{g(\theta) - g(\theta')}{\cos\theta - \cos\theta'}d\theta'. \tag{3.19}$$

The integrand is now finite so a midpoint trapezoidal integration may be used giving

$$\begin{aligned} \int_0^\pi \frac{g(\theta) - g(\theta')}{\cos\theta - \cos\theta'}d\theta' \quad &\approx \quad \frac{\pi}{N}\sum_{i=1}^{N}\Big[\frac{g((2i-1)\pi/2N)}{\cos\theta - \cos((i-1/2)\pi/N)} \\ &\qquad - \frac{g(\theta)}{\cos\theta - \cos((2i-1)\pi/2N)}\Big]. \end{aligned} \tag{3.20}$$

Equation (3.20) can follow from (3.19) only if $\theta \neq \theta'$. Lan showed that this is ensured and the last term of (3.20), corresponding to the previously inserted Glauert integral, eliminated if θ is chosen equal to θ_j where

$$\theta_j = \frac{j\pi}{N}, \qquad j = 1,2,\ldots,N. \tag{3.21}$$

This places the discrete vortices at x_i and the control points at x_j where

$$x_i = \frac{1}{2}[1-\cos((i-1/2)\pi/N)], \qquad i = 1,2,\ldots,N \tag{3.22}$$

$$x_j = \frac{1}{2}[1-\cos(j\pi/N)], \qquad j = 1,2,\ldots,N. \tag{3.23}$$

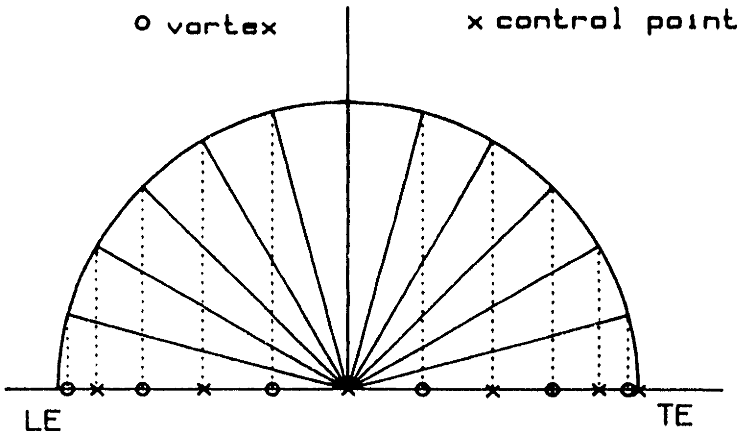

Figure 3.3: Schematic representation of QCM panelling.

This arrangement is commonly referred to as cosine spacing and distinguishes the quasi-continuous method (QCM) from the classical vortex lattice method (VLM) wherein the panels are of equal size and the control points are placed at their midpoints. Figure 3.3 illustrates how equations (3.22) and (3.23) distribute vortices and control points over the chord.

In three dimensions, the QCM is applied in the chordwise direction. In the spanwise direction, there is no square-root singular edge behavior but experience shows that the spanwise circulation often looks elliptical, meaning that a square-root approach to zero can be anticipated. Thus, it seems reasonable to accumulate panels towards the tip. To do this, the "semi-circle" method was suggested by Lan. Lan found that this gave better results than spanwise uniform spacing. Similarly, Kerwin and Lee found it to have excellent convergence properties. It has the added benefit over uniform spanwise spacing of placing panels closer to the tips for a given number of panels thus increasing resolution. Figure 3.4 shows the semi-circle method applied spanwise compared to uniform spacing.

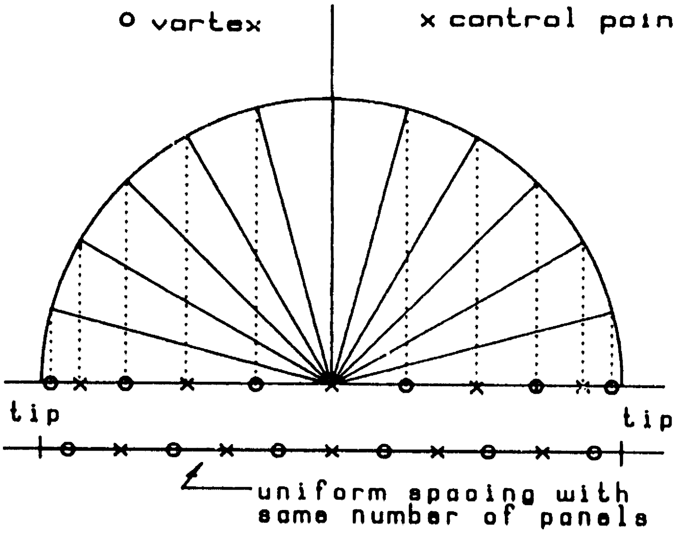

Figure 3.4: Spanwise vortex and control point locations for semi-circle and uniform spacing.

To apply the scheme described above, the grid points which form the vertices of the panels are laid out first. Their radial positions are given by

$$r_m = \frac{1}{2}\Big[(R + r_H) - (R - r_H)\cos(\frac{m - 1/2}{M + 1}\pi)\Big], \qquad m = 1, 2, \ldots, M, \tag{3.24}$$

where M is the number of panels in the spanwise direction. Their chordwise position, s, expressed as a fraction of chordlength from the leading edge, is

$$s_n = \frac{1}{2}\Big[1 - \cos(\frac{n - 1/2}{N}\pi)\Big], \qquad n = 1, 2, \ldots, N, \tag{3.25}$$

where N is the number of panels over the chord. Equations (3.5) are then applied to r_m and s_n to get the actual coordinates of the grid points. Figure 3.5 shows the resulting panel arrangement for one blade of a typical propeller.

The next step is to locate the control points. Their radial locations are given by

$$rp_m = \frac{1}{2}\Big[(R + r_H) - (R - r_H)\cos(\frac{m}{M + 1}\pi)\Big], \qquad m = 1, 2, \ldots, M. \tag{3.26}$$

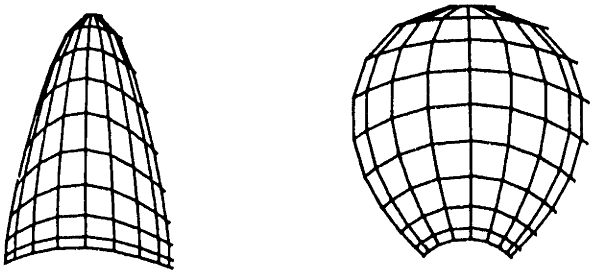

Figure 3.5: QCM panelling on a typical propeller blade.

One must proceed carefully from here. Suppose that the control points are placed by applying equation (3.23) in the chordwise direction. For blades with straight edges there is no problem but for propeller blades which have curved edges this approach leads to disaster. Figure 3.6 shows a detail of the tip region of the blade from Figure 3.5 with the control points placed as described. One immediately notices that some control points are actually outside the panels with which they are associated. Realistic solutions cannot be expected from such an arrangement.

The fault is actually with the panel boundaries and not with the control points. When the blade outline is not rectilinear, straight vortex elements do not lie at the correct chordwise positions except at their endpoints. For normal propeller shapes, the vortices tend to cluster toward the midchord.

There are two possible solutions. One is to use panels with curved edges. This approach was taken by Guermond [24] in his study of the planar circular wing problem. Another approach is to take the straight-edged panelling as correctly defining an "equiv-

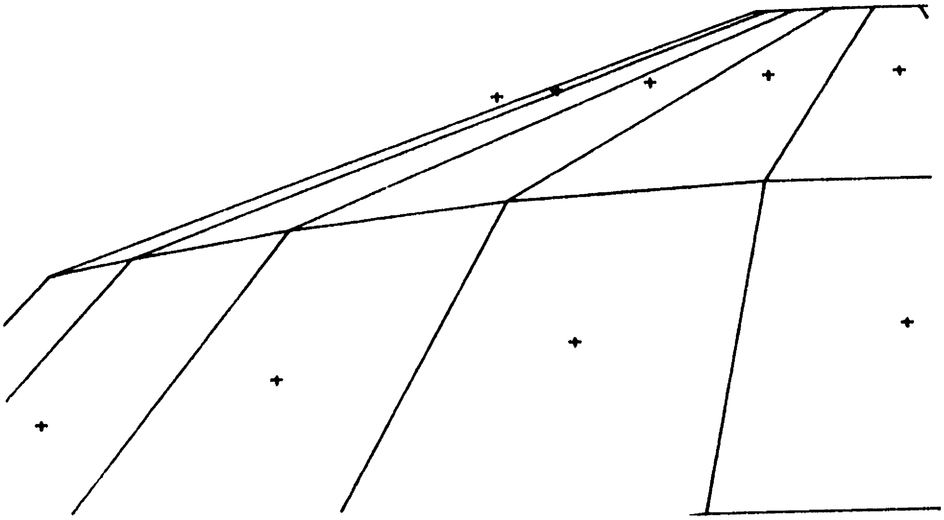

Figure 3.6: Control point locations resulting from direct application of QCM to blades with curved boundaries.

alent" propeller — one with straight, segmented boundaries. The control points for this equivalent propeller may then be placed correctly by interpolating from the grid point locations. Guermond's approach is the more correct and is relatively easy to implement for planar surfaces. An efficient means of computing the influence coefficients for planar panels with curvilinear boundaries has been developed by Canteloube and Rehbach [8] but propellers are notoriously nonplanar so their work isn't applicable here. This work applies the second approach.

Consider a single panel within the grid as shown in Figure 3.7. Its defining grid points are at $\mathbf{x}_{n,m}$, $\mathbf{x}_{n+1,m}$, $\mathbf{x}_{n,m+1}$ and $\mathbf{x}_{n+1,m+1}$. The points $\boldsymbol{\xi}_{n,m+1}$ and $\boldsymbol{\xi}_{n,m}$ are interpolated according to

$$\boldsymbol{\xi}_{n,m} = \mathbf{x}_{n,m} + \frac{s_c - s_n}{s_{n-1} - s_n}(\mathbf{x}_{n+1,m} - \mathbf{x}_{n,m}) \tag{3.27}$$

where $n = 1, 2, \ldots, N-1$, $m = 1, 2, \ldots, M+1$, s_n is from equation (3.25), and s_c, the chordwise QCM control point location, follows from equation (3.23). Additionally, $\boldsymbol{\xi}_{N,m}$ are placed on the trailing edge at r_m.

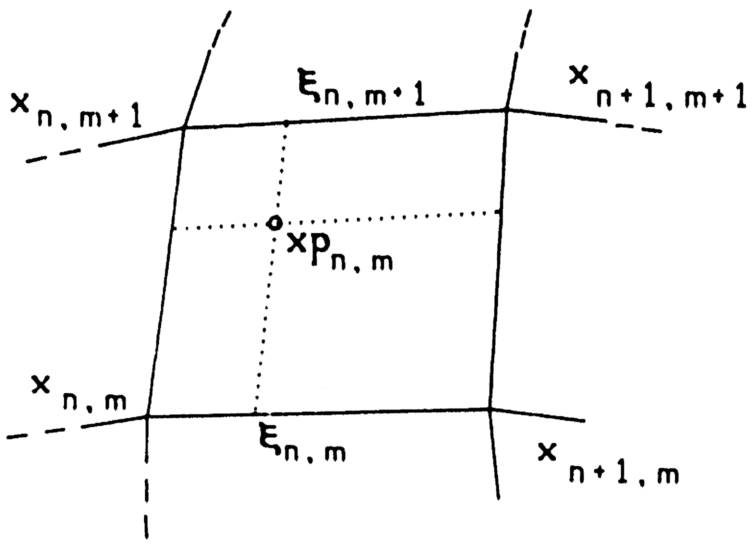

Figure 3.7: Interpolation of the control point location.

The control point coordinates **xp** are then calculated as

$$\mathbf{xp}_{n,m} = \boldsymbol{\xi}_{n,m} + \frac{rp_m - r_m}{r_{m+1} - r_m}(\boldsymbol{\xi}_{n,m+1} - \boldsymbol{\xi}_{n,m}) \tag{3.28}$$

for $n = 1, 2, \ldots, N$ and $m = 1, 2, \ldots, M$. Figure 3.8 shows the same detail as in Figure 3.6 after allowing for the straight panel edges. Figure 3.9 shows a complete view of the same propeller. It is interesting to note that in both [36] and [22] the need to locate the control points with reference to the "equivalent" propeller was appreciated intuitively. Hoshino [29] makes no reference to this issue; the algorithm given would locate the control points incorrectly.

To proceed in the development of the numerical model, consider a streamwise strip of panels on the blade as shown in Figure 3.10. The vortices at adjacent panel edges are shown combined to form single lumped vortices. Each Γ is the sum of two dipole strengths. For example,

$$\Gamma^S_{n,m} = \mu_{n,m} - \mu_{n-1,m}$$

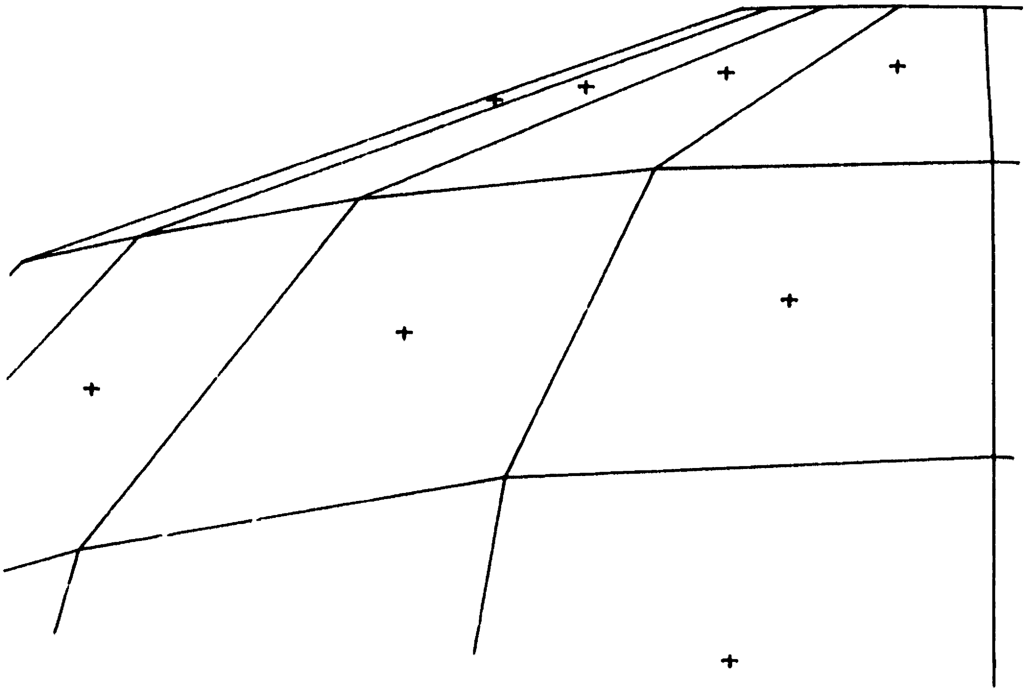

Figure 3.8: Corrected control point locations.

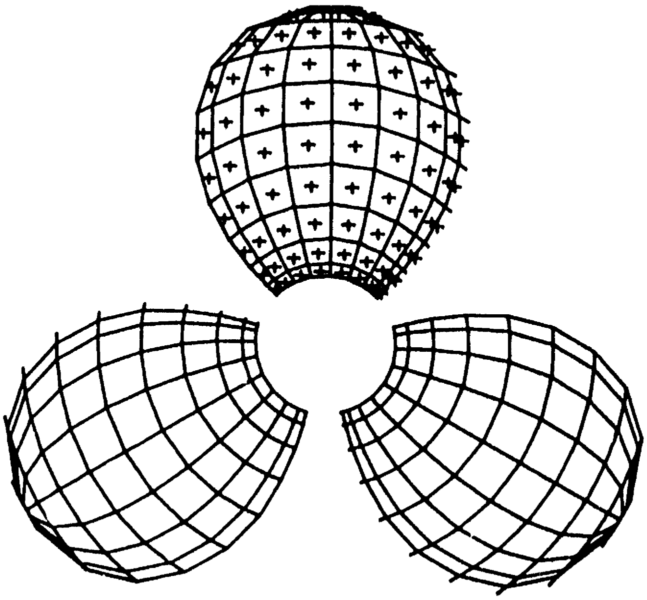

Figure 3.9: QCM panelling with corrected control point locations (control points shown only on one blade for clarity).

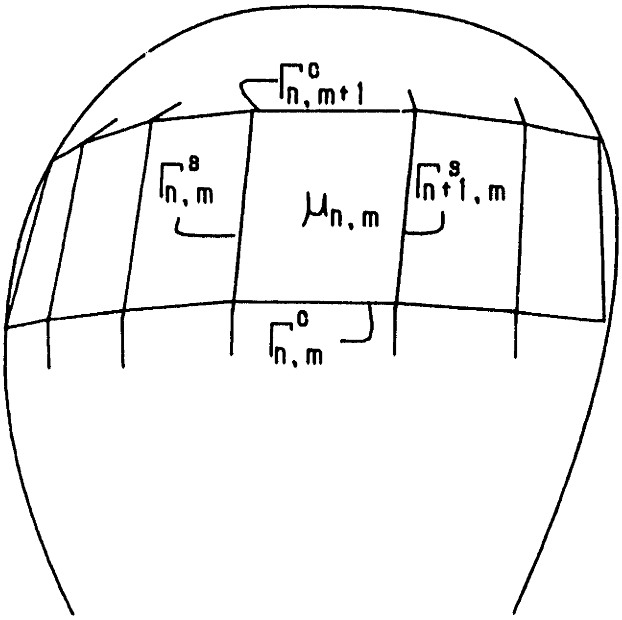

Figure 3.10: Definition sketch of vortex segments associated with panel boundaries.

and

$$\Gamma^C_{n,m} = -\mu_{n,m} + \mu_{n,m+1}$$

where the subscripts n and m refer to the n^{th} panel from the leading edge in the m^{th} strip of panels from the blade root. The quantity denoted by $v^S_{i,n,m}$ is the normal component of velocity induced at the i^{th} control point by a unit strength spanwise vortex. Specifically,

$$v^S_{i,n,m} = \mathbf{n}_i \cdot \int_{\mathbf{x}_{n,m}}^{\mathbf{x}_{n,m+1}} \frac{\mathbf{x}_i - \boldsymbol{\xi}}{|\mathbf{x}_i - \boldsymbol{\xi}|^3} \times d\mathbf{l}. \tag{3.29}$$

In this notation, equation (3.14) may be written as

$$\begin{aligned} -\mathbf{n} \cdot \mathbf{v}_1(\mathbf{x}_i) = \sum_{k=1}^{K} \Bigg[& \sum_{m=1}^{M} \sum_{n=1}^{N} v^S_{i,n,m,k} \Gamma^S_{n,m,k} \\ & + \sum_{m=1}^{M+1} \sum_{n=1}^{N} v^C_{i,n,m,k} \Gamma^C_{n,m,k} \\ & + \sum_{m=1}^{M} \sum_{n=1}^{N_w} v^w_{i,n,m,k} \Gamma^w_{n,m,k} \\ & + \sum_{m=1}^{M+1} \sum_{n=1}^{N_w-1} v^t_{i,n,m,k} \Gamma^t_{n,m,k} \Bigg] \end{aligned} \tag{3.30}$$

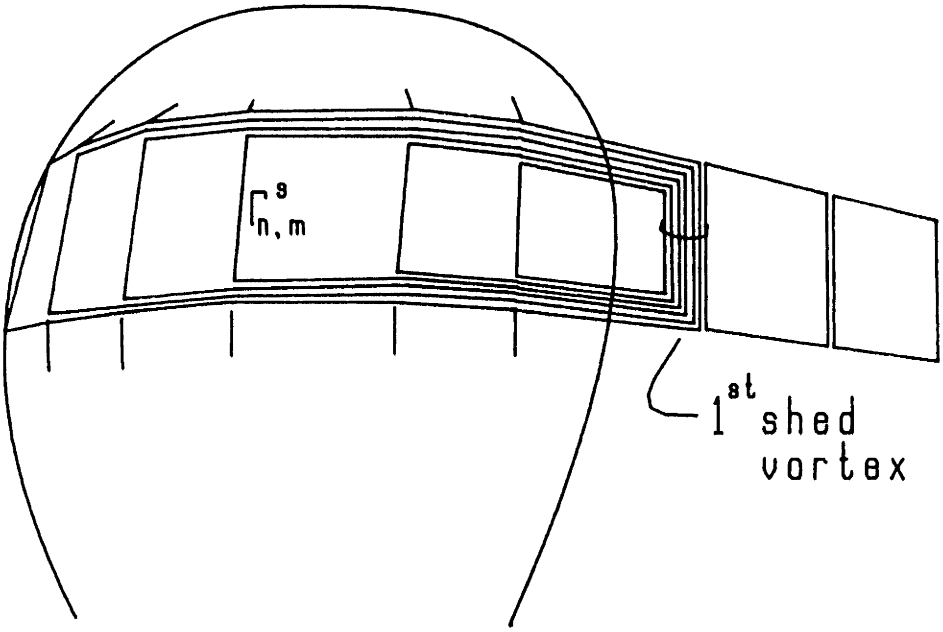

Figure 3.11: Vortex segments organized into closed vortex loops.

where the superscripts on v and Γ refer to the following orientations:

S = spanwise on blade,
C = chordwise on blade,
t = streamwise in wake,
w = spanwise in wake.

By invoking Kelvin's theorem at each grid point one can write (3.30) as

$$\begin{aligned} \mathbf{n}_i \cdot \mathbf{v}_1(\mathbf{x}_i) &= \sum_{k=1}^{K} \left\{ \sum_{m=1}^{M} \left\{ \sum_{n=1}^{N} [v^S_{i,n,m,k} + \sum_{l=n}^{N} (v^C_{i,l,m+1,k} - v^C_{i,l,m,k}) - v^w_{i,1,m,k}] \Gamma^S_{n,m,k} \right.\right. \\ &\left.\left. + \sum_{n=2}^{N_w} [v^w_{i,n-1,m,k} - v^w_{i,n,m,k} + v^t_{i,n-1,m+1,k} - v^t_{i,n-1,m,k}] \mu^w_{n,m,k} \right\} \right\}. \quad (3.31) \end{aligned}$$

The bracketted quantities represent vortex elements organized into closed vortex loops as indicated in Figure (3.11). Defining the loop influence coefficients

$$\square_{inmk} = v^S_{i,n,m,k} + \sum_{l=n}^{N} (v^C_{i,l,m+1,k} - v^C_{i,l,m,k}) - v^w_{i,1,m,k} \quad (3.32)$$

$$\Box^{w}_{inmk} = v^{w}_{i,n-1,m,k} - v^{w}_{i,n,m,k} + v^{t}_{i,n-1,m+1,k} - v^{t}_{i,n-1,m,k} \tag{3.33}$$

permits writing

$$\sum_{k=1}^{K}\sum_{m=1}^{M}\sum_{n=1}^{N} \Box_{i,n,m,k}\Gamma^{S}_{n,m,k} = -\sum_{k=1}^{K}\sum_{m=1}^{M}\sum_{n=2}^{N_w} \Box^{w}_{i,n,m,k}\mu w_{n,m,k} - \mathbf{n}_i \cdot \mathbf{v}_1(\mathbf{x}_i). \tag{3.34}$$

Thus the boundary value problem of equation (2.13) is reduced to solving a set of $K \times M \times N$ simultaneous equations for the unknown Γ^{S}'s.

By writing equation (3.32) in the form shown above one feature becomes evident. The matrix to be inverted includes the influence of the first shed vortex in the wake. Each $\Box_{i,n,m,k}$ (read "loop") on the blade includes the quantity $v^{w}_{i,1,m,k}$. It has already been shown that the vorticity in the wake is convected with the local velocity. Therefore the position of the first shed vortex depends on the induced velocities near the trailing edge which in turn depend on the position of the first shed vortex.

The computational implications of the wake's involvement in the self influence matrix are great. If the vortex' position is allowed to vary with time then the $\Box_{i,n,m,k}$ must be obtained iteratively, requiring many matrix inversions — at least one per time step. This cost combined with that of calculating the downstream wake position would make the model prohibitively expensive. If the position of the first shed vortex was constant, then an LU decomposition of the matrix could be done once with only back-substitution required at each time step. To gain this computational advantage the vortex' position is fixed on an extension of the blade's camber surface. Its position relative to the trailing edge is given by

$$\mathbf{xw}_{1,m} = \mathbf{x}_{te_m} + \frac{1}{4}\, V_c\, \delta t\, \mathbf{e}. \tag{3.35}$$

The unit vector $\mathbf{e}$ is tangent to the blade surface at the trailing edge and V_c is the "convection" velocity given by

$$V_c = (\overline{\mathbf{v}}_2 + \mathbf{x}_{te_m} \times \boldsymbol{\Omega}) \cdot \mathbf{e} \tag{3.36}$$

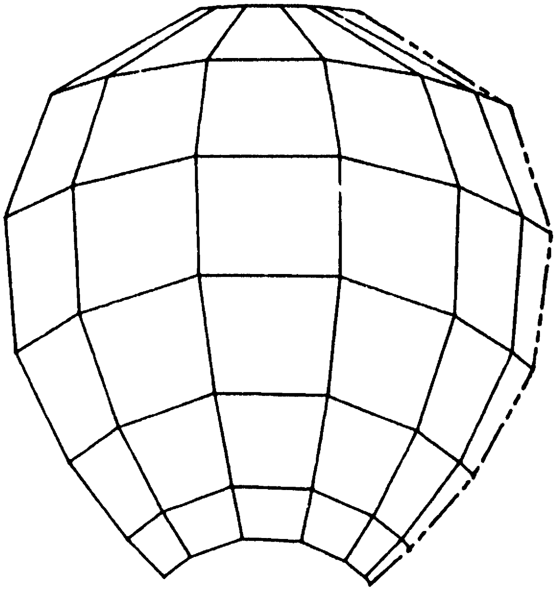

Figure 3.12: Blade grid including the first shed vortex in the wake.

where $\overline{V}_2$ is the circumferential mean background velocity and Ω is the angular velocity of the propeller. The factor of 1/4 was motivated by 2D studies done by Frydenlund and Kerwin [17] which found this to give good agreement with analytical results for unsteady motion. One can see in Figure 3.12 the grid formed by this method. One feature immediately noticeable is the growing size of the trailing edge panel with increasing radial position. Hoshino [29] sought to avoid the resulting extreme jump in panel size by placing the first shed vortex on the camber surface extension, at a fixed fraction of chord length

$$s_w = s_{te} + \frac{1}{4}\frac{c(r)}{N}.$$

While this gives more attractive panel size adjacent to the trailing edge it has the effect of varying the time reference radially. That is, the outer radii feel variations in the inflow earlier than do inboard sections. Chapter 5 discusses this further.

After the first wake grid points are set as described above, the remainder of the wake is prescribed. This prescribed wake geometry is an adaptation of the so-called transition

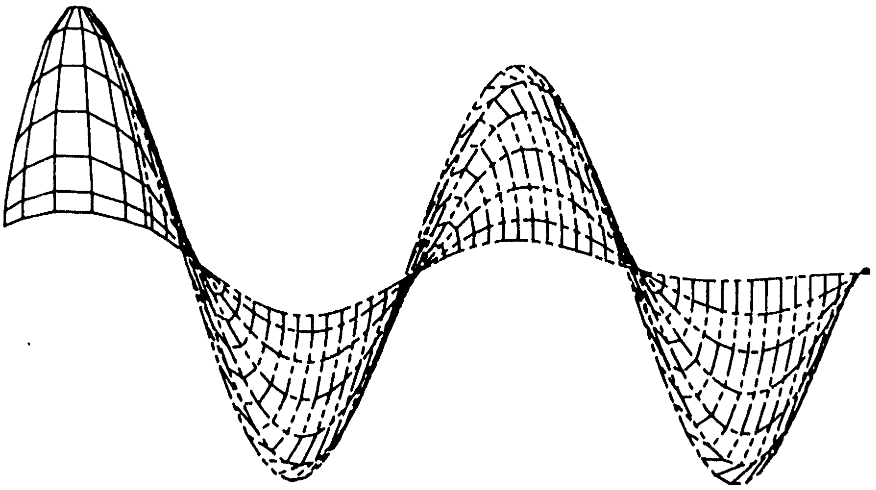

Figure 3.13: Panelling for blade and initial prescribed wake.

wake model described in [22]. It is used only to provide an initial approximate steady solution from which the unsteady free wake calculation is developed. Figure 3.13 shows this panelling.

3.4 Matrix Solution

With the wake positioned, the right hand side vector $\mathbf{b}$ may be computed. Recall from equation (3.34) that

$$b_i = -\sum_{k=1}^{K}\sum_{m=1}^{M}\sum_{n=2}^{N_w} \Box^{w}_{i,n,m,k}\, \mu W_{n,m,k} - \mathbf{n}_i \cdot \mathbf{v}_1(\mathbf{x}_i). \tag{3.37}$$

Since $\mathbf{V} = \mathbf{v}_1 + \mathbf{v}_2$ and $\mathbf{V}\cdot\mathbf{n} = \mathbf{U}\cdot\mathbf{n}$, (3.37) is

$$b_i = -\sum_{k=1}^{K}\sum_{m=1}^{M}\sum_{n=2}^{N_w} \Box^{w}_{i,n,m,k}\, \mu W_{n,m,k} - \mathbf{n}_i \cdot \left[\boldsymbol{\Omega} \times \mathbf{x}_i - \mathbf{v}_2(\mathbf{x}_i)\right]. \tag{3.38}$$

By suitably arranging the indices n, m, k, the matrix equation may be placed into the form

$$\begin{pmatrix} (\mathbf{A}_{11}) & \dots & (\mathbf{A}_{1K}) \\ \vdots & \ddots & \vdots \\ (\mathbf{A}_{K1}) & \dots & (\mathbf{A}_{KK}) \end{pmatrix} \begin{pmatrix} (\boldsymbol{\Gamma}_1^S) \\ \vdots \\ (\boldsymbol{\Gamma}_K^S) \end{pmatrix} = \begin{pmatrix} (\mathbf{b}_1) \\ \vdots \\ (\mathbf{b}_K) \end{pmatrix}. \tag{3.39}$$

Each block in the matrix corresponds to the influence of one blade on another. Suppose that the diagonal blocks of the matrix are separated so that

$$\begin{pmatrix} (\mathbf{A}_{11}) & & 0 \\ & \ddots & \\ 0 & & (\mathbf{A}_{KK}) \end{pmatrix} \begin{pmatrix} (\boldsymbol{\Gamma}_1^S) \\ \vdots \\ (\boldsymbol{\Gamma}_K^S) \end{pmatrix} =$$

$$\begin{pmatrix} (\mathbf{b}_1) \\ \vdots \\ (\mathbf{b}_K) \end{pmatrix} - \begin{pmatrix} 0 & \dots & (\mathbf{A}_{1K}) \\ \vdots & \ddots & \vdots \\ (\mathbf{A}_{K1}) & \dots & 0 \end{pmatrix} \begin{pmatrix} (\boldsymbol{\Gamma}_1^S) \\ \vdots \\ (\boldsymbol{\Gamma}_K^S) \end{pmatrix} \tag{3.40}$$

then equation (3.39) breaks down into the following series of K sub-equations:

$$(\mathbf{A}_{kk})(\boldsymbol{\Gamma}_k^S) = (\mathbf{b}_k) - \sum_{i=1}^{K} (\mathbf{A}_{ki})(\boldsymbol{\Gamma}_i^S), \qquad k = 1, 2, \dots, K. \tag{3.41}$$

The form of equation (3.41) hints at a substantial computational savings. If the $\boldsymbol{\Gamma}^S$'s appearing on the right side were known the matrix solution could be reduced from an $(N \times M \times K)^2$ effort to $K \times (N \times M)^2$. Fortunately, for a normal propeller, the blade-to-blade influence represented by the summation on the right is small. This circumstance permits use of a block Gauss-Seidel iterative solution which works as follows. At a given time step, the vortex strengths on the right-hand side are approximated as those prevailing at the previous time step. Equation (3.41) is solved for each blade in turn. As soon as a new solution for any blade is known it is used to update the estimated solution on the right. The process is then repeated until the desired tolerance for $\boldsymbol{\Gamma}^S$ is achieved.

The speed-up over direct solution of the full matrix equation is, in fact, even greater than suggested above. Each $(\mathbf{A}_{ij})$ is constant in time by virtue of the placement of the

1^{st} shed vortex so an *LU* decomposition may be performed once at the beginning of the calculation. Only back-substitution is required at each time step thereafter. For normal propellers, a further advantage accrues from the fact that each blade is the same shape. That means that each ($\mathbf{A}_{kk}$) is the same — only one block needs to be decomposed. The resulting scheme is very fast. Computation of the vector **b** takes far longer than does extracting $\boldsymbol{\Gamma}^S$ once **b** is known.

3.5 Blade Loading

Once the discrete vortex strengths are known, the blade forces may be calculated. Previous implementations of vortex lattice lifting surface models have obtained blade forces from the "rotating bedspring" analogy (a term coined by J. E. Kerwin) [22,29,36]. In that approach, one imagines the lifting surface to be *replaced* by the array of singularities. The forces computed are those arising from the application of Joukowski's rule to each vortex segment using velocities evaluated at the vortex segment (usually on its midpoint). Guermond has correctly criticized this approach. Its fault lies in the fact that velocities calculated on the body anywhere away from the control points do not satisfy the kinematic boundary condition (2.28). Kerwin has observed that the effect is to distribute the leading edge suction to each vortex position over the chord in proportion to the vortex' contribution to total section circulation [32]. Thus, moments will be incorrect even if total forces are accurate.

Two alternative methods of calculating force distributions may be suggested as being correct. One may interpolate the velocities correctly computed at the control points to the vortex elements or one may evaluate vorticity at the control points. The latter approach is taken here. Also, rather than apply the Joukowski rule, local pressures will be evaluated. This is seen as a convenience since one often requires surface pressures anyway for additional studies. The remainder of this section will develop the required expression for the surface pressures. The following section will examine the leading edge suction.

Having solved equation (3.39), the velocities at the control points on the blade are immediately available as

$$\mathbf{V}^M(\mathbf{x}_i) = \mathbf{v}_2 - \frac{1}{2\pi}\sum_{k=1}^{K}\sum_{m=1}^{M}\left[\sum_{n=1}^{N}\mathbf{v}^{\square}_{i,n,m,k}\Gamma^S_{n,m,k} + \sum_{n=1}^{N_w}\mathbf{v}^{\square_w}_{i,n,m,k}\mu_{W\,n,m,k}\right] \tag{3.42}$$

where $\mathbf{v}^{\square}_{i,n,m,k}$, $\mathbf{v}^{\square_w}_{i,n,m,k}$ are the vector influences at $\mathbf{x}_i$ of the unit strength vortex loops defined in Figure 3.11. The velocity is written as $\mathbf{V}^M$ to emphasize that it is the mean velocity at the control point. There is also a local jump in velocity caused by the local vortex density $\gamma_{n,m,k}$ which is

$$2\Delta\mathbf{v}_{n,m,k} = \boldsymbol{\gamma}_{n,m,k} \times \mathbf{n}_{n,m,k}. \tag{3.43}$$

Leaving the discrete problem momentarily, note that the velocity on the blade surfaces is

$$\begin{aligned}\mathbf{V}^{\pm} &= \mathbf{v}_2 + \mathbf{v}_1^{\pm} \\ &= \mathbf{v}_2 + \nabla_{S_B}\varphi^{\pm}.\end{aligned} \tag{3.44}$$

The ± signs refer to the back and face of the blades and ∇_{S_B} is the gradient on S_B. Thus, the velocity jump across S_B is also given by

$$\begin{aligned}2\Delta\mathbf{v} &= \nabla_{S_B}(\varphi^+ - \varphi^-) \\ &= \nabla_{S_B}\mu.\end{aligned} \tag{3.45}$$

Now consider the curvilinear coordinate system on S_B formed by taking the tangents to lines of constant radius and chord as the basis vectors. Derivatives of μ along these lines are related to $\Delta\mathbf{v}$ by

$$\frac{\partial\mu}{\partial\xi} = 2\Delta\mathbf{v}\cdot\boldsymbol{\xi} \tag{3.46}$$

$$\frac{\partial\mu}{\partial\eta} = 2\Delta\mathbf{v}\cdot\boldsymbol{\eta}. \tag{3.47}$$

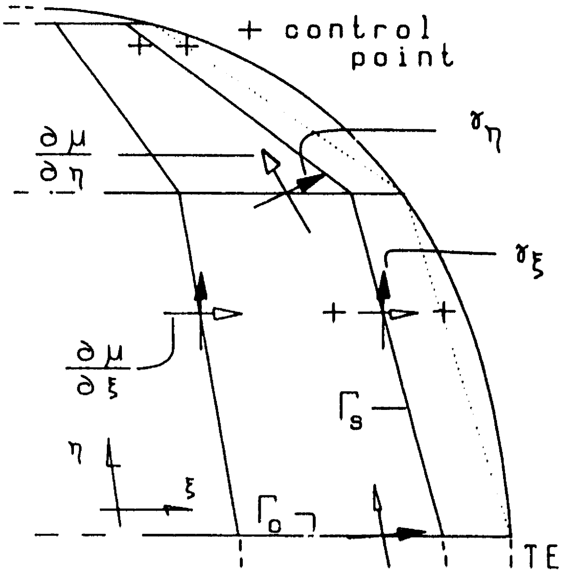

Figure 3.14: Jump velocities from consideration of the potential gradient.

Figure 3.14 shows a detail of the grid. Panel boundaries are indicated along with level curves of ξ and η. The quantities $\xi\partial\mu/\partial\xi$ and $\eta\partial\mu/\partial\eta$ may be approximated as:

$$\left.\frac{\partial\mu}{\partial\xi}\right|_{n+1} \approx \frac{\mu_{n+1,m}-\mu_{n,m}}{\xi_{n+1,m}-\xi_{n,m}}, \tag{3.48}$$

$$\left.\frac{\partial\mu}{\partial\xi}\right|_{n} \approx \frac{\mu_{n,m}-\mu_{n-1,m}}{\xi_{n,m}-\xi_{n-1,m}}, \tag{3.49}$$

$$\left.\frac{\partial\mu}{\partial\eta}\right|_{m+1} \approx \frac{\mu_{n,m+1}-\mu_{n,m}}{\xi_{n,m+1}-\xi_{n,m}}, \tag{3.50}$$

$$\left.\frac{\partial\mu}{\partial\xi}\right|_{m} \approx \frac{\mu_{n,m}-\mu_{n,m-1}}{\xi_{n,m}-\xi_{n,m-1}}. \tag{3.51}$$

The relation between μ and Γ^S can be used to write

$$\left.\frac{\partial\mu}{\partial\xi}\right|_{n+1} \approx \frac{\Gamma^S_{n+1,m}}{|\mathbf{xp}_{n+1,m}-\mathbf{xp}_{n,m}|}. \tag{3.52}$$

Writing the denominator in terms of the Cartesian coordinates of the control points simplifies the implementation. The order of the approximation is preserved. Similar expressions hold for the remaining gradients of μ.

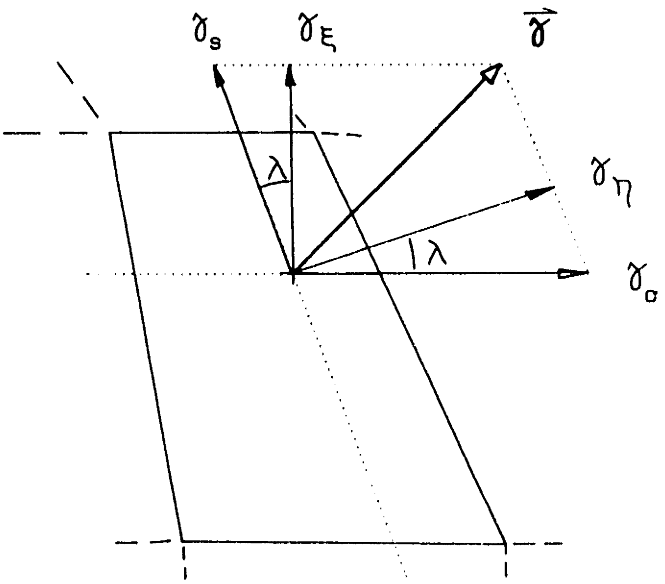

Figure 3.15: Relation of interpolated vortex density components to total vortex density.

These jump velocities correspond to the component vortex densities γ_η and γ_ξ also shown in Figure 3.14. Finally, the desired vortex density is found by interpolating γ_η and γ_ξ to the the control point where the local grid angle λ allows $\gamma_{n,m}$ to be deduced as shown in Figure 3.15.

Bernoulli's equation (2.37) also includes a term $\partial\varphi/\partial t$ which must be evaluated for unsteady flows. Unsteady in this sense refers to the ship-fixed, inertial coordinates so, in this model, propellers operating in axisymmetric inflows are unsteady (although we speak of such cases as steady flows, having in mind the blade loading as a function of time).

To compute $\partial\varphi/\partial t$, suppose that at time t_0 the control point at which pressure is to be computed is at (x, r, Θ_0). If the propeller loading is constant in time and its rotation speed is Ω that potential will prevail at a later time t at the location $(x, r, \Theta_0 + \Omega t, t_0)$. That is,

$$\varphi(x, r, \Theta, t) = \varphi(x, r, \Theta_0 + \Omega t, t_0). \tag{3.53}$$

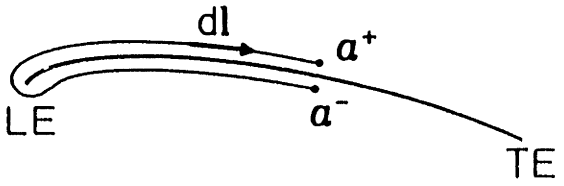

Figure 3.16: A section through the blade showing the contour for calculating potential jump at a.

If, however, the loading is unsteady then

$$\varphi(x,r,\Theta,t)=\varphi(x,r,\Theta_0+\Omega t,t_0)+\int_{t_0}^{t}\frac{\partial\varphi}{\partial\tau}d\tau. \tag{3.54}$$

The new term on the right represents the accumulated change of potential at the blade-fixed point of interest. It follows that

$$\frac{\partial}{\partial t}\varphi(x,r,\Theta,t)=\frac{\partial\varphi}{\partial\Theta}\frac{\partial\Theta}{\partial t}+\left.\frac{\partial\varphi}{\partial\tau}\right|_t \tag{3.55}$$

which can be rewritten as

$$\frac{\partial\varphi}{\partial t}=r\Omega u_t+\left.\frac{\partial\varphi}{\partial\tau}\right|_t . \tag{3.56}$$

The quantity u_t is the tangential velocity induced by the singularities on the propeller.

Now consider a section through the blade at constant radius. The velocity at a point a, say, is given by

$$\mathbf{V}=\mathbf{v}_2+\nabla\varphi .$$

With reference to the contour shown in Figure 3.16, one may write

$$\begin{aligned}\int_{a^-}^{a^+}\nabla\varphi\cdot d\mathbf{l} &= \varphi^+-\varphi^- \\ &= \int_{LE}^{a}\left(\mathbf{V}^+-\mathbf{V}^-\right)\cdot d\mathbf{c}.\end{aligned} \tag{3.57}$$

The integral on the left is over one side, from the leading edge to a. Substituting for the velocity jump from equation (3.43) gives

$$\varphi^+ - \varphi^- = \int_{LE}^{a} (\gamma \times \mathbf{n}) \cdot d\mathbf{c}. \tag{3.58}$$

The vortex density can be written as

$$\gamma = \gamma_s \mathbf{e}_2 + \gamma_c \mathbf{e}_1 \tag{3.59}$$

where the unit vectors $\mathbf{e}_1$ and $\mathbf{e}_2$ are tangents to the constant radius and constant chord curves, respectively. The components of vortex density used here are related to γ_ξ and γ_η defined previously by the relations

$$\gamma_s = \gamma_\xi \sec\lambda \tag{3.60}$$

$$\gamma_c = \gamma_\eta \sec\lambda \,. \tag{3.61}$$

By construction, $d\mathbf{c} = \mathbf{e}_1 dc$ from which it follows that

$$\gamma \cdot (\mathbf{n} \times d\mathbf{c}) = -\gamma_s \cos\lambda \, dc \,. \tag{3.62}$$

Thus, at the n^{th} control point

$$\varphi_n^+ - \varphi_n^- \approx \sum_{j=1}^{n} \gamma_{s_j} \Delta c_j \cos\lambda \,. \tag{3.63}$$

But

$$\Gamma_j^S = \gamma_{s_j} \Delta c_j \cos\lambda$$

so that

$$\varphi_n^+ - \varphi_n^- \approx \sum_{j=1}^{n} \Gamma_j^S \,. \tag{3.64}$$

Finally,

$$\frac{\partial \varphi^\pm}{\partial t} = r\Omega u_t \pm \frac{1}{2} \sum_{j=1}^{n} \frac{\partial \Gamma_j^S}{\partial t} \,. \tag{3.65}$$

Return once again to equation (2.37). The pressure at points on the propeller is related to that far upstream by

$$\frac{1}{2}\rho V^{\pm 2} + \rho\frac{\partial \varphi^{\pm}}{\partial t} + p^{\pm} = \frac{1}{2}\rho V_{\infty}^{\pm 2} + p^{\pm}\,. \tag{3.66}$$

The pressure jump across S_B is then

$$p^{+} - p^{-} = \frac{1}{2}\rho\left(V_{\infty}^{-2} + V_{\infty}^{+2}\right) + \frac{1}{2}\rho\left(V^{+2} + V^{-2}\right) + \rho\frac{\partial}{\partial t}\left(\varphi^{+} - \varphi^{-}\right) \tag{3.67}$$

assuming $p_{\infty}^{+} = p_{\infty}^{-}$. The rotationality of the background flow requires that $V_{\infty}^{\pm}$ be distinguished from each other but if, as has been assumed, the vorticity in the background is weak then the difference $V_{\infty}^{+2} - V_{\infty}^{+2}$ is small, giving

$$p^{+} - p^{-} \approx \frac{1}{2}\rho[\left(\mathbf{V}^{M} + \Delta\mathbf{v}\right)^{2} - \left(\mathbf{V}^{M} - \Delta\mathbf{v}\right)^{2}] + \rho\,\frac{\partial}{\partial t}\left(\varphi^{+} - \varphi^{-}\right)\,. \tag{3.68}$$

The pressure jumps are combined with the corresponding panel area and unit normal to obtain an incremental force $\Delta\mathbf{F}$ which acts at the control point.

Kim and Kobayashi [37] report a similar method for computing pressures based on the steady lifting surface code PSF2 [22]. Their method appears to be in error in two respects: first, spanwise gradients corresponding to equations (3.50) and (3.51) are approximated by taking δr as the denominator rather than the actual curvilinear distance and, second, the mean velocity is computed on the vortex segment, a location where flow tangency does not obtain. Direct comparison between their results and this work are unavailable since they included thickness effects which are not considered here. It is clear, though, that when the propeller is raked δr will differ from $\delta\eta$ thus causing the chordwise vorticity component to be overestimated.

3.6 Leading Edge Suction

Recall from Chapter 2 that the leading edge suction force is given by

$$\mathbf{F}_S = -\frac{1}{4}\pi\rho C_S^2\,\mathbf{i}$$

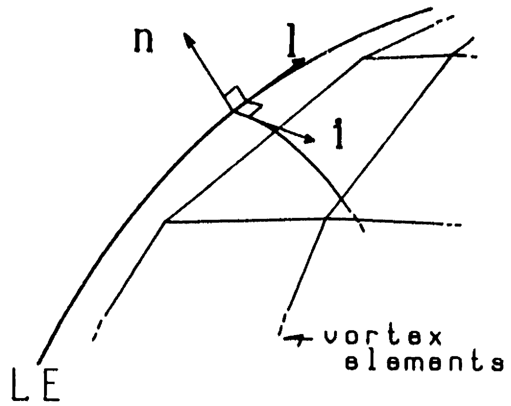

Figure 3.17: Coordinate system and blade grid for leading edge suction.

where

$$C_S = \lim_{s\to 0} \sqrt{s}\,\gamma(s)\cdot \mathbf{l}.$$

Lan showed in his analysis of the QUM that the value of C_S could be obtained directly by computing the downwash at the leading edge. Guermond has noted in [24] that this method cannot be applied to quadrilateral panels. Because of the mislocation of the straight edges of the panels a logarithmic error is produced in the calculation of nearfield velocities. At the leading edge, in particular, the vortex strengths are large and the required downwash point very close by. Thus, leading edge suctions calculated in this way are likely to produce large errors, particularly where the leading edge has large curvature. Additionally, it requires computing an extra set of influence coefficients.

In this work, a direct application of the limit process expressed in equation (2.39) is employed. Figure 3.17 shows a detail of the leading edge. To evaluate the limit, the vorticity γ is calculated at the control points along a streamwise strip. Near the leading edge, the distances from the leading edge to the n^{th} control point measured along a grid curve, s_n, and in the **i** direction, c_n, are related according to $c_n = s_n \cos \lambda$ where λ is the angle that the constant radius grid line makes with the unit vector **i**.

The vortex strength at the leading edge is estimated by $\gamma_n = \boldsymbol{\gamma}_n \cdot \mathbf{l}$. Now

$$C_S = \sqrt{c_n}\gamma_n \tag{3.69}$$

must be evaluated for $n \to 0$. This requires extrapolation since the quantities called for are only known inboard of the leading edge. The extrapolation can be made reliable if it is assumed that γ may be expressed as

$$\gamma(c) = \frac{1}{\sqrt{c}}P(c) \tag{3.70}$$

where $P(c)$ is a polynomial to any degree in c. If this is the case, the slope of the curve $\sqrt{c}\gamma$ vanishes at the leading edge. The assumption is not very restrictive. It is true for a flat plate and for parabolic camber. It strictly fails for NACA a-series loadings but these are mathematical idealizations, requiring a logarithmic singularity in camber at the leading edge. The loading actually achieved is probably closer to something expressible by (3.70). The force finally calculated is then scaled by the length of the leading edge vortex segment and applied at a point which lies on the leading edge of the "equivalent propeller", that is, at a point obtained by interpolating from the leading edge positions at the adjacent grid point radii as shown in Figure 3.18.

This approach is computationally effective in that it obtains C_S directly from already known quantities: no additional influence coefficients need be calculated. It, of course, does nothing to capture the contribution to $\mathbf{F}_S$ due to the curvature of the leading edge. This is left as future work.

3.7 The wake

The wake sheet evolves from its initial prescribed geometry according to

$$\frac{\partial \mathbf{xw}_{nmk}}{\partial t} = \mathbf{V}_{n,m,k} \tag{3.71}$$

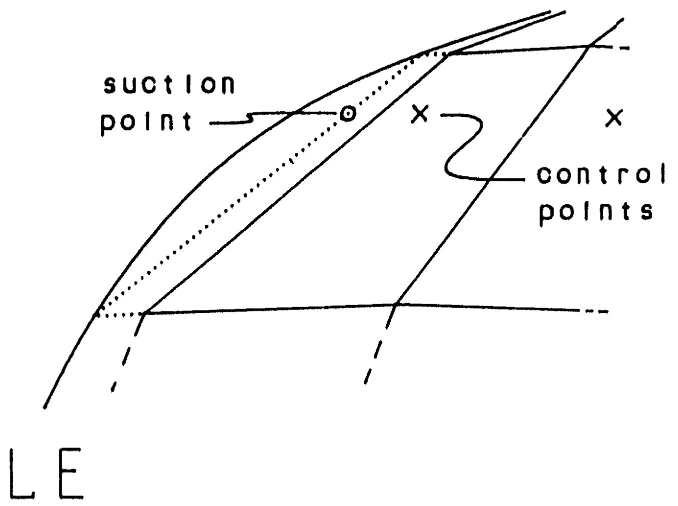

Figure 3.18: Interpolation to locate the point of action for the leading edge suction.

where **xw** is the position of a grid point on the wake sheet and **V** is the total velocity at that point. This simple equation contains a Pandora's box of trouble.

A typical grid point is at the junction of four vortex segments. Strictly, the induced velocity is undefined here. To avoid this difficulty, the contributions from the attached vortex segments are often simply ignored [11,22,56]. The only real attraction of this approach is that it gives induced velocity at the grid points directly. It cannot be justified as a correct quadrature for the wake integral

$$\mathbf{v}_{n,m,k} = \int_{S_W} \mu_W \nabla(\mathbf{n} \cdot \nabla_\xi \frac{1}{|\mathbf{x}_{n,m,k} - \boldsymbol{\xi}|}) d\sigma$$

It also has the drawback of effectively doubling the panel size.

The Cauchy singularity can be handled without wasting panels by simply computing wake induced velocities at the panel centroids. The required grid point velocities are then obtained by interpolation. Recalling that the first shed vortex in the wake was placed at the 1/4-chord of the panel swept out by the trailing edge in one time step, this simple mid-point rule places wake control points at the 3/4-chord location.

As discussed in Chapter 2, the self-induction associated with the curvature of the tip vortex, at least, must be accounted for. The induced velocity at grid points along the tip vortices are obtained by interpolation from values calculated directly at the midpoints of the tip vortex segments. To these values are added the LIA contribution, $\mathbf{u}_l$. Recall from equation (2.27) that this is given by

$$\mathbf{u}_l = \frac{\kappa\Gamma}{4\pi}\ln\left(\frac{L}{\varepsilon}\right)\mathbf{b}. \tag{3.72}$$

This contribution is estimated by fitting to the tip vortex a circular arc which passes through the desired grid point and its immediate upstream and downstream neighbor. The values of the curvature κ, the arc length L, and the direction of the binormal $\mathbf{b}$ are then immediately available. The core size ε is assigned as discussed in Chapter 5.

Besides the local effects of the sheet on itself dealt with above, a free-wake model must anticipate a more pernicious problem — the close approach of one part of the sheet to another. Close approach is normally seen in the rolling-up part of the sheet where discrete vortices in one turn of the rollup spiral are brought into close proximity with vortices in an adjacent turn. As important length scales become comparable to panel dimensions the quality of the near field representation deteriorates, spurious velocities result, and the integrity of the sheet's structure is destroyed.

Various techniques have been proposed to deal with near-field modelling. Chorin and Benard [9] introduce a finite core to the vortices. Krasny [39] takes a similar approach to desingularizing the Cauchy integral. Combining vortices that approach each other too closely into a single "equivalent" vortex has been used by Smith [71] and Moore [54]. This method has been applied to adjacent vortices on the same sheet but not, to the author's knowledge, when the nearby vortices are on different sheets. Maskew [49] introduced the so-called sub-vortex technique. In his method, when a field point at which velocity is to be calculated is too close to the vortex sheet, the sheet is subdivided into smaller panels until the field point distance is sufficiently large compared to the local subpanel size. Fink and Soh [15] periodically regrid the vortex sheet to preserve the order of the geometric aproximation. Hoeijmakers and Vaatstra [28] use a higher-order representation of the vortex distribution in combination with adaptive panelling and amalgamation.

These approaches have been motivated by the need to capture in some detail the structure of the rollup spiral. It is fortunate that this work does not require that information. Leading edge vortex sheet separation, while important to propeller performance, is not contained in this model. Therefore, detailed resolution of the leading edge vortex is not required. Even when the propeller is operating at a low advance coefficient so that tip vortices might be expected to pass close aboard the following blades, the distances are great enough so that a far-field approximation of the tip structure is all that is needed.

In this work, the simplest model possible has been chosen. A cutoff radius is prescribed for application of the Biot-Savart integration. If a point is within this radius of a vortex segment, the induced velocity contribution is set to zero. The value of the cutoff radius is taken to be quite small compared to typical panel dimensions.

After all induced velocities have been calculated at the wake grid points there will be found some less extreme but still unacceptable induced velocities. To deal with these, an *ad hoc* damping function is applied to the induced velocities before they are combined with the background to form the convection velocities. With this damping the "corrected" induced velocities $\mathbf{v}_c$, are obtained from the directly calculated $\mathbf{v}_d$'s according to

$$\mathbf{v}_c = \mathbf{v}_d\left[1 - \exp\left(\frac{-{U_R}^2}{\alpha_d\, v_d^2}\right)\right] \tag{3.73}$$

where α_d is a damping parameter which controls the range of induced velocities affected and U_R is a reference velocity given by

$$U_R = \sqrt{V_S^2 + (0.7R\,\Omega)^2}. \tag{3.74}$$

V_S is the speed of advance of the propeller (ship speed), R is the tip radius of the

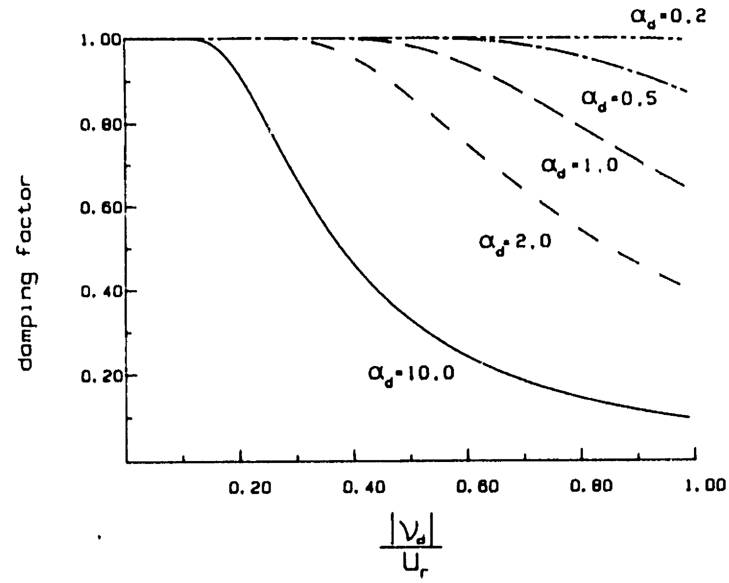

Figure 3.19: Reduction in magnitude of induced velocities for various values of α_d.

propeller, and Ω is its angular speed. Figure 3.19 shows the effect of various values of α_d. Figure 3.20 shows the distribution of induced velocities in the wake of a propeller blade with greater than design loading. The wake comprised 180 grid points of which 176 have induced velocities less than U_R, most are less than $0.2U_R$. Comparing this figure with Figure 3.19 shows that $\alpha_d = 1.0$ damps only the most extreme values by any significant amount.

The treatment of the induced velocities in the wake described above is intended to supress spurious extreme velocities. It alone is not sufficient to ensure orderly evolution of the wake sheet. The discrete vortices in the rollup region have a natural tendency to orbit about each other. The period of this orbitting motion, governed by panel size and vortex strengths, forces a local time scale which must be considered when time step size is selected during the integration of equation (3.71). If the time step is large compared to the local time scale, the vortices near the tip deviate from their proper paths and the wake structure is destroyed. If the length of the time step is adjusted to keep it

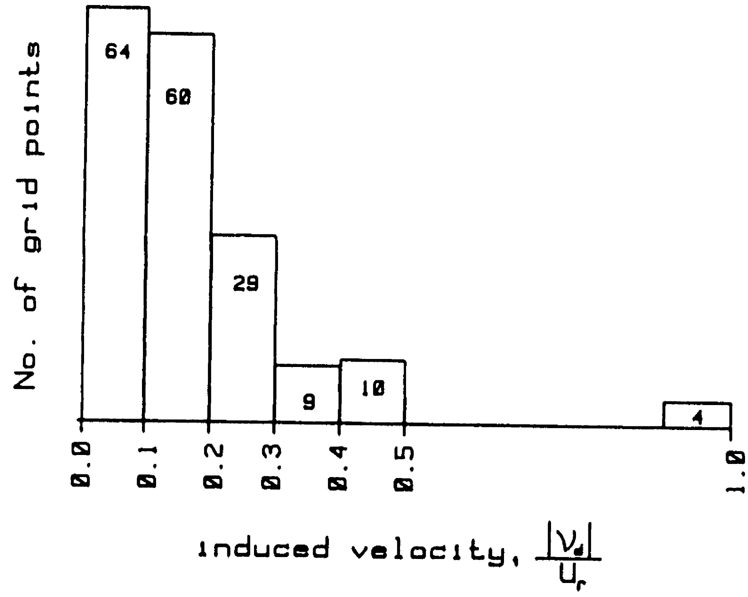

Figure 3.20: The distribution of induced velocities in the wake of a one-bladed NSRDC 4118 propeller at $J = 0.83$.

appropriately small, the integration grinds to a halt as the tip spiral rolls up tighter and the panel size shrinks.

Rather than try to chase the vortex sheet into an infinite spiral it has become almost universal practice since Ham [26] and Smith [71] (at least in 2D) to collect the innermost part of the spiralling sheet into a single vortex. In a simple example, when the amalgamation criterion is triggered, the tip vortex and its nearest neighbor on the sheet are replaced by a single vortex placed at the center of vorticity. The wake sheet is then often repanelled so that the total number of vortices remains constant.

Applying this process in three dimensions has its advantages. The time step can be kept conveniently large and the number of panels (hence the number of influence coefficients to be calculated) is reduced. Since the calculation time goes like N^2 times the number of time steps, reducing N and increasing δt has an irresistable attraction.

The amalgamation process as implemented here proceeds as follows. At each time

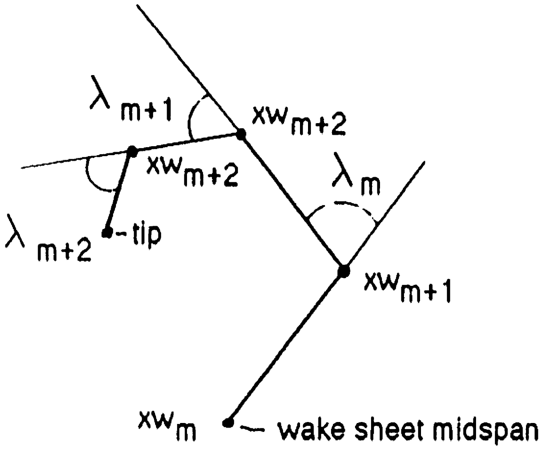

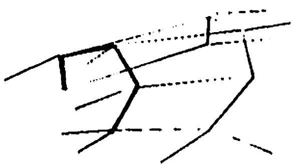

Figure 3.21: Schematic showing how rollup is measured.

step, the extent to which the sheet has rolled up about the tip vortex is examined. This value is expressed as the accumulated spanwise folding referred to a location near the midspan of the sheet. See Figure 3.21. The amalgamation process is triggered if this value exceeds a specified limit. Amalgamation consists of collapsing the two outermost grid points so that

$$\left.\begin{array}{l}\mathbf{xw}_{M+1}(t^+)\\ \mathbf{xw}_M(t^+)\end{array}\right\} = \frac{|\Gamma^t_{M+1}|\,\mathbf{xw}_{M+1}(t) + |\Gamma^t_M|\,\mathbf{xw}_M(t)}{|\Gamma^t_{M+1}| + |\Gamma^t_M|}. \tag{3.75}$$

Chapter 4

Unsteady Wake Geometry Measurements

Experimental data regarding the wake geometry, in particular, the tip vortex geometry, of marine propellers is scarce. Virtually all data refer to steady flow situations. Loukakis [48] made direct observations of the steady geometry of cavitating tip vortices from an NSRDC 4118 propeller at various advance coefficients. Okamura [61] and Shih [70] made measurements using laser doppler velocimetry (LDV) techniques.

Okamura measured the radial position of the tip vortices for a model propeller described as being designed for a 50,000 dwt ship. He also inferred the pitch of the wake sheets from circumferential mean velocities measured in the wake of the propeller. Unfortunately, the particulars of the propeller design given in that paper are incomplete.

Shih made measurements of wake pitch for an NSRDC 4644 propeller under both uniform and steady shear flow conditions. Two techniques were used. The so-called laser beam crossing method he used locates the vortices by dropping the propeller tunnel pressure until the vortex cores cavitate. The LDV sampling volume is then positioned on the vortex and its location obtained from the LDV's positioning apparatus. Corresponding pitch measurements are also reported. These were derived from consideration of the phase relationship of time varying velocities in the vicinity of the tip vortex at various points along the slipstream.

One expects the free wake analysis method described in Chapters 2 and 3 should match steady flow data such as these but it must also be compared to unsteady flow cases. Loukakis, in the work previously cited, observed but did not measure the tip vortex geometry for the NSRDC 4118 propeller operating behind a wake screen which produced a 30% wake defect over one quadrant of the propeller disk. These observations showed the same kind of distortion of the wake geometry by the local wake defect as is produced by a ship's wake.

This well-known propensity of vortex sheets to conform to the local velocities accents the importance of more detailed information on the transient configuration of the wake. Such data are required to validate any unsteady free-wake model. To this end an experiment was performed to quantify the instantaneous tip vortex wake geometry for a representative propeller operating in a nonuniform inflow. To the author's knowledge, no other studies of tip vortex geometry for unsteady flow have been reported until now.

4.1 Apparatus

An NSRDC 4497 propeller as described in Table 4.1 was available and was judged to be representative of the type that the code would be required to analyze. All tests were conducted in the MIT Variable Pressure Water Tunnel. This tunnel has a 20 inch square test section with observation windows that permit approximately 12 inches of vertical and 18 inches of streamwise travel for the LDV sampling volume. Both the tunnel and the LDV apparatus have been described by Kobayashi [38]. A description of the theory behind laser doppler velocimetry (also called laser doppler anemometry) may be found in reference [12].

A smoothly varying wake profile would be desirable as a test case but wake screens don't lend themselves to creating truly smooth wakes. It is even more difficult to "grow" a ship wake by placing a body upstream of the propeller. In the end, the inflow to the

Number of blades: 5
Hub/Diameter ratio: 0.2
Expanded area ratio: 0.725
Section meanline : NACA a=0.8
Section thickness Distribution: NACA 66 (modified)
Design advance coefficient, J_A : 0.889

r/R	P/D	$rake/D$	Θ_s	C/D	f_0/C	t_0/D
0.20	1.455	0.000	0.000	0.174	0.0430	0.0434
0.25	1.444	0.000	2.328	0.202	0.0395	0.0396
0.30	1.433	0.000	4.655	0.229	0.0370	0.0358
0.40	1.412	0.000	9.363	0.275	0.0344	0.0294
0.50	1.361	0.000	13.948	0.312	0.0305	0.0240
0.60	1.285	0.000	18.378	0.337	0.0247	0.0191
0.70	1.200	0.000	22.747	0.347	0.0199	0.0146
0.80	1.112	0.000	27.145	0.334	0.0161	0.0105
0.90	1.027	0.000	31.575	0.280	0.0134	0.0067
0.95	0.985	0.000	33.788	0.210	0.0140	0.0048
1.00	0.942	0.000	36.000	0.0001	0.0001	0.0029

Table 4.1: Particulars of the test propeller.

propeller was configured by a wake screen designed to split the flow into two regions of approximately ±12 per cent of the volumetric mean flow.

The design method for the wake screen is described by McCarthy [50]. By judicious selection of screen material with appropriate combinations of wire diameter and spacing one can control the pressure drop across the screen surface. The pressure drop is virtually independent of Reynolds number in the range of interest for these tests. The screen was mounted upstream by means of a collar attached to the propeller shaft. The perimeter of the screen was supported by a ring held by struts cantilevered from this collar as shown in Figure 4.1. Figure 4.2 shows the results of axial velocity measurements in the propeller plane.

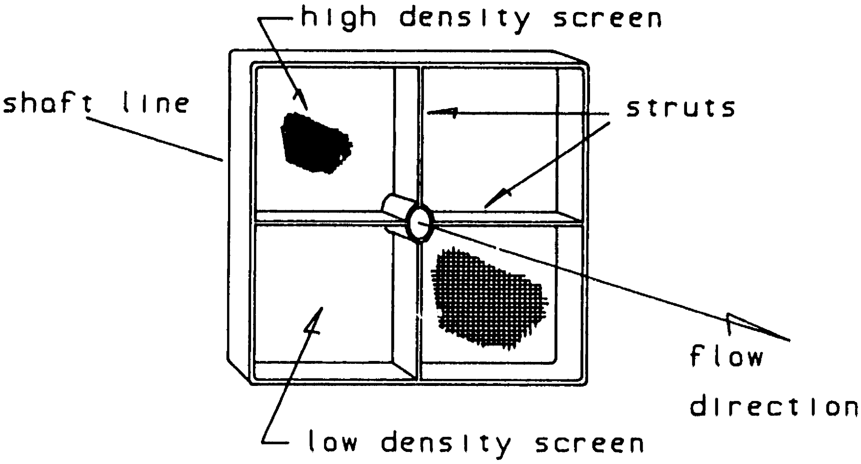

Figure 4.1: Construction of the wake screen and support.

4.2 Inflow Characteristics

The gross characteristics of the velocity field are as designed. There are localized jets downstream of the support struts which were unanticipated. These are the result of the nonlinear interaction of the screen with the stagnation zone at the leading edges of the struts. As noted above, while the pressure drop effected by the screen is linear in approach velocity over a wide range of Reynolds number it tends to decrease with R for smaller R. The stagnation zone near the blunt leading edge of the strut prevented the screen from causing any significant pressure drop. The downstream velocity recovery in the strut's potential flow field transforms this nil pressure drop into a jet. (Anecdotally, it should be pointed out that the detailed shape of the strut leading edge can change this effect radically. These struts had a squared off leading edge. Shih [69], for a similarly constructed screen having struts with rounded leading edges, shows velocity defects behind the struts). These jets were considered unobtrusive enough so that no effort was

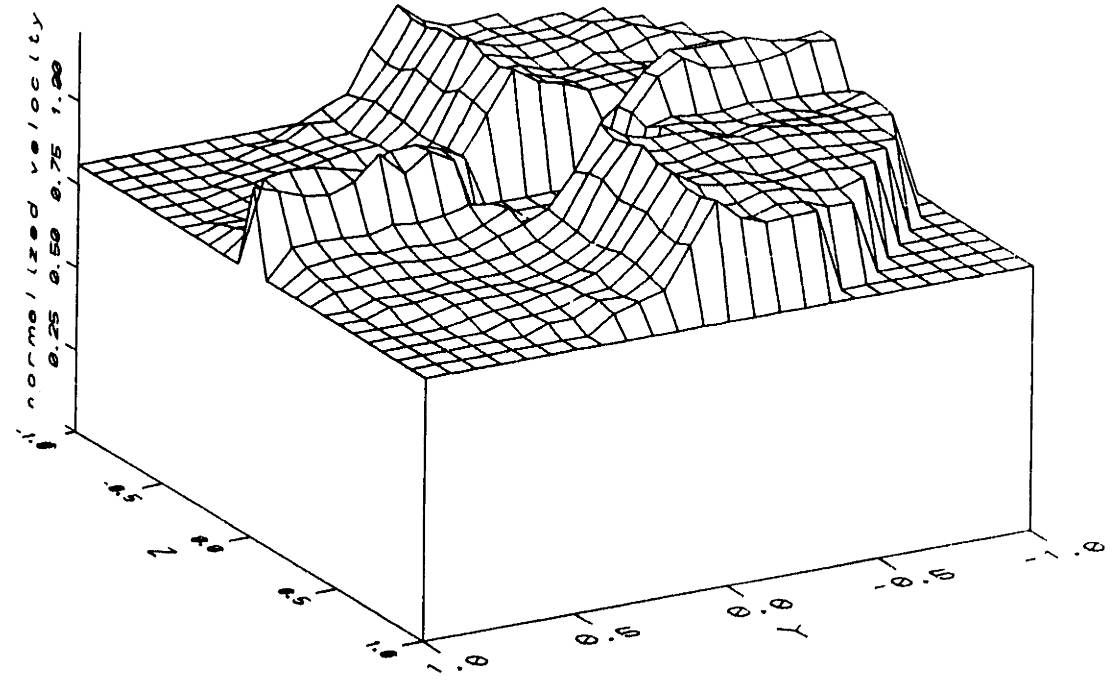

Figure 4.2: Axial velocity in the propeller plane.

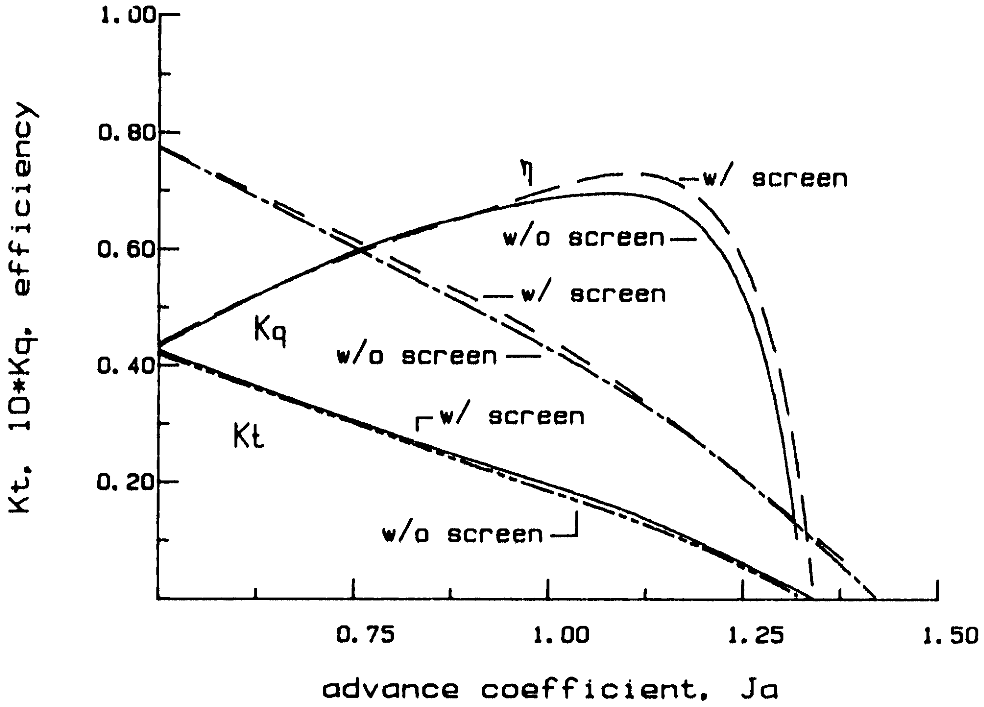

Figure 4.3: Performance of 4497 propeller in open water and behind wake screen.

made to eliminate them.

4.3 Propeller Operating Point

Performance tests for the model propeller were conducted in open water and behind the wake screen. The 4497 is designed for an advance coefficient of $J = 0.889$. At this J, the measured thrust coefficient was $K_t = 0.235$. The advance coefficient in the screen wake, J_s, corresponding to this thrust value was determined to be $J_s = 0.906$. This operating point was used throughout the experiment. Figure 4.3 shows the results of these tests. Propeller tests in the MIT facility are normally run at a minimum of 1000 RPM to avoid Reynolds number scaling problems as much as possible. In this experiment, the rotation speed of the propeller was limited to 900 RPM. This was for two reasons. The wake screen blockage required that the tunnel impeller RPM be doubled (as compared with an open water test) to produce a given mean flow. Also, at this operating point the screen structure was at its strength limits. This gives a Reynolds number of about 10^6

based on the $.7R$ blade section.

4.4 Wake Surveys

Once the operating point for the propeller/wake screen combination was determined, three wake surveys were made in or near the plane of the propeller. First, a nominal wake survey in the plane of the propeller was done. Axial velocity downstream of the wake screen was mapped. Second, an unsteady axial velocity map was obtained at a station 1.5 inches upstream of the nominal propeller plane. These measurements were made with the propeller installed and running at its operating point. The third set of measurements was a steady axial velocity map in the same location as the unsteady.

4.5 Measurement Paradigm

In a variable pressure water tunnnel, it is common practice to locate propeller tip vortices by lowering tunnel pressure until the high velocity vortex cores reach incipient cavitation. Shih used this technique in his steady measurements. This method of visualization can lead to trouble in the presence of a wake screen. It can happen that the cavitation number for the screen wires is reached before that for the vortex cores. This was the case in this experiment. The result of wake screen cavitation was a complete "white-out" of the tunnel test section, obscuring the vortices altogether. A more elaborate indirect measurement technique was developed to circumvent this problem.

In the new technique, it is assumed that the tip vortex structure can be modelled as discrete helices having finite cores of constant vorticity, i.e., as Rankine vortices. This paradigm allows us to understand how velocity measurements may be used to locate the vortices. The essence of the technique is to interpret the characteristics of unsteady axial velocity measurements near the boundary of the slipstream in light of this vortex model. To locate a point on a vortex is then a two step process. The first step is to obtain the

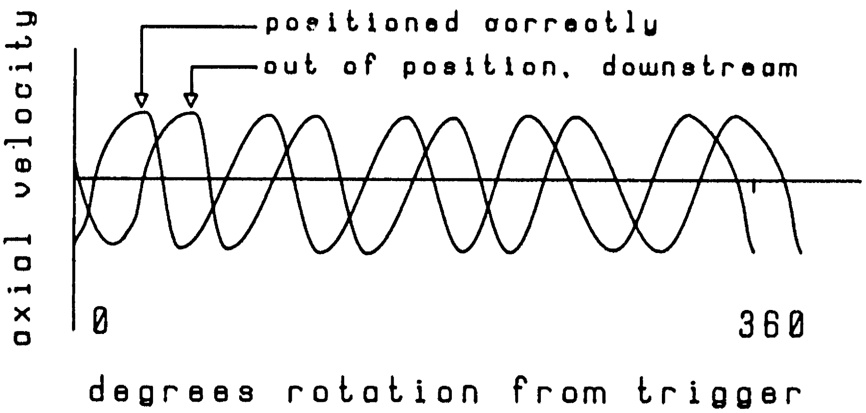

Figure 4.4: Schematic velocity waveforms for positioning LDA in streamwise direction.

correct axial position. Assuming the LDA's sampling volume is located outside but near the race one expects the axial velocity waveform to show a velocity decrement when a tip vortex is close aboard. By observing the phase relationship of this event with respect to the trigger pulse one can "home in" on a particular blade's tip vortex. Figure 4.4 shows schematically how the waveforms are interpreted for axial positioning. This technique works best by starting near a blade tip. This eliminates the possibility of confusing the vortices from different blades.

Having established the axial location of the vortex one then traverses the LDA sampling volume radially to find the remaining two coordinates. This part of the process is an extension of the technique described by Shih [70]. Again, the axial velocity is observed. As the sampling volume passes from outside to inside the tip vortex position, the Rankine vortex model predicts a progression of waveforms such as sketched in Figure 4.5. One first observes a growing amplitude as the outer boundary of the vortex core is approached. Then the amplitude decreases as the vortex core is traversed. After

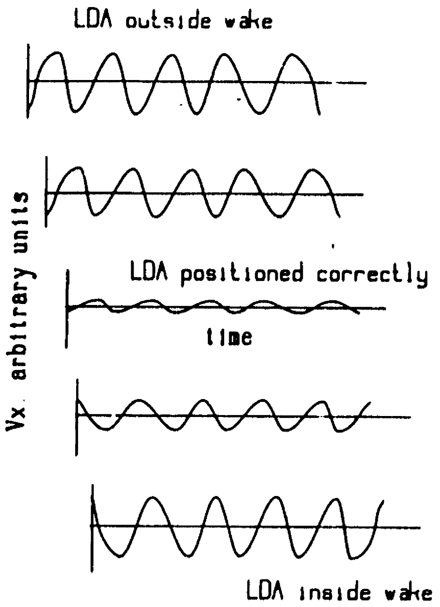

Figure 4.5: Schematic velocity waveforms for positioning LDA radially.

passing through the center of the vortex core the amplitude increases but with opposite sign. The vortex location is defined to be that point at which the amplitude is a minimum.

In practice, the process is not so simple. It is necessary to iterate the axial and radial traverses several times for each data point. A large number of factors conspire to conceal the clean waveforms of Figures 4.4 and 4.5 from the observer. The vortex location is not exactly repeated from one revolution to the next due to general fluctuations in the flow as well as to the natural instability of the vortex line. The detailed structure of the vortex core differs from the Rankine idealization. There is a vortex sheet shed from the inboard portions of the propeller's trailing edge. This sheet is attached to the tip vortex and is being rolled up into it. There is some phase noise in the triggering mechanism. The LDA traverse carraige was somewhat flexible and permitted fairly large oscillations of the sampling volume (especially in the streamwise direction). Figure 4.6 shows some actual velocity waveforms such as were observed during the positioning process.

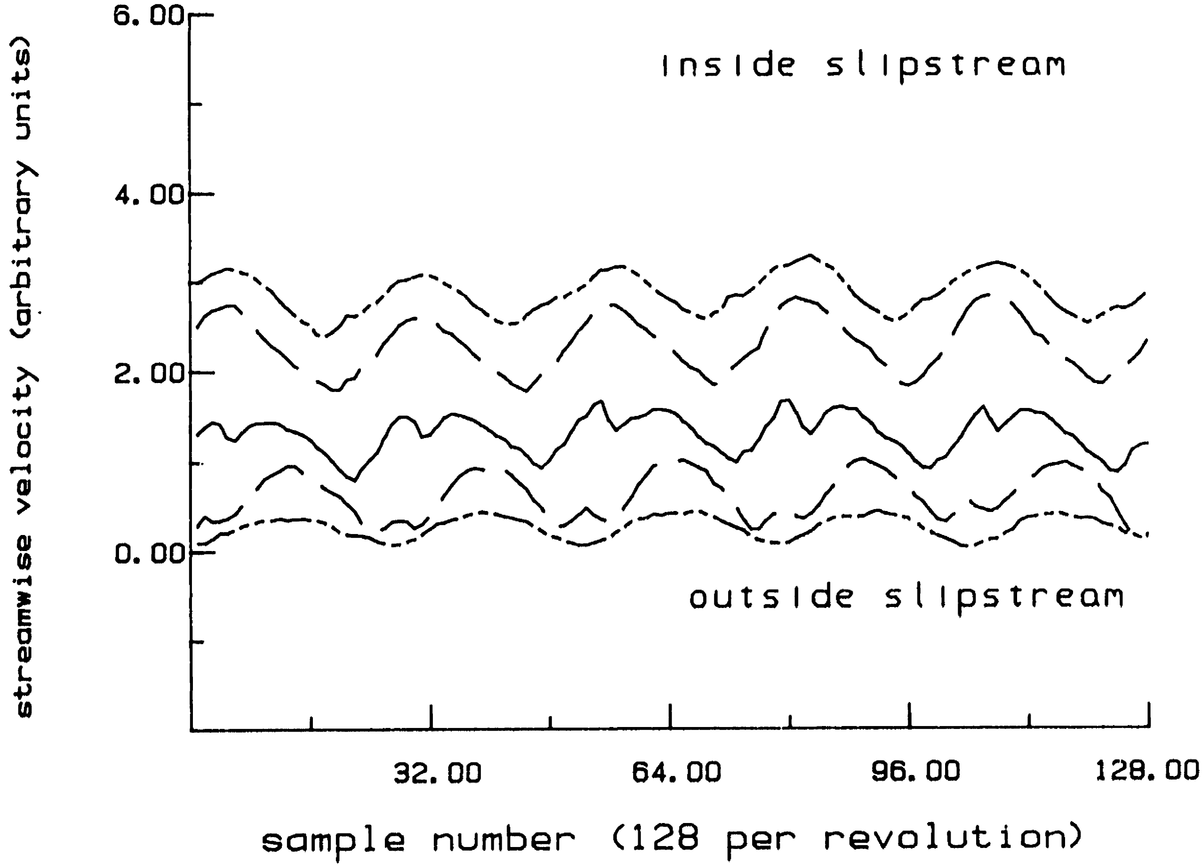

Figure 4.6: Axial velocity recorded during positioning.

The poor quality of the real-time velocity signal necessitated a period of operator training in order to learn to interpret the velocity waveforms. Fortunately, a small region of the tip vortex structure could be made to cavitate without producing massive screen cavitation. This afforded the opportunity to compare positions obtained by the method described above with direct observation. After some hours of training it was possible to obtain consistent results.

4.6 Instrumentation

To employ this indirect measurement technique requires careful triggering and real-time signal processing. Figure 4.7 shows the setup used. A magnet on the drive shaft is sensed by the trigger pickup once per revolution. The pulse from the pickup is compressed in time and amplified. This signal is used to fire a strobe lamp which illuminates the test section of the tunnel. The strobe flash is observed by a photocell whose output is used as the data processing trigger. This triggering setup has the virtue that the variable delay of the strobe can be used to adjust the propeller's angular position during measurements.

For the tip vortex location and strength measurements, a $15mW$ He-Ne laser was employed in back-scatter mode. The photomultiplier signals were aquired and conditioned by a TSI 1057 signal conditioner and TSI 1090 LDA signal processor. These, and the integral monitor, comprise the tracker identified in Figure 4.7. The resulting velocity waveform was sent to a PAR TDH-9 waveform eductor which averaged the signal over several revolutions. The averaged signal, along with the trigger pulse, was observed on a Tektronix 561B oscilloscope during the tip vortex mapping procedure. Concurrently, the velocity signal was captured by a DEC MINC computer and averaged over 800 revolutions. The sampling rate was such that one revolution is represented by 128 points. Another Tektronix oscilloscope was used to monitor the raw photomultiplier signal directly for burst quality.

1	Prop. Shaft	6	Oscilloscope	11	Argon-ion Laser
2	Trigger Pickup	7	Strobe	12	Sig'l Processor
3	Spike Generator	8	Water Tunnel	13	Sig'l Condit'r
4	Oscilloscope	9	Trig. Photocell	14	Monitor
5	V'form Eductor	10	Photomultiplier	15	LDA Tracker

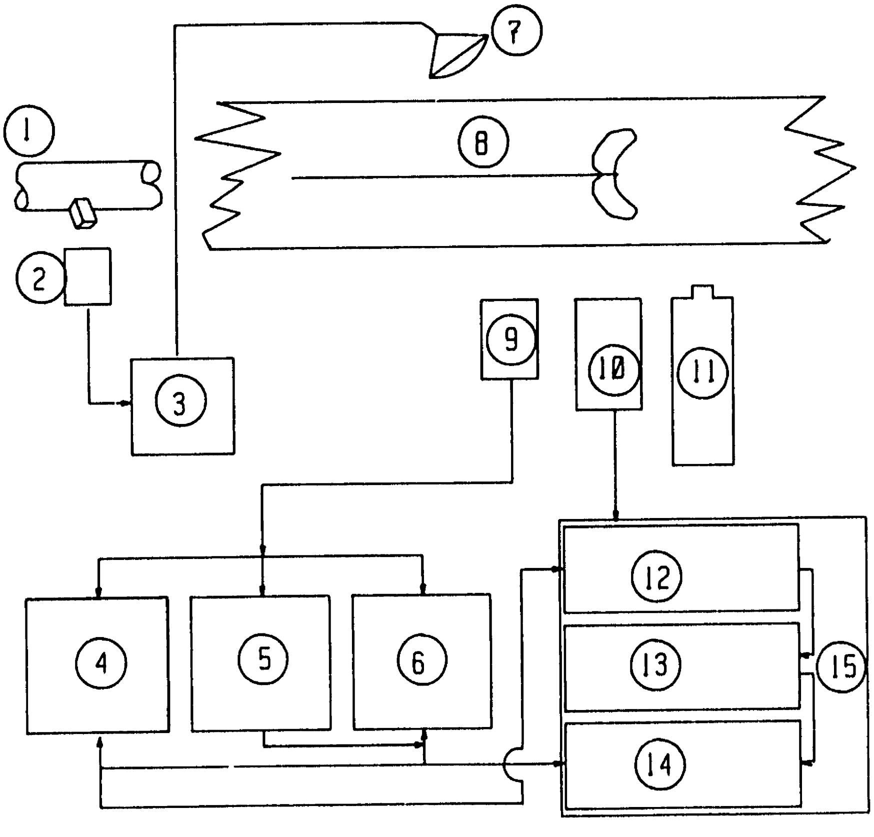

Figure 4.7: Apparatus for tip vortex measurements.

4.7 Tip Vortex Geometry Measurements

Trigger pulse adjustment placed the propeller at a nominal angle of 64.5 degrees during all tip vortex geometry measurements (referred to the coordinate system defined in Figure 3.1 of Chapter (3). The test propeller has 36 degrees of skew so the tip of the corresponding blade was at 100.5 degrees.

Since data-taking would extend over several days it was important to check repeatability. Figure 4.8 shows position data taken for one vortex one two separate days. From this, one can see that day-to-day repeatability is fairly good. Figure 4.9 shows the vortices' positions in the X–Y plane as viewed from the positive Z axis. Note the change in pitch from the upper (slower flow) region to the lower. The contraction of the race is also apparent. Figure 4.10 shows a view of the vortices in the X–Z plane as viewed from the positive Y axis. In this view the effect of the strut jets is evident in the streamwise deflection of the vortices near $Z = 0$. Figure 4.11 shows the same data as Figures 4.9 and 4.10 replotted to display the regions of differing pitch. Finally, Figures 4.12, 4.13, 4.14, 4.15 and 4.16 show these data looking at the Y–Z plane from ahead of the propeller.

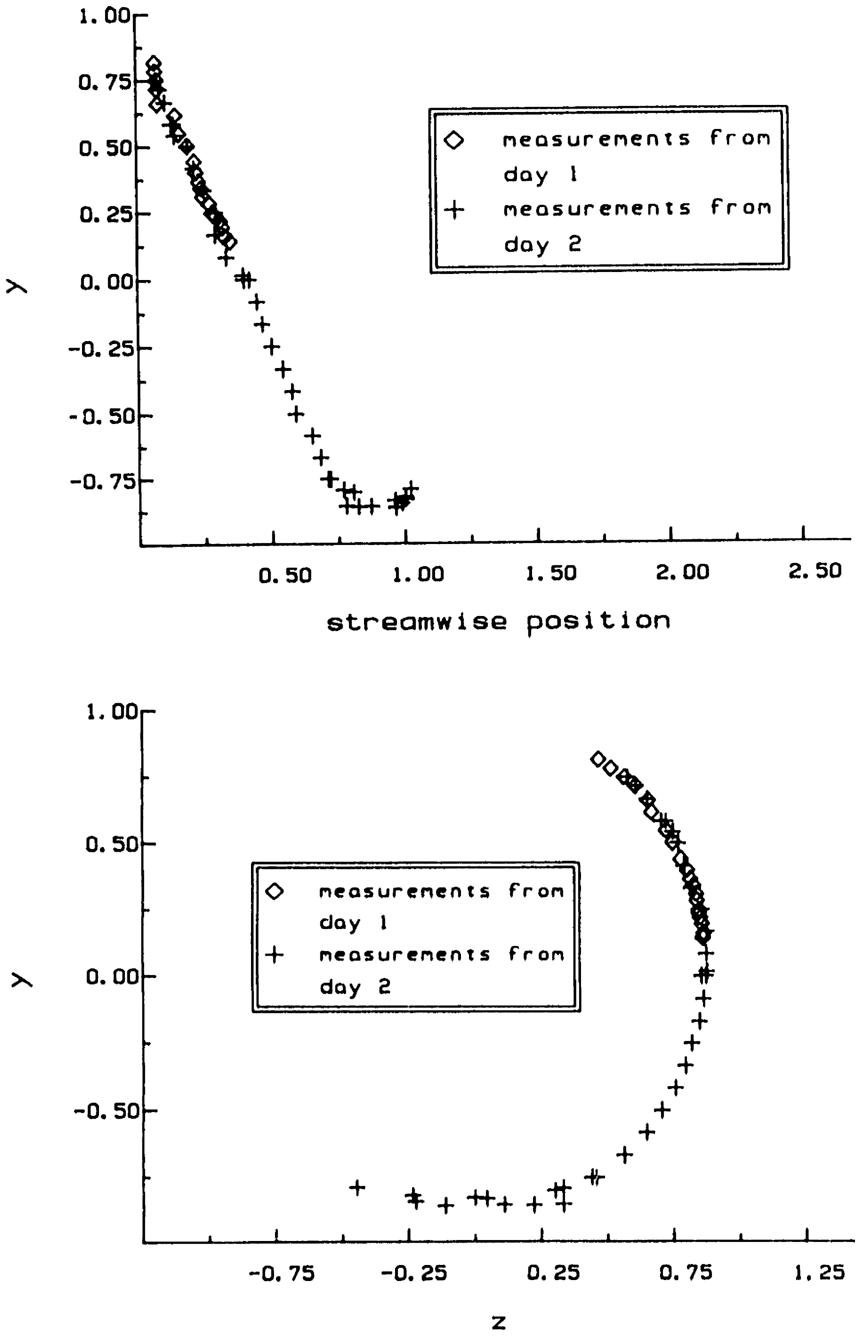

Figure 4.8: Repeatability for vortex geometry measurements.

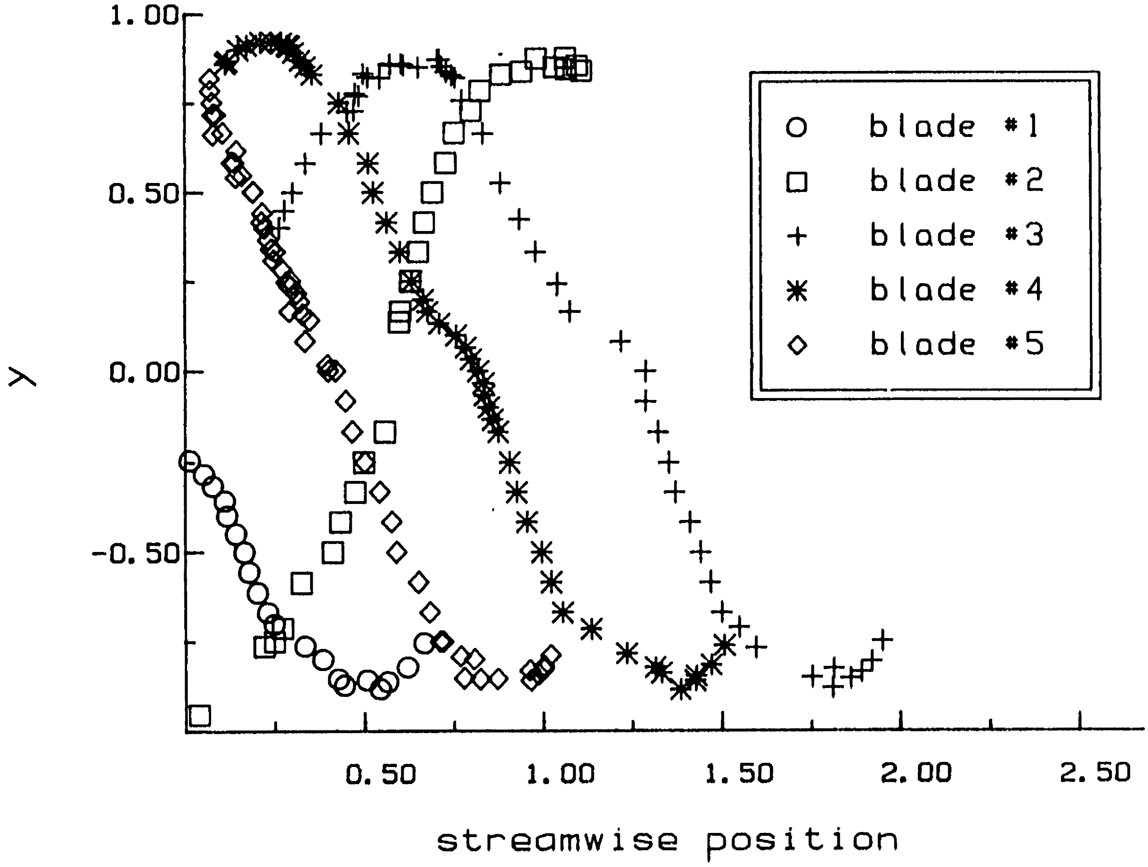

Figure 4.9: Tip vortex geometry in X–Y plane.

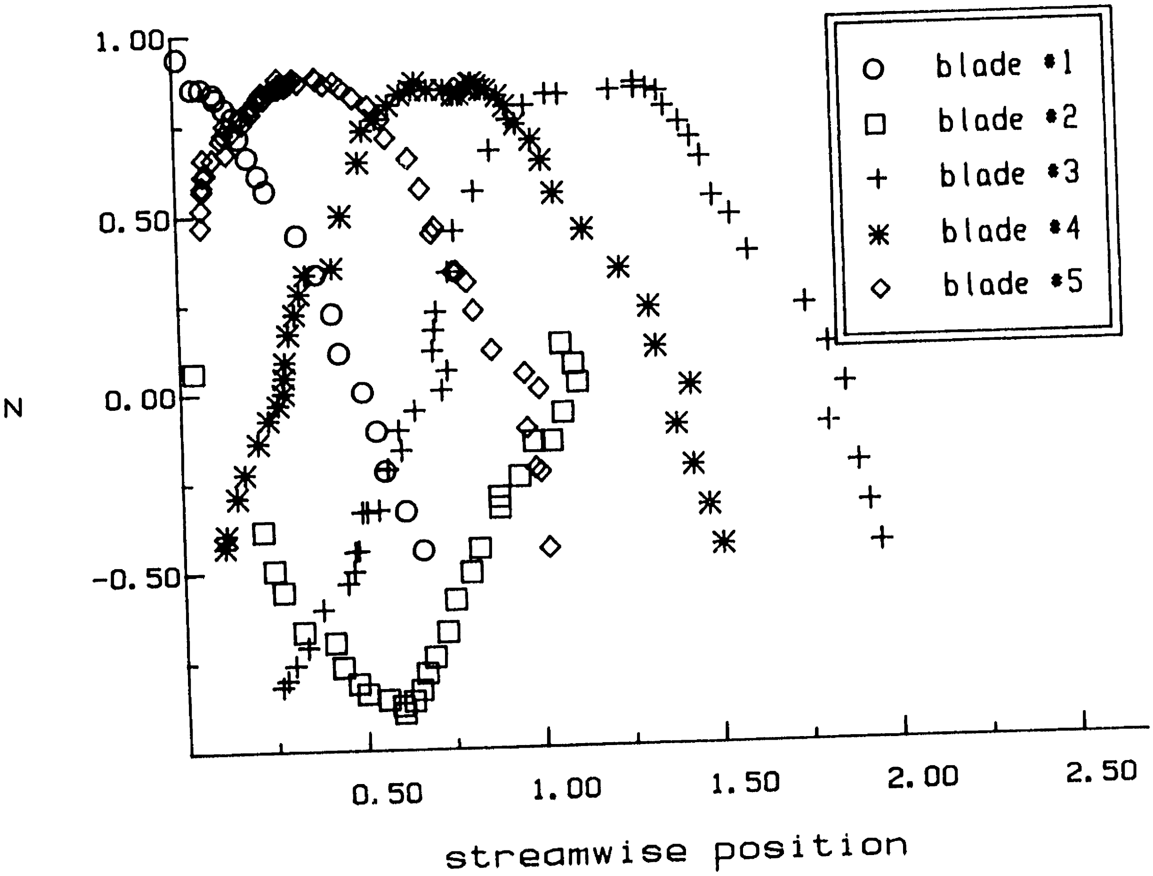

Figure 4.10: Tip vortex geometry in X–Z plane.

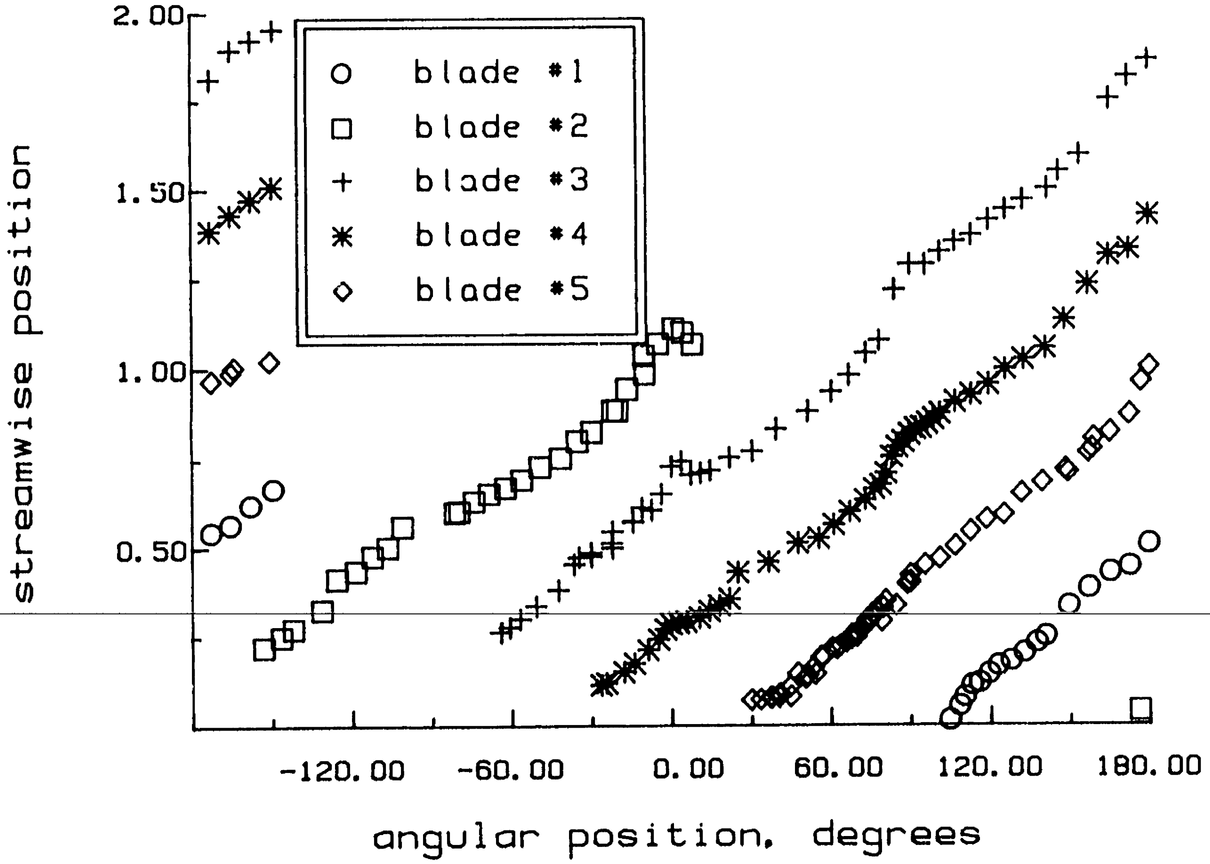

Figure 4.11: Developed view of tip vortices.

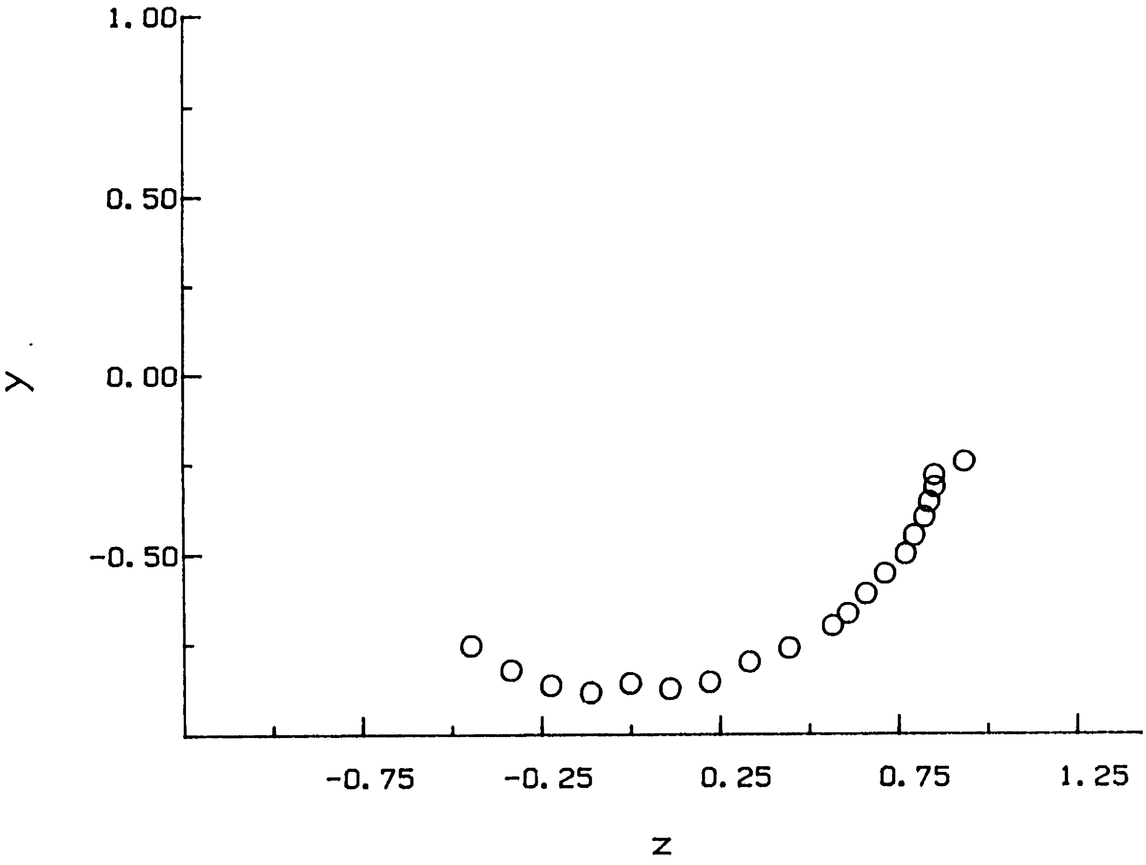

Figure 4.12: Tip vortex geometry in Y–Z plane – blade #1.

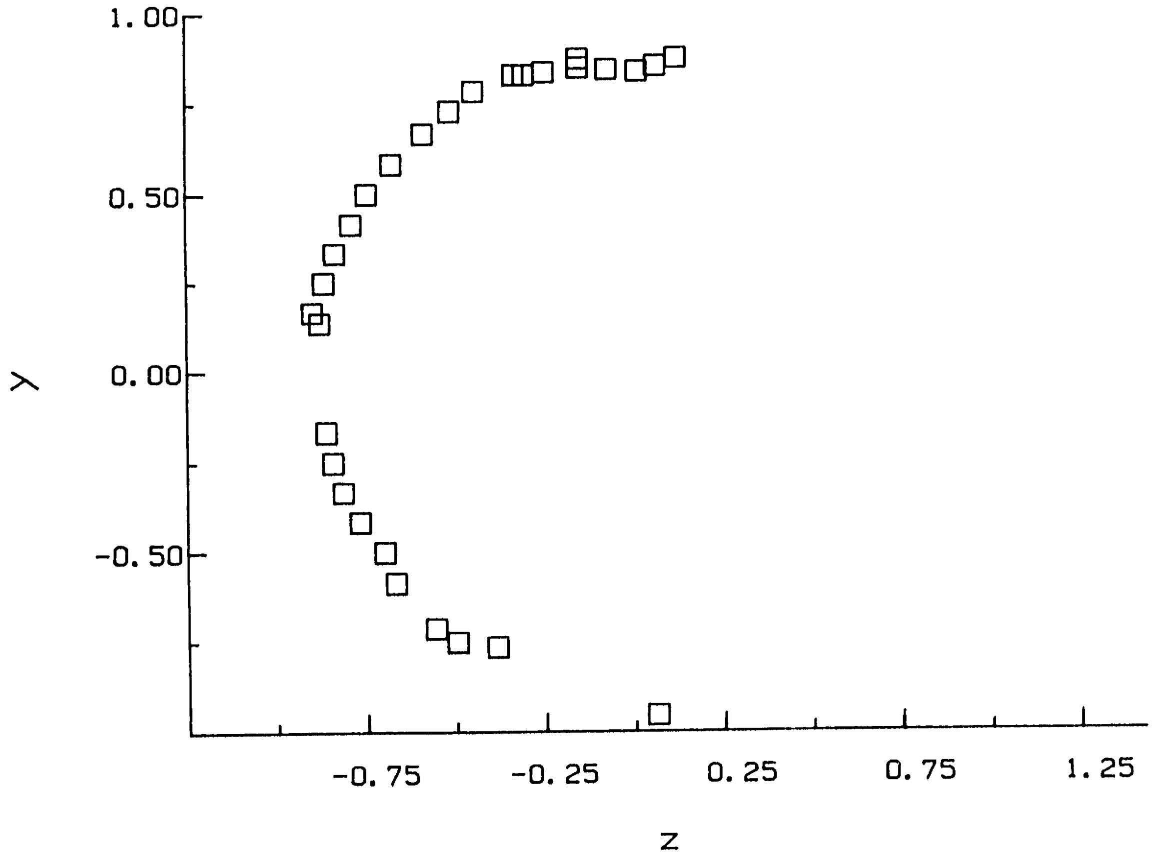

Figure 4.13: Tip vortex geometry in Y–Z plane – blade #2.

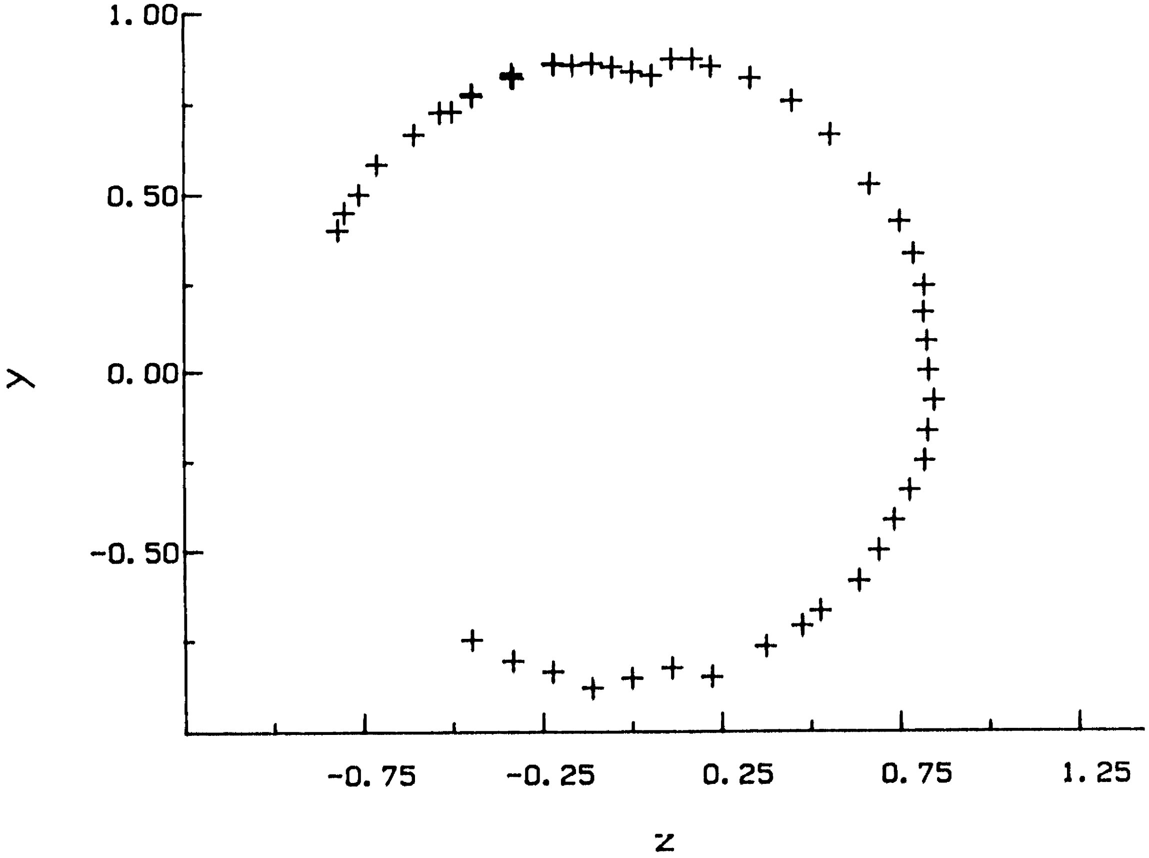

Figure 4.14: Tip vortex geometry in Y–Z plane – blade #3.

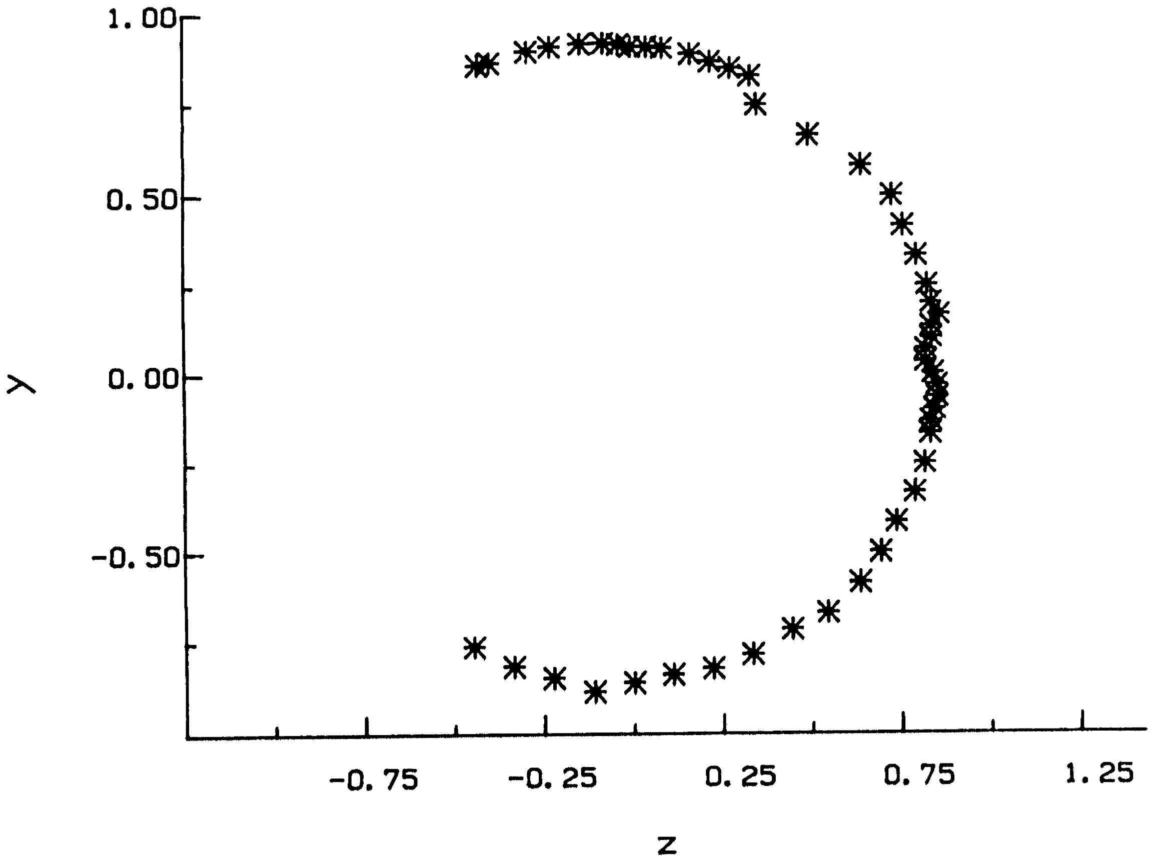

Figure 4.15: Tip vortex geometry in Y–Z plane – blade #4.

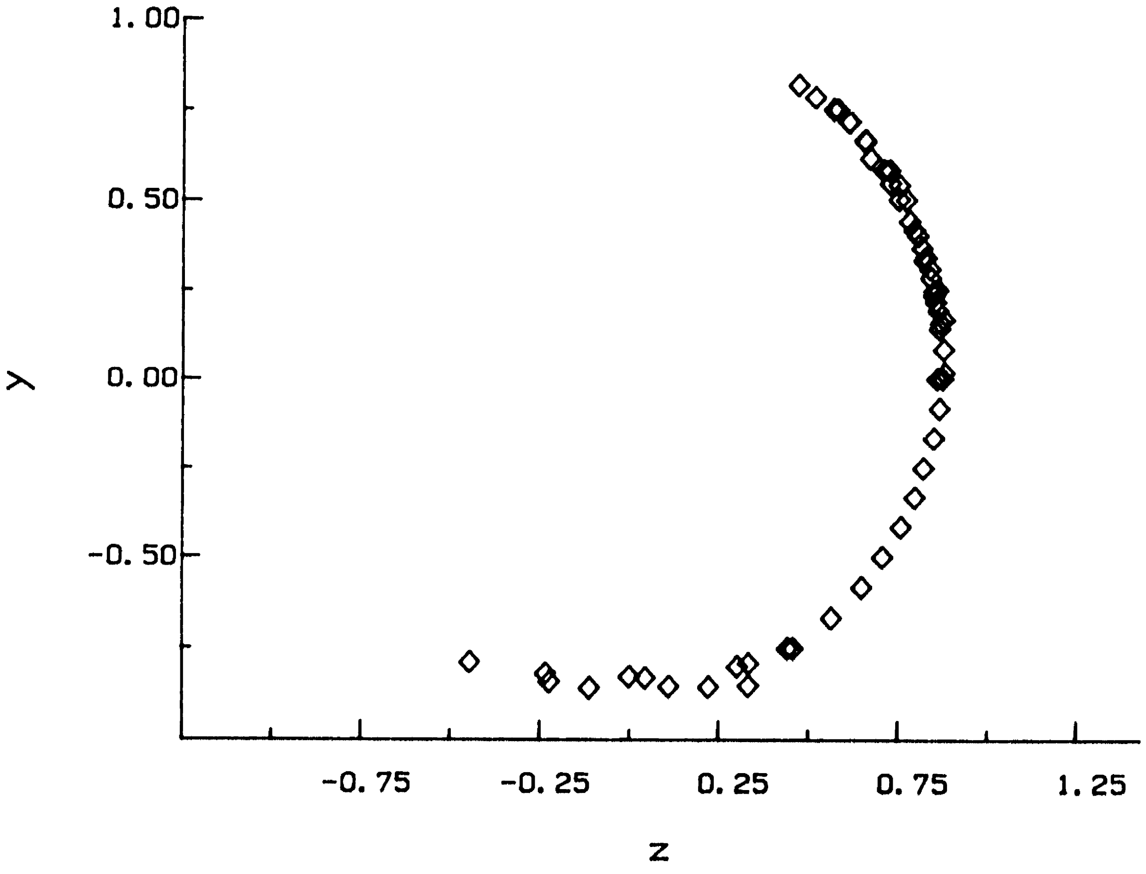

Figure 4.16: Tip vortex geometry in Y-Z plane - blade #5.

Chapter 5

Calculations

The numerical model developed in the earlier chapters of this document has been implemented in a code called PUF5 (for Propeller Unsteady Forces, version 5). Two groups of calculations will be presented in this chapter. The first group comprises various convergence studies while the second group compares the code's results to experimental data.

5.1 Convergence of Blade Forces

The results from a numerical model cannot be completely understood without the perspective lent by study of the scheme's convergence properties. This section will examine PUF5's convergence characteristics. The propeller used for these studies will be an NSRDC 4118. Table 5.1 lists the properties of this propeller. A single blade was used for reasons of economy.

5.1.1 Convergence with number of panels

One of the attractive features of vortex lattice models using the QCM is their rapid convergence. This is exhibited in Figures 5.1 and 5.2 which were obtained using a fixed wake geometry in uniform flow. Overall blade forces are mostly a function of the

Number of blades: 3
Hub/Diameter ratio: 0.2
Expanded area ratio: 0.6
Section meanline : NACA a=0.8
Section thickness Distribution: NACA 66
Design advance coefficient, J_A : 0.833

r/R	P/D	$rake/D$	θ_s	C/D	f_0/C	t_0/D
0.20	1.086	0.000	0.000	0.3198	0.0219	0.0414
0.25	1.085	0.000	0.000	0.3420	0.0227	0.0337
0.30	1.084	0.000	0.000	0.3635	0.0232	0.0282
0.40	1.082	0.000	0.000	0.4048	0.0233	0.0239
0.50	1.080	0.000	0.000	0.4392	0.0218	0.0198
0.60	1.078	0.000	0.000	0.4627	0.0205	0.0160
0.70	1.077	0.000	0.000	0.4622	0.0200	0.0125
0.80	1.075	0.000	0.000	0.4347	0.0197	0.0091
0.90	1.073	0.000	0.000	0.3613	0.0182	0.0060
0.95	1.072	0.000	0.000	0.2775	0.0189	0.004[illegible]
1.00	1.071	0.000	0.000	0.0278	0.0001	0.0001

Table 5.1: Particulars of the NSRDC 4118 propeller.

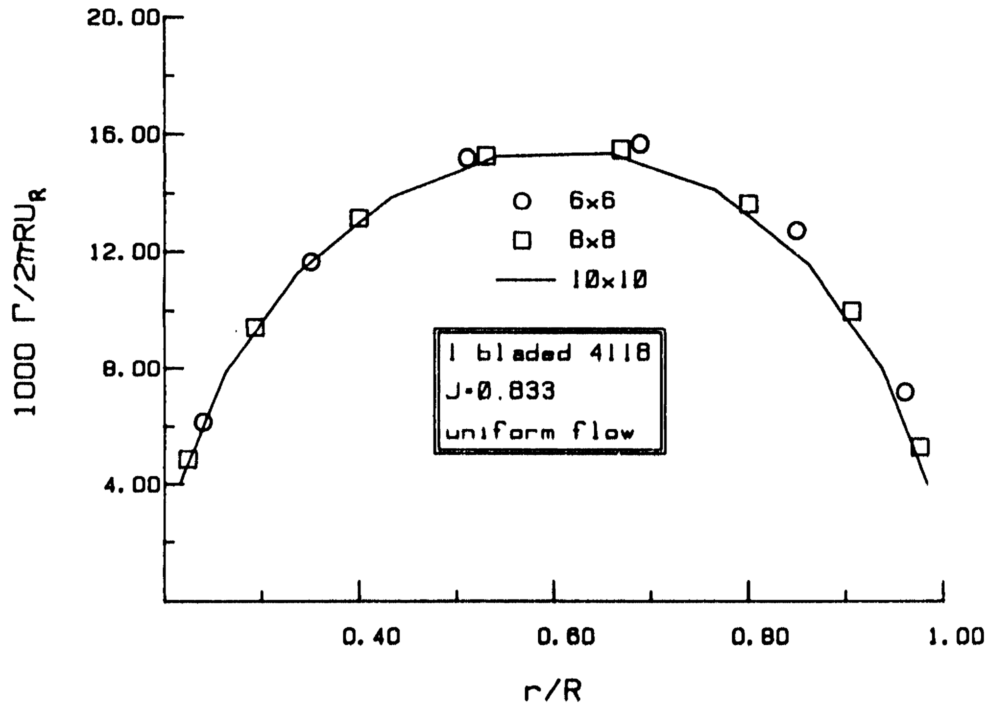

Figure 5.1: Convergence of the spanwise circulation distribution *vs.* number of spanwise panels.

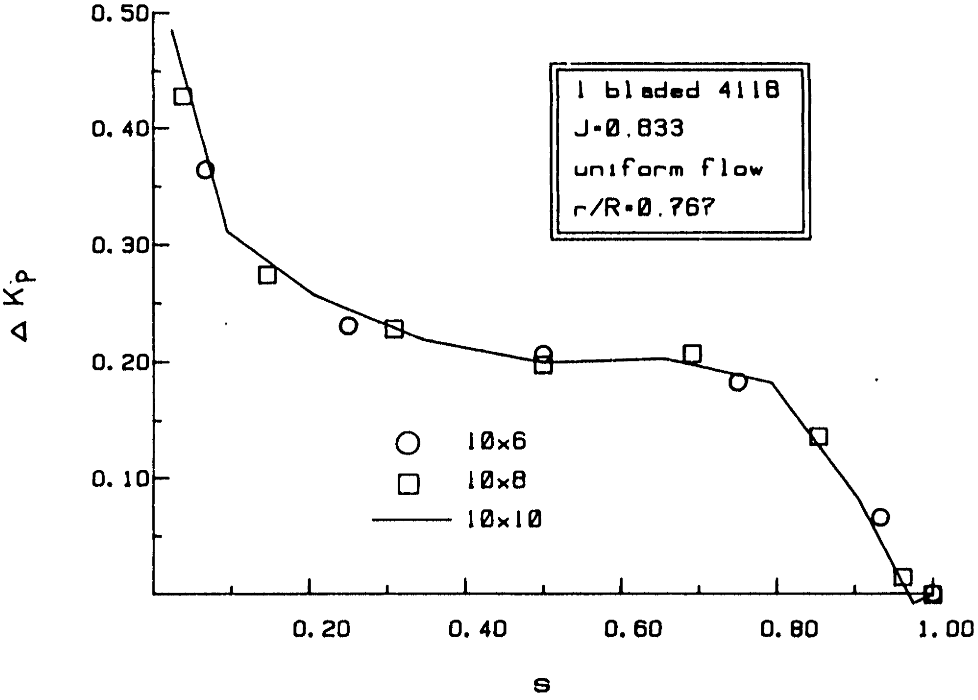

Figure 5.2: Convergence of a typical sectional pressure distribution *vs.* number of panels in the chord.

spanwise distribution of circulation. In this regard, Figure 5.1 is noteworthy showing as it does that even a 6 × 6 grid can give fairly precise results. Figure 5.2 demonstrates the ability of the QCM panelling to capture the flat-plate loading at the leading edge.

In practice, the process is not so simple. It is necessary to iterate the axial and radial traverses several times for each data point. A large number of factors conspire to conceal the clean waveforms of Figures 4.4 and 4.5 from the observer. The vortex location is not exactly repeated from one revolution to the next due to general fluctuations in the flow as well as to the natural instability of the vortex line. The detailed structure of the vortex core differs from the Rankine idealization. There is a vortex sheet shed from the inboard portions of the propeller's trailing edge. This sheet is attached to the tip vortex and is being rolled up into it. There is some phase noise in the triggering mechanism. The LDA traverse carraige was somewhat flexible and permitted fairly large oscillations of the sampling volume (especially in the streamwise direction). Figure 4.6 shows some actual velocity waveforms such as were observed during the positioning process.

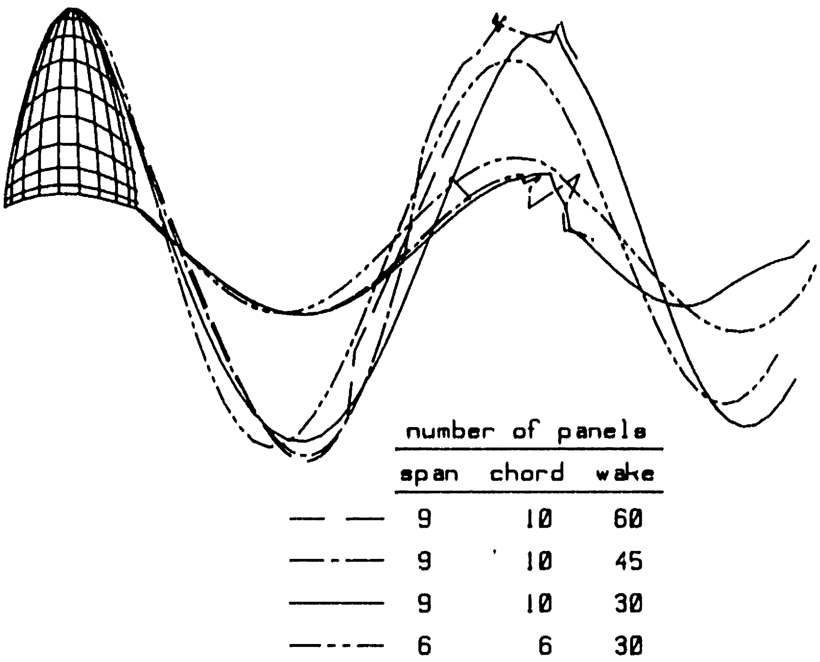

Figure 5.3: Side view of a one-bladed 4118 showing the hub and tip vortex locations for various panellings. J is 0.833, uniform flow from left to right.

is a fixed-wake vortex lattice model that is known to give accurate results for the full 4118 propeller. One expects it to be a good reference for the one-bladed case as well. Figure 5.4 compares PUF2.1's prediction of spanwise circulation with that from PUF5. In this example, PUF5 was run using 9 panels spanwise and 10 chordwise. It also includes the effects of the free wake. Figure 5.5 compares thrust predicted by the two over a range of advance coefficient.

A complete, three bladed 4118 is compared to experimental data in Figure 5.6. This case used 9 panels spanwise, 9 panels chordwise, 30 time steps per revolution and a wake length of approximately 4 propeller radii. One notices immediately that thrust is underpredicted in the heavy load case and overpredicted in the light load case. The error in the former case can be identified with the phenomenon of leading edge vortex separation. As the loading increases, there comes a point when the adverse pressure gradient behind the leading edge produces a separation bubble. This has the effect of rotating the leading edge suction force to a direction normal to the lifting surface at

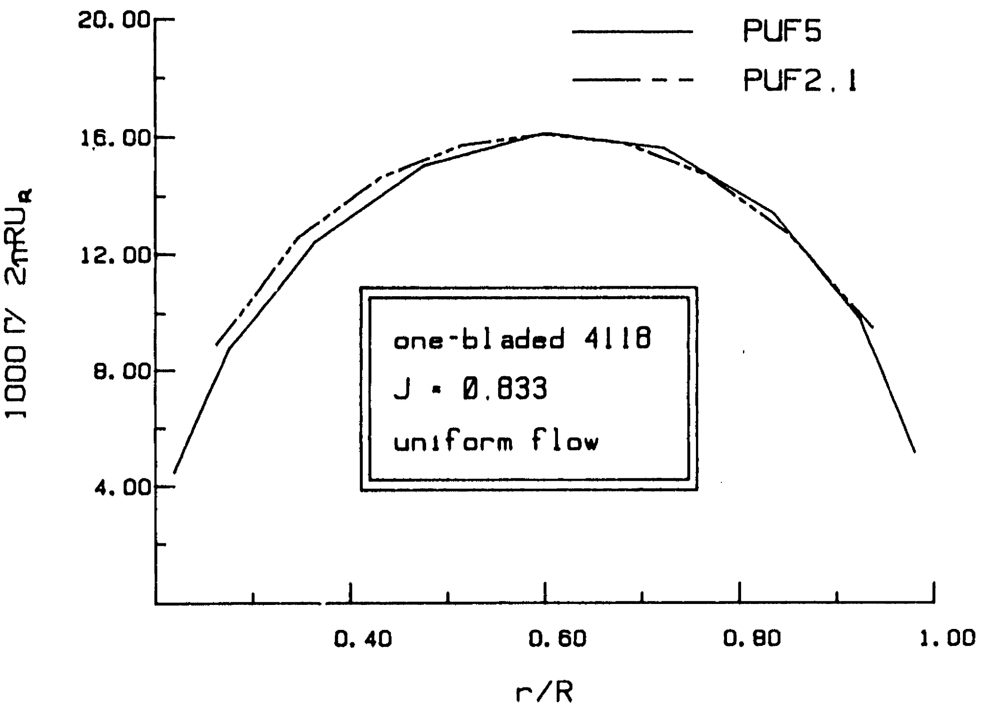

Figure 5.4: Circulation as a function of span for PUF5 and PUF2.1

the leading edge. The thrust is increased, as is the torque. Greeley and Kerwin [22] examined this extensively and have developed a numerical model which accounts for the global effects well.

5.1.3 Convergence *vs.* Time

PUF5 has the option of starting its unsteady calculations from an estimated steady solution or with an impulsive start analogous to the Wagner problem. By selecting the impulsive start, certain issues related to the wake may be illuminated.

First consider convergence to the steady solution. Figure 5.7 shows the circulation at about $0.7R$ as a function of time for 15, 30 and 50 time steps per propeller revolution. The number of panels over the span is fixed at 6. The chordwise panelling is adjusted so that the ratio of the sizes of the last blade panel and the first wake panel is roughly constant. Convergence is virtually complete after a third of a revolution. The different

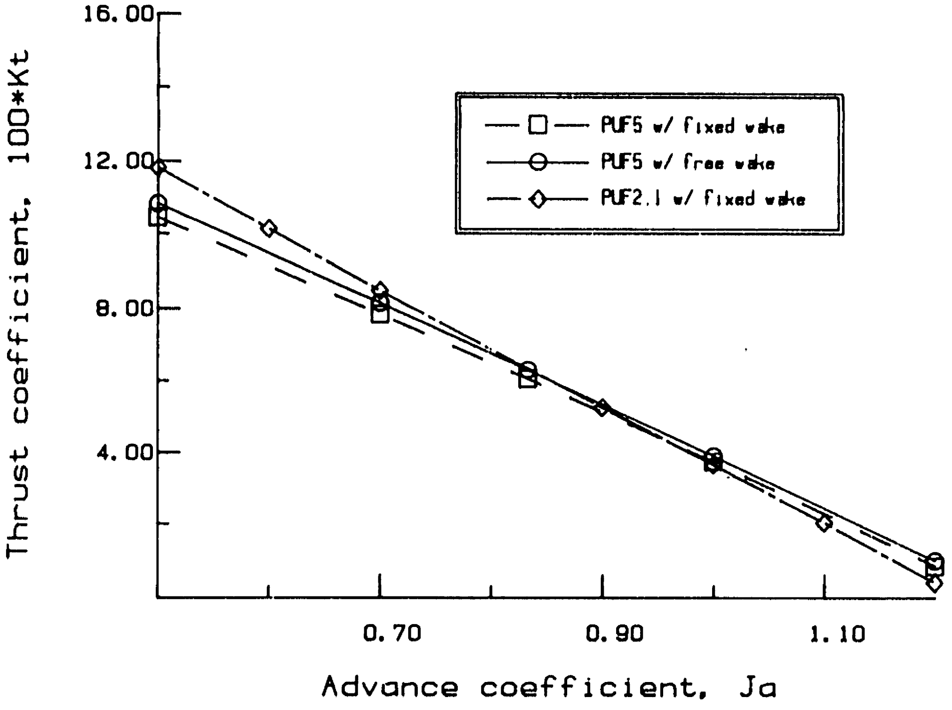

Figure 5.5: Thrust curve for one-bladed 4118 from PUF5 and PUF2.1

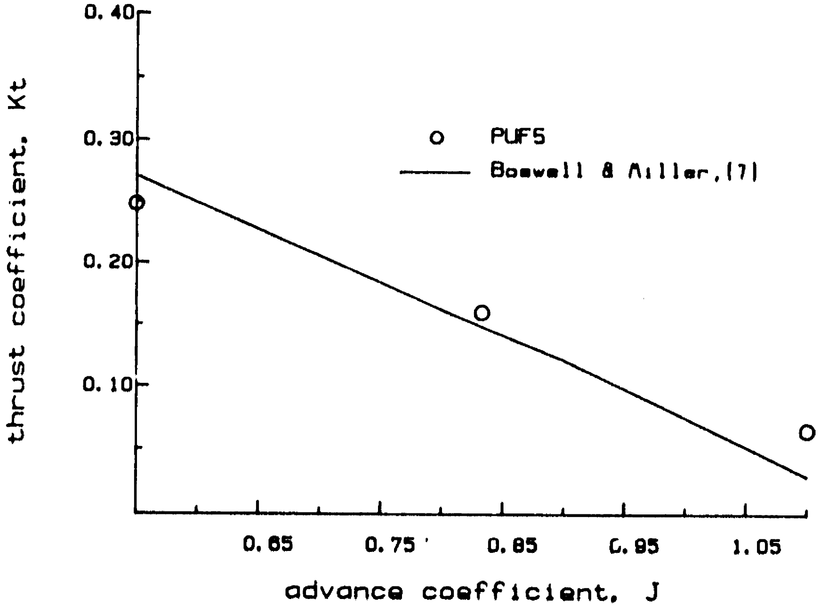

Figure 5.6: Steady thrust for 4118 propeller in uniform flow, free wake case.

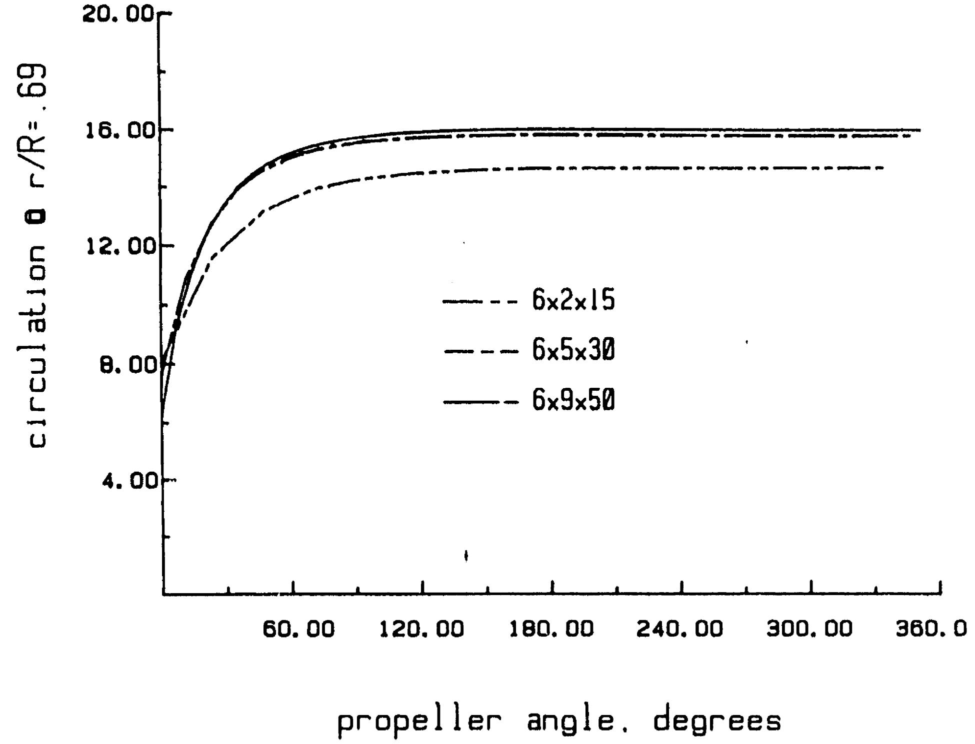

Figure 5.7: Circulation as a function of time at $r/R = 0.69$.

levels achieved has to do with the accuracy of the wake representation. Approximating the wake helix with 15 segments rather than 50 effectively increases the wake contraction which in turn reduces the angle of attack of the blade sections.

The initial values of circulation in Figure 5.7 relate to the streamwise location of the first shed vortex. There is a limit on how near $t = 0$ one can look. Imagine observing an actual foil undergoing such a maneuver. The circulation would be seen to start from zero, rising abruptly as the startup vortex is shed from the trailing edge. The numerical model must represent the cumulative effect of all the shed vorticity produced during one time step as a single discrete vortex. Thus, the earliest time one may examine is approximately $t = O(\delta t)$. This is seen in the figure; smaller time steps produce a smaller initial value of Γ as should be the case. Figures 5.8 and 5.9 show the circulation developed at other radii for the same three panellings. Near the tip, the circulation is fully developed at earlier times. This is the physically correct trend because, for short times, the phenomenon is actually governed by the number of chordlengths the section

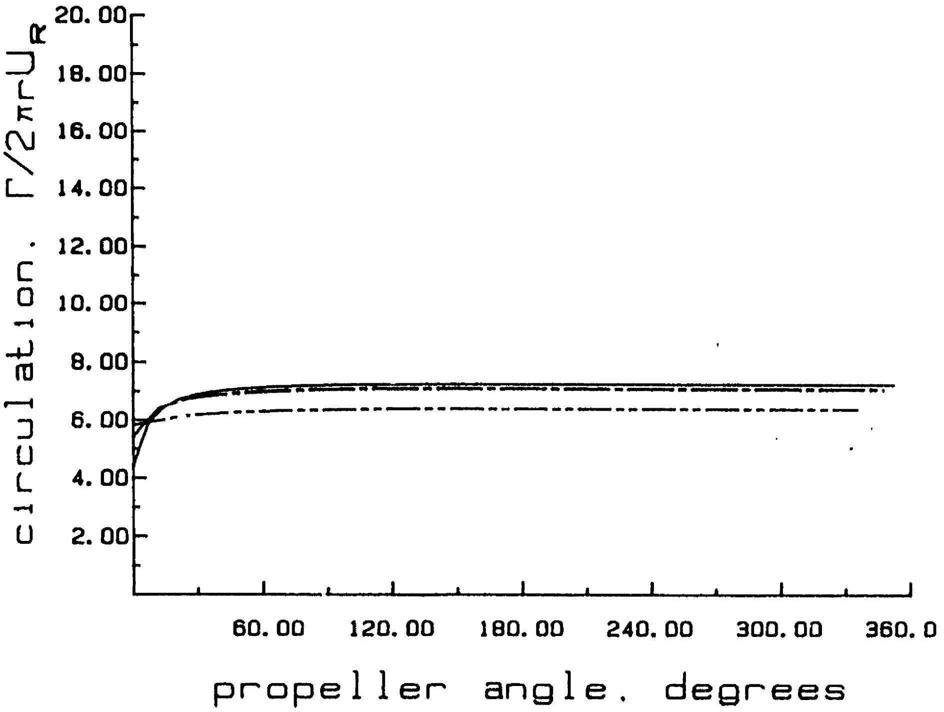

Figure 5.8: Circulation as a function of time at $r/R = 0.96$.

has advanced rather than by the propeller angle. The tip sections, being at a greater radius and normally of smaller chord, travel a greater number of chords per δt.

It was pointed out in Section 3.3 that locating the first shed vortex as a fixed fraction of chordlength leads to erroneous behavior. Figure 5.10 shows results obtained by setting the first wake panel size equal to a fixed fraction of that of the last blade panel. All three calculations were run at 30 time steps per revolution. Figure 5.11 shows corresponding calculations obtained by holding the blade panelling — and the location of the first wake vortex — fixed while varying the time step size. Looking at Figure 5.10, notice that the rate at which circulation is developed varies significantly with the number of chordwise panels as does the initial value of circulation even though the size of the time step is fixed. As for Figure 5.11, one sees that no matter how much the step size is refined, one cannot resolve the earliest development of circulation. These are undesirable behaviors: a marine propeller often is placed in an environment which produces rapid load variations. The magnitude and phase of the circulation response is central to resolving blade forces

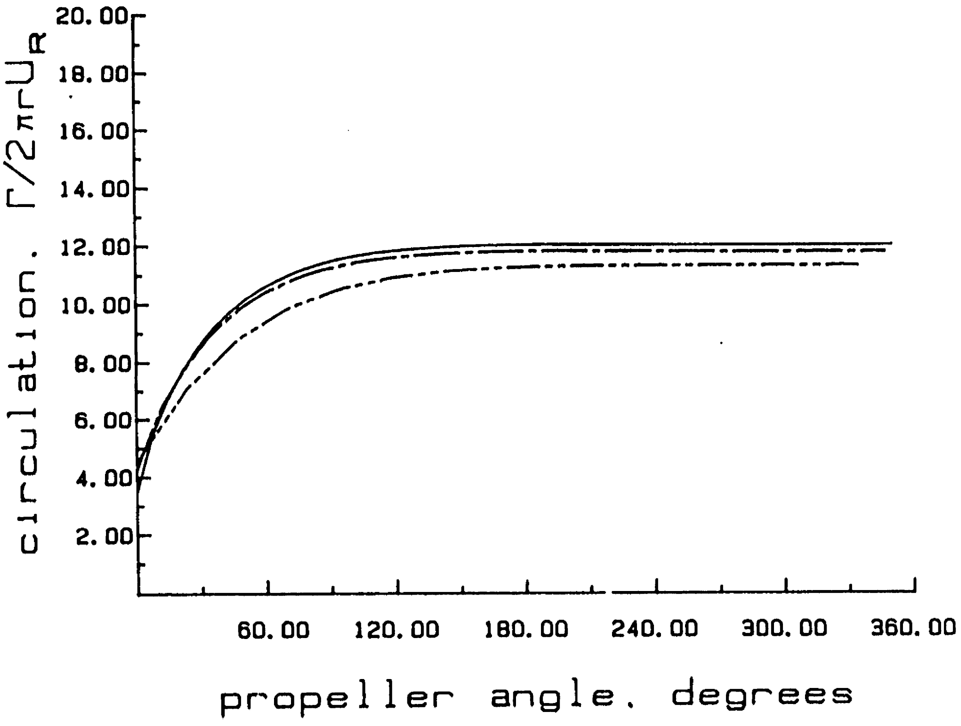

Figure 5.9: Circulation as a function of time at $r/R = 0.35$.

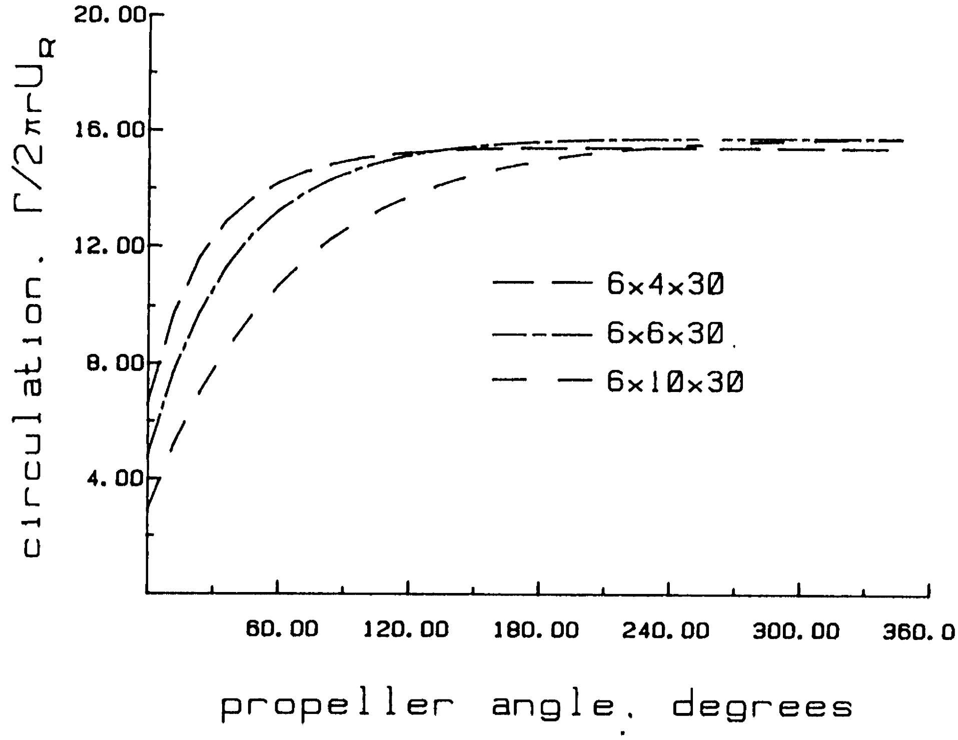

Figure 5.10: Circulation using constant time step size, varying 1^{st} wake vortex location with blade panelling.

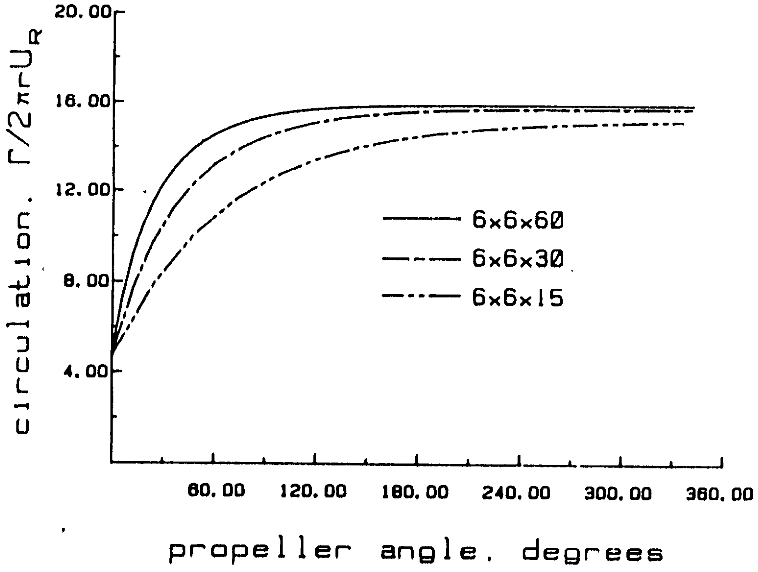

Figure 5.11: Circulation, varying time step size, holding 1^{st} wake vortex location fixed.

Number of blades: 5
Hub/Diameter ratio: 0.2
Section meanline : NACA a=0.8
Section thickness Distribution:
Design advance coefficient, J_A: 0.727

r/R	P/D	$rake/D$	Θ_s	C/D	f_0/C	t_0/D
0.20	0.765	0.00	0.0	0.1846	0.0064	0.0498
0.30	0.803	0.00	0.0	0.2043	0.0174	0.0462
0.40	0.836	0.00	0.0	0.2220	0.0252	0.0415
0.50	0.864	0.00	3.0	0.2369	0.0305	0.0356
0.60	0.862	0.00	10.7	0.2478	0.0327	0.0284
0.70	0.825	0.00	23.4	0.2522	0.0323	0.0203
0.80	0.746	0.00	39.2	0.2454	0.0292	0.0143
0.90	0.610	0.00	55.4	0.2139	0.0223	0.0096
1.00	0.400	0.00	72.0	0.0000	0.0100	0.0060

Table 5.2: Particulars of the OBO propeller.

into shaft side forces and moments.

Before leaving the impulsive start problem, consider Figures 5.12 and 5.13. These are results obtained from an impulsive start calculation for one blade of the propeller described in Table 5.2. Figure 5.12 shows the thrust developed during an impulsive start compared to that part of the thrust generated by circulation alone, the latter obtained by setting $\partial\varphi/\partial t = 0$. Here one sees that, as in the classical Wagner problem, there is an immediate, finite thrust developed from the $\partial\varphi/\partial t$ term in Bernoulli's equation even though the circulation is negligible.

Finally, Figure 5.13 shows another way to look at convergence of circulation during runup to the steady state. Plotted here is the log of the maximum change of any Γ^S from one time step to the next:

$$GDIF = \max_{n,m}\{|\Gamma^S_{n,m}(t) - \Gamma^S_{n,m}(t - \delta t)|\}.$$

This is actually a much more sensitive indicator of convergence and is not always so well behaved. The blade in this case happens to be fairly lightly loaded; for heavily loaded propellers the wake geometry tends to remain unsettled longer causing ultimate

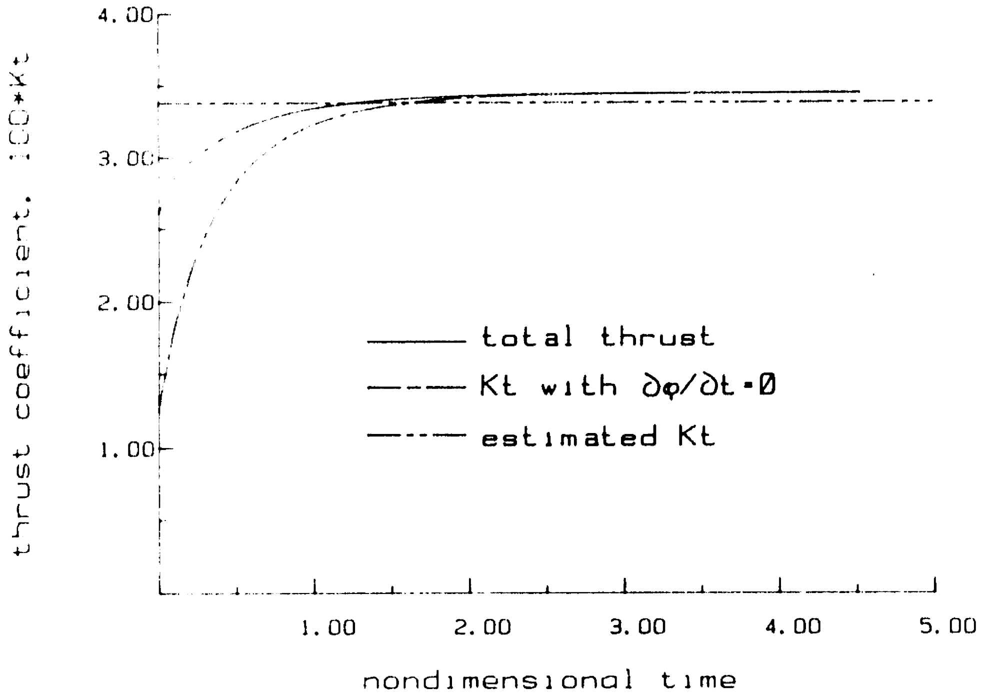

Figure 5.12: Thrust developed during an impulsive start in uniform flow.

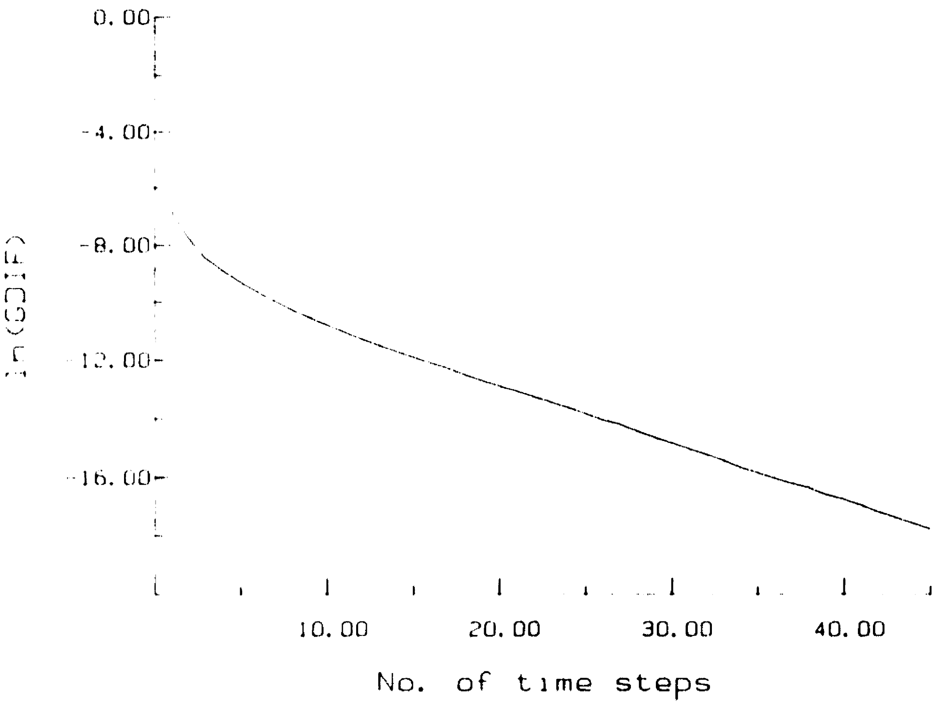

Figure 5.13: Convergence of circulation during an impulsive start.

convergence to be delayed.

5.1.4 Tip vortex core size

In Chapter 2, the local induction of a vortex filament was introduced as a correction to the behavior of the vortex wake at its edges. Loukakis [48] found this term to be essential to predicting the steady wake pitch. Recall from equation (2.27) that the relevant contribution involved a $\ln(1/\varepsilon)$ behavior where ε is identified as the tip vortex core radius.

To compute this radius as part of the solution would require a detailed viscous flow model similar to that developed by Govindan, *et. al.* that could capture the development of the core structure from the boundary layer behavior on the blade . Its subsequent evolution might then be treated using the methods of Ting, say. Fortunately, such detailed calculations aren't necessary for the present model.

Loukakis, in his studies of the fully developed wake structure, performed extensive

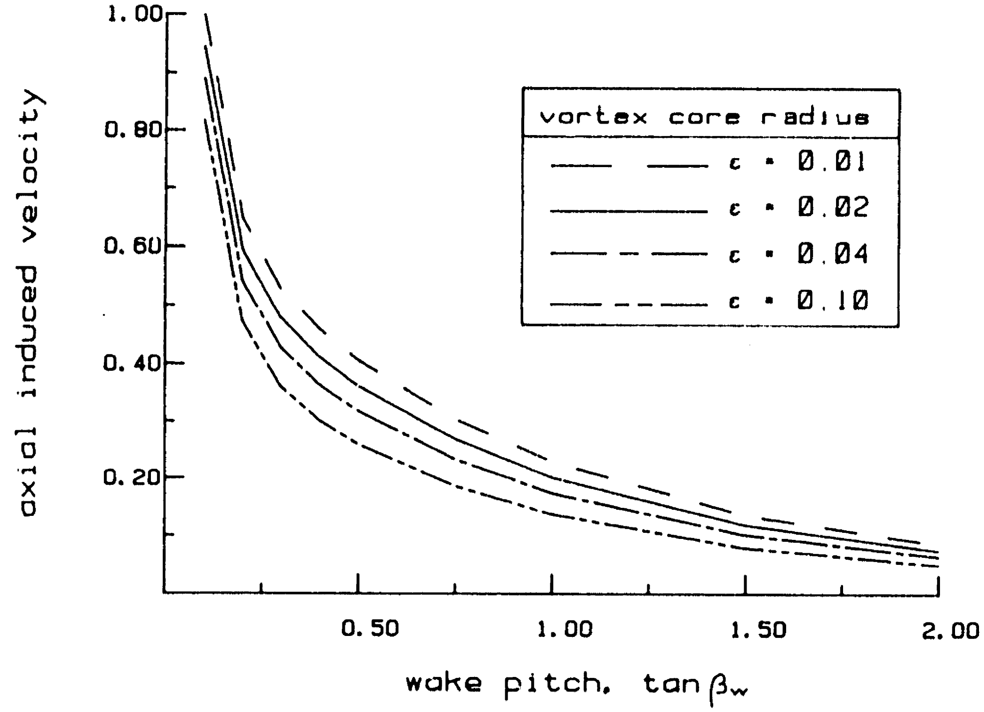

Figure 5.14: Self-induced axial velocity of an infinite helical filament including local effects.

calculations looking at the effect of the local induction on the wake pitch. Modelling the fully developed wake as a constant radius helical vortex filament of infinite extent, he computed self-induced velocities on the vortex. His calculations were done by fitting a circle to the helix at the point of interest, computing the induction from an arc of the circle using Lamb's classical result, and adding in the helix' far field induction by numerical integration. Some of these calculations have been repeated here with the LIA part calculated analytically for the helix. The results for axial velocity as a function of helix pitch are shown in Figure 5.14. As expected, these are virtually identical with Loukakis' data. Figure 5.15 shows more directly the dependence on ε. The induced velocities are only weakly dependent on core radius: an order of magnitude change in ε produces only small changes in u_a. These data were obtained using a wake pitch of $\tan\beta_w = 0.4$.

Employing the LIA approximation requires piecing together an inner and an outer solution. This naturally involves the matching length L appearing in equation (3.72).

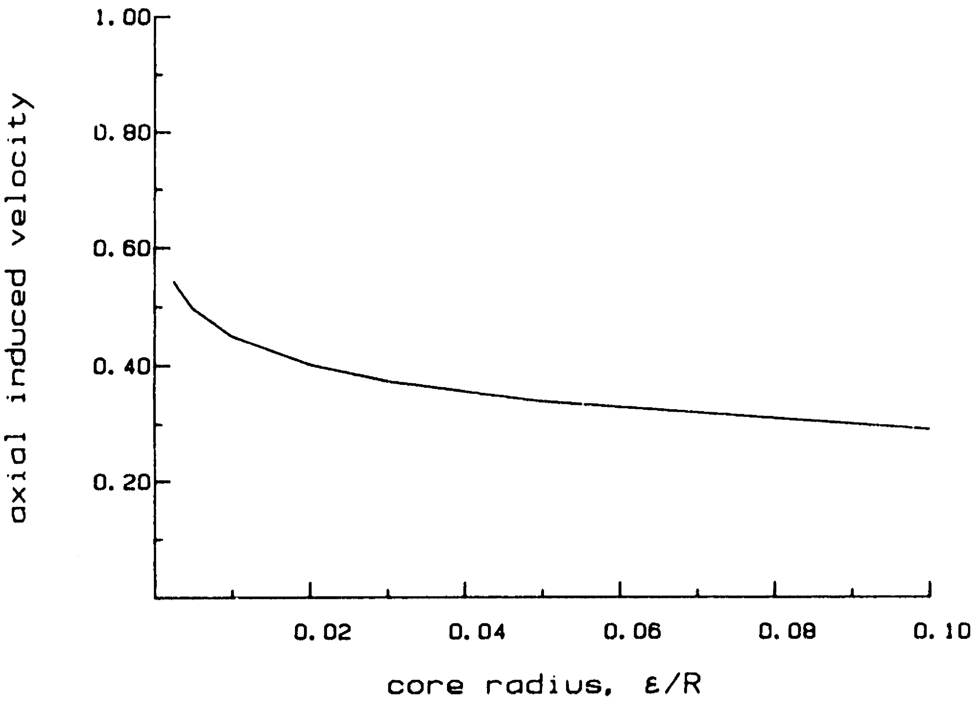

Figure 5.15: Sensitivity of self-induced velocity to core radius.

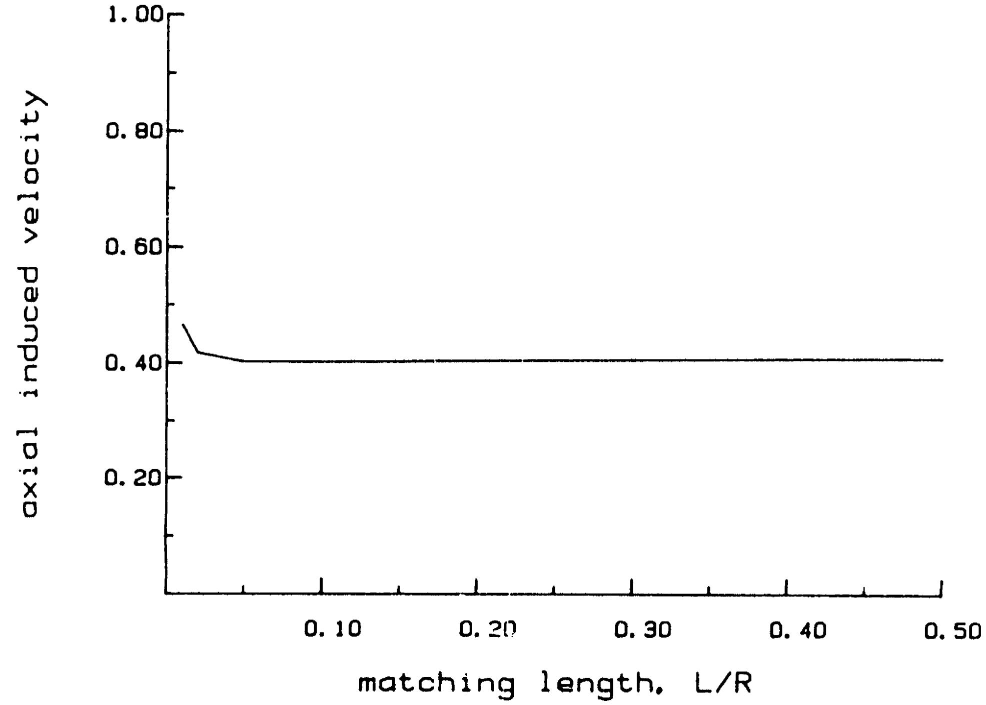

Figure 5.16: Sensitivity of self-induced velocity to matching length.

Calculations to check sensitivity to changes in L were done for a wake pitch of $\tan\beta_w = 0.40$ with a core radius of 0.02 times the helix radius. Figure 5.16 shows that matching length has virtually no effect.

All of the foregoing is presented in order to make a case for the following: if a reasonable guess for ε can be made it is good enough for the present application. This estimate may be approached from two directions. First, there is phenomenological evidence. Loukakis and later, Greeley and Kerwin [22], found good agreement with experimental wake pitch data with $\varepsilon = 0.02R$ although they had to estimate the strength of the tip vortex making it hard to separate the effects. Second, there is analytical evidence. Using energy arguments with an outer potential flow and an inner viscous model of the tip vortices from a wing, Roberts [67] was able to calculate the radius of maximum velocity which is identified here as the core radius. It is $\varepsilon = 0.018R$.

With regard to the streamwise variation of ε, it should be noted that casual direct observation in the propeller tunnel seems to indicate that the core radius may be considered constant over almost the whole length of the tip vortices. This is buttressed by Roberts' calculations which indicate that the region of persistence of the vortex core structure is on the order of ten spans. A core radius value of $0.02R$ is used in the present work at all positions along the vortex.

5.2 Unsteady Problems

The full unsteady code was tested against two groups of experimental data. In one case, comparison is made to unsteady force measurements. In the other case, computed wake geometry is matched against data from the measurements described in Chapter 4. Lastly, PUF5 is applied to the case of a five bladed propeller operating in a ship wake with an extreme wake defect.

5.2.1 Forces on the 4118 propeller

Boswell and Miller [7] studied unsteady loading on a series of propellers that included the 4118 described above. They tested the propellers in wakes generated from wake screens constructed to produce square wave azimuthal variation in the flow. Two screens were used, with periods $2\pi/3$ and $2\pi/4$. Unsteady thrust and torque were measured and harmonically analyzed.

PUF5 was run for each case using nine panels spanwise, nine chordwise and thirty panels streamwise in the wake. There were forty-five time steps per revolution. Integration of the wake trajectory was accomplished in a three part process within each time step. First, forward Euler was applied with step size δt and the result saved. Next, forward Euler was twice applied starting from the original position using a step size of $1/2\delta t$. Finally, Richardson extrapolation was applied to the two results to obtain the new wake position with second order accuracy in time.

The results are summarized in three figures showing propeller forces in an inertial reference frame. Figure 5.17 resolves the axial force into harmonics of shaft rate. Since

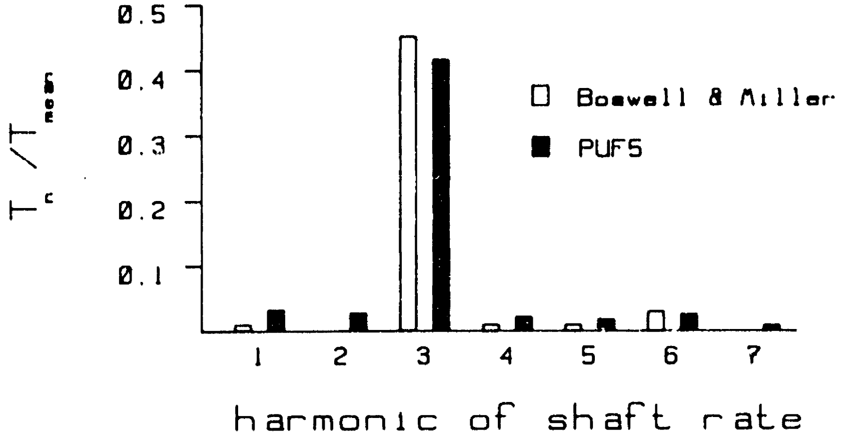

Figure 5.17: Thrust harmonics for 4118 propeller in a three cycle wake.

this is a three-bladed propeller in a three cycle wake, the third harmonic dominates. Figures 5.18 and 5.19 refer to the four cycle wake. Here the third harmonic dominates as well. The experimental data shows strong mean value, particularly in the vertical force, which does not appear in the PUF5 data. Boswell and Miller attribute this to the weight of the propeller and shaft. The appearance of a first harmonic in both side forces is apparently due to a mean side force measured in the rotating reference frame. The origin of the 20 per cent discrepancy in the third harmonic of horizontal side force is not clear.

5.2.2 Tip vortex geometry from the 4497 propeller

The velocity profile measured in the propeller plane, presented as Figure 4.2, was provided as input to PUF5 in the form of Fourier harmonics. Table 5.3 lists these. Only coefficients for axial velocity are given. The axial inflow velocity is calculated as

$$V_x = V_s \sum_n \left[A_n \cos(n\theta) + B_n \sin(n\theta) \right].$$

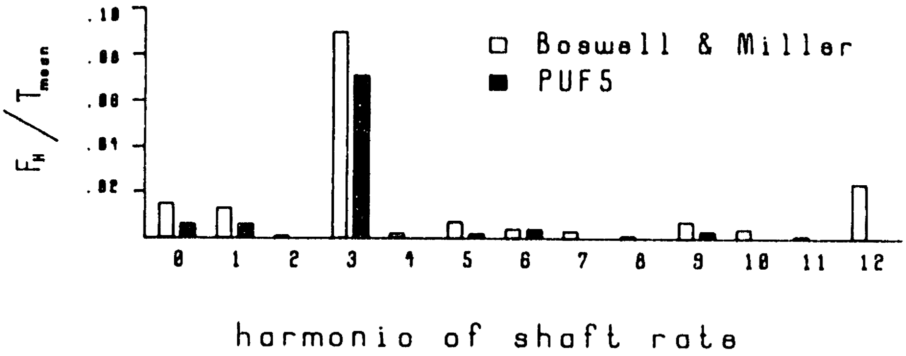

Figure 5.18: Horizontal side force on the 4118 propeller in a four cycle wake.

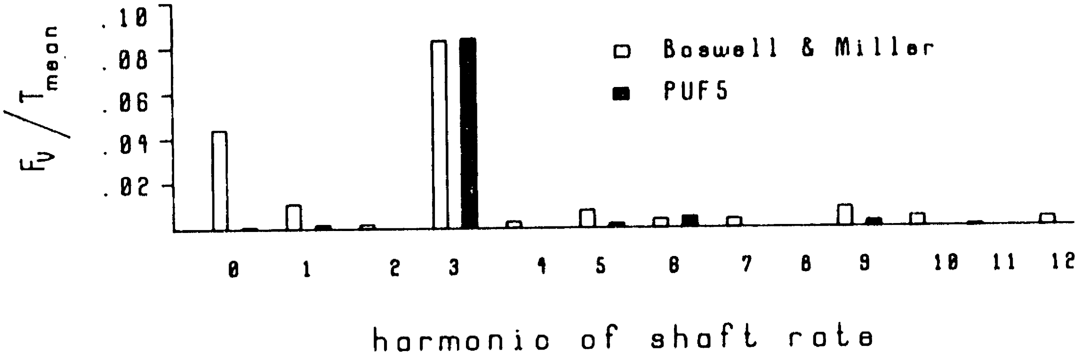

Figure 5.19: Vertical side force on the 4118 propeller in a four cycle wake.

r/R	0.25		0.30		0.40		0.50		0.60	
n	A_n	B_n	A_n	B_n	A_n	B_n	A_n	B_n	A_n	B_n
0	1.045	0.000	1.044	0.000	1.037	0.000	1.013	0.000	1.006	0.000
1	-0.065	-0.003	-0.076	0.001	-0.098	-0.002	-0.110	0.000	-0.120	0.004
2	-0.042	-0.003	-0.028	-0.009	-0.006	-0.006	-0.009	-0.007	-0.006	-0.007
3	0.021	-0.009	0.016	-0.004	0.021	-0.012	0.032	-0.014	0.039	-0.005
4	0.034	-0.004	0.039	-0.005	0.053	-0.002	0.049	-0.002	0.052	0.003
5	0.002	-0.012	0.000	-0.009	0.006	-0.015	0.001	-0.016	0.003	-0.011
6	-0.004	-0.003	-0.001	-0.001	0.000	-0.001	-0.001	-0.002	0.001	0.000

r/R	0.70		0.80		0.90		0.95		1.00	
n	A_n	B_n	A_n	B_n	A_n	B_n	A_n	B_n	A_n	B_n
0	0.999	0.000	0.987	0.000	0.986	0.000	0.975	0.000	0.975	0.000
1	-0.120	-0.001	-0.122	-0.003	-0.125	-0.002	-0.127	-0.002	-0.124	-0.001
2	-0.015	-0.006	0.005	0.000	-0.008	0.001	-0.005	0.002	-0.002	0.006
3	0.034	-0.006	0.041	-0.009	0.038	-0.004	0.046	-0.002	0.052	-0.002
4	0.046	-0.004	0.030	-0.002	0.043	-0.002	0.034	-0.003	0.032	-0.004
5	-0.004	-0.008	-0.002	-0.008	-0.001	-0.005	-0.003	-0.001	-0.004	-0.002
6	-0.002	-0.001	0.002	-0.002	0.000	-0.002	0.000	-0.001	0.001	-0.002

Table 5.3: Harmonic analysis of screen-generated wake profile.

The propeller used in the experiment was modelled by PUF5 using nine panels over the span, nine chordwise, and thirty along the streamwise direction in the wake. There were forty-five time steps per revolution. The calculation was started from an estimated steady solution to speed convergence. Two revolutions were executed.

Figure 5.20 shows the experimental data overlayed onto the calculated tip vortex locations from PUF5. Flow is from left to right and the low speed region of the flow is in the upper half of the plot. No interpolation of the tip vortices' positions was deemed necessary since the propeller angle at one time step nearly matched the experimental propeller position. The overall features of the experimental data are reproduced. In particular, the different pitch in the two inflow regions is captured. Figure 5.21 shows this in a different view. One can also see the effect of the jet flow at zero and 180 degrees.

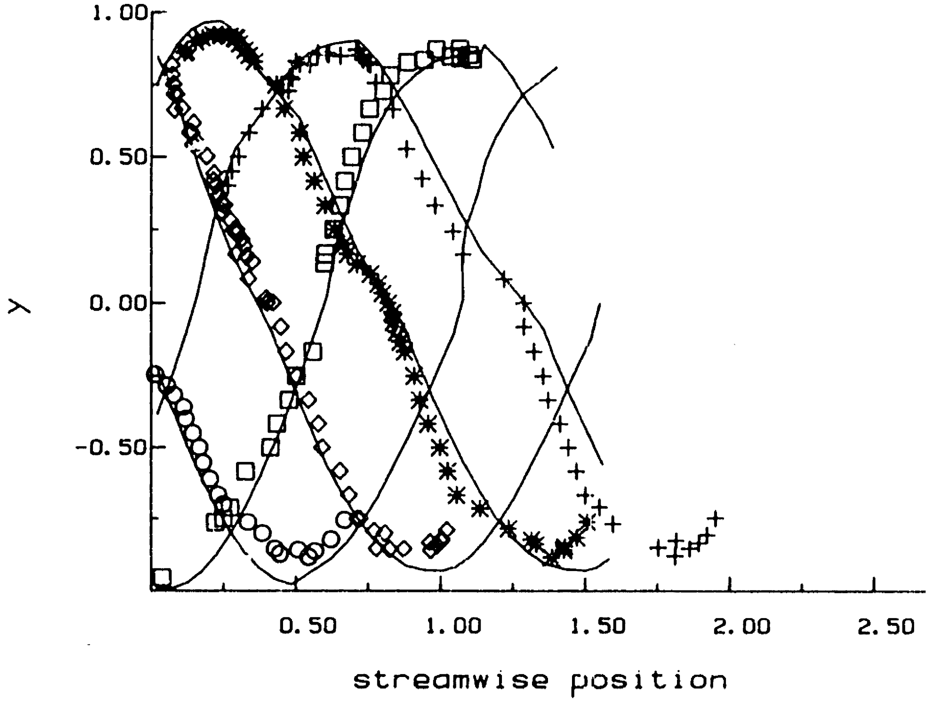

Figure 5.20: Tip vortex structure of the 4497 propeller operating in a screen-generated wake.

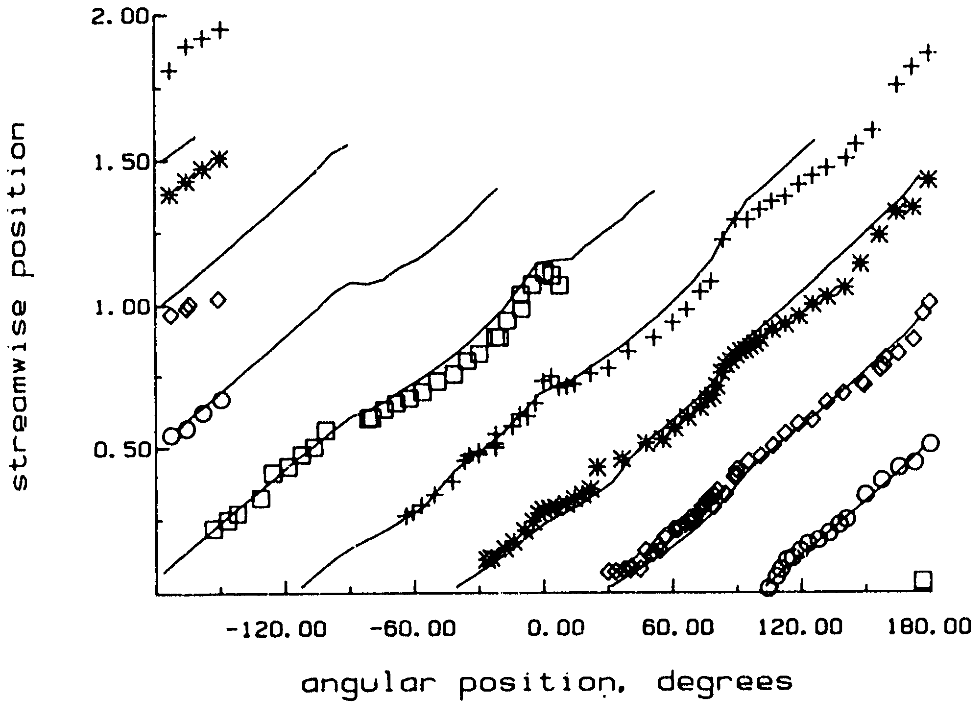

Figure 5.21: Pitch of the tip vortices.

There are two discrepancies that should be noted. The radial contraction of the slipstream is under-predicted. Some part of this is likely due to the truncation of the wake. There would also be a contribution if the calculated rollup is proceeding too slowly since during rollup the tip vortex tends to migrate inboard. The other discrepancy is that the pitch is slightly overpredicted. It doesn't seem very significant at first glance but if one were to add a far-wake model to improve the radial contraction it would increase the pitch further. There would be an indirect effect: the induction at the propeller plane added by the far wake would reduce the loading. Weaker tip vortices would result in less pitch.

5.2.3 The wake from a helicopter rotor

Virtually all three dimensional free wake analyses known to the author comes from the aerodynamics field. That portion most closely related to this work has to do with

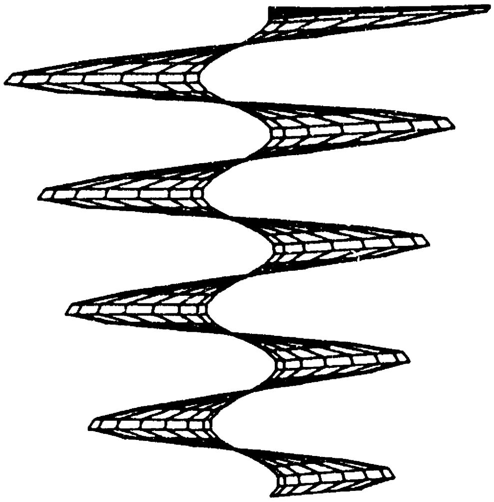

Figure 5.22: Initial prescribed rotor wake geometry.

helicopter rotors. For the purposes of comparison with that larger body of literature, PUF5 was exercised on a simple rotor problem. The rotor consisted of a single blade with a tip radius was 17.5 feet; the root cut-out was 2.33 feet. It had a chord of 1.083 feet, a collective pitch of 10.61° and a linear twist of $-5°$. It was rotated at 355 RPM.

The rotor was panelled with three panels over the chord and seven over the span. Twelve time steps per revolution were used. Each time step was divided into three substeps wherein the singularity strengths were kept constant but the geometry was advanced. Four revolutions per represented in the wake. The problem was started from a steady solution obtained with a prescribed wake geometry shown in Figure 5.22. Forty time steps were carried out. The data presented are for the last time step.

Landgrebe [44] has proposed a wake model based on fitting experimental data which

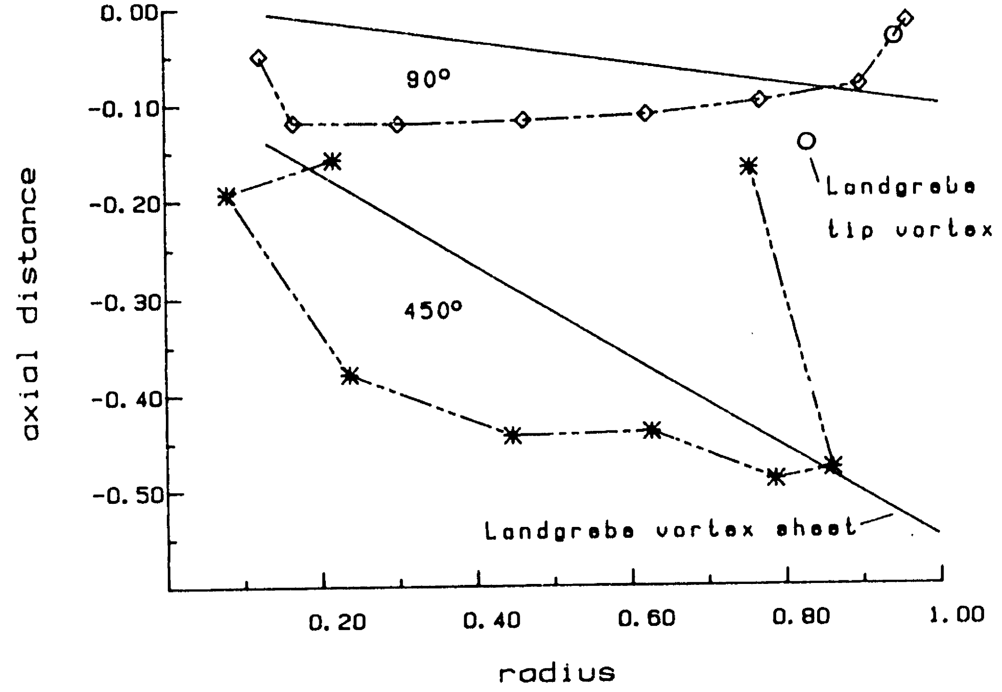

Figure 5.23: Cross-sections of the rotor wake at 90° and 450° behind the first shed vortex compared with Landgrebe empirical model.

is used here as a basis for comparison. Morino, Kaprielian and Sipcic [58], from whom the rotor model was taken, compare their data to the Landgrebe model as well. Figure 5.23 shows a section through the first two turns of the wake at 90° behind the first shed vortex. The outer radii appear well represented but the interior of the sheet seems to suffer from too much downwash. Figure 5.24 reproduces a similar plot from [58]. On balance the two versions are about equal. One notable difference arises from the fact that PUF5 and Morino, *et.al.* use different spanwise arrangements of vortices. Morino, *et.al.* have used half-cosine spacing so that the root panels are quite large. This appears to suppress the tendency of the inboard edge of the sheet to rollup.

Figure 5.25 shows the tip vortex' radial position as a function of rotor angle. Com-

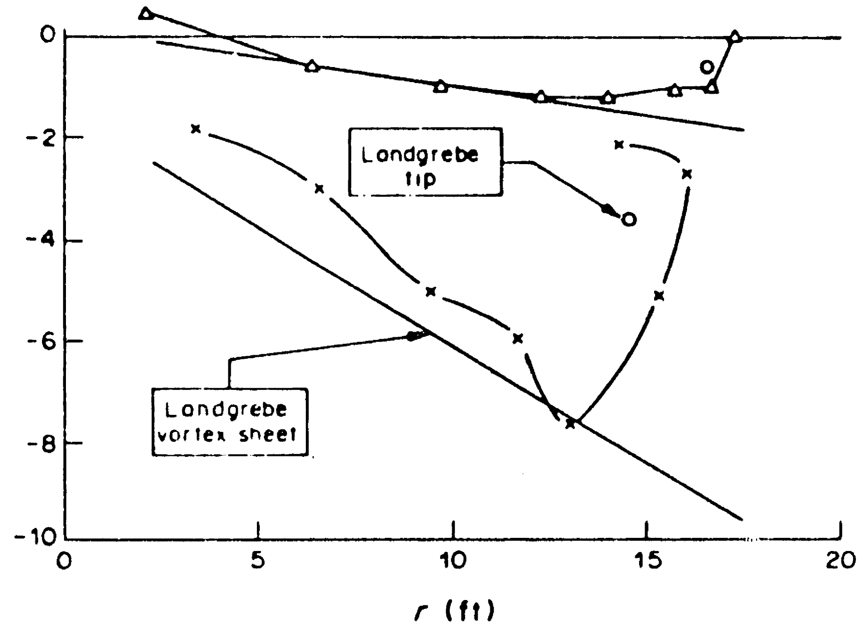

Figure 5.24: Cross-sections of the rotor wake from [58].

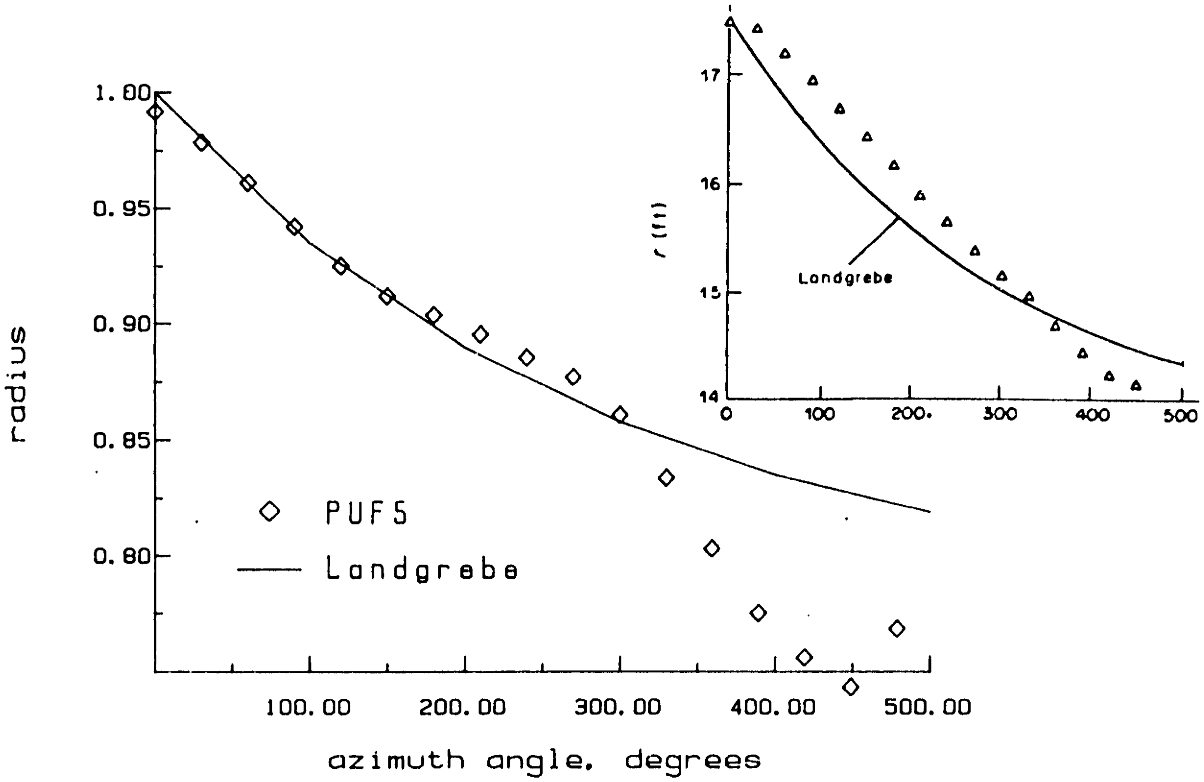

Figure 5.25: Predicted tip vortex radial location compared with Landgrebe's empirical model. Data from [58] are inset.

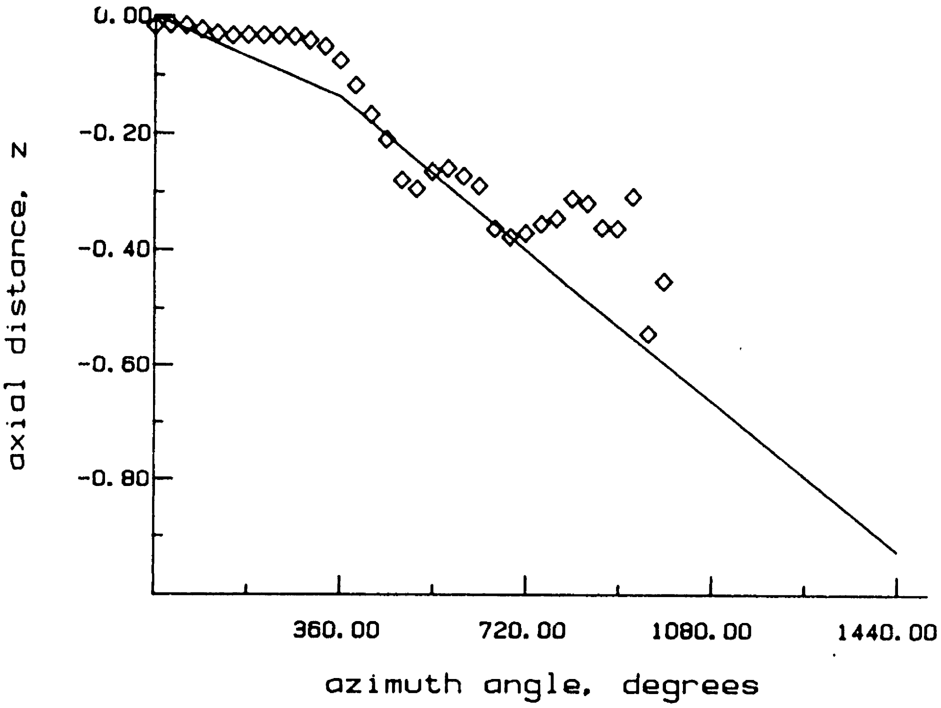

Figure 5.26: Rotor wake pitch compared with Landgrebe empirical model.

parison to Landgrebe's data is excellent up to about 300°. The data from [58] do not match so well. Figure 5.26 makes clear what is happening at 300°. The wake remains well structured for about one revolution but then begins to feel the lack of an ultimate wake model: there is no mechanism to transport the older part of the wake down, away from the rotor. As a result, the downstream end is convected back up into the nearfield, destroying the sheet's coherence. Morino, *et.al.* note the same effect and point out that the length of the coherent part depends on how many turns of the wake are represented.

This backwash effect is even more pronounced at the root radius, especially with the smaller panels used by PUF5. Figure 5.27 shows the wake structure as a function of time. At each time step, the wake is sectioned at the location of every third shed vortex, corresponding nearly to every 90°. The four sets of such sections available at each time step are overlayed. One can clearly see the root and tip vortices being convected back up to the rotor disk where eventually they will be ingested into the upstream end of the

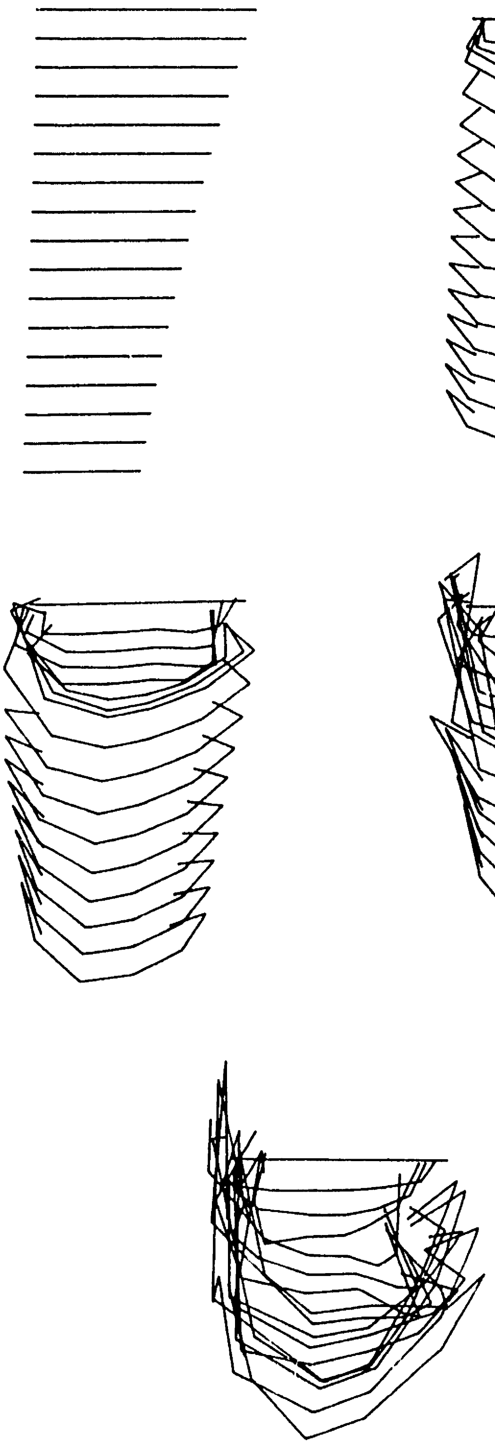

Figure 5.27: Evolution of the wake structure with time.

wake solenoid.

Chapter 6

Conclusions

A vortex lattice representation for marine propellers in unsteady flow has been developed. In doing so, a number of issues which have been lightly regarded in earlier work have been placed into proper perspective. The role of rotationality in the background flow has been described. The assumptions made illuminate the origin of the effective wake problem.

The vortex lattice model is shown to follow naturally from consideration of Green's 2^{nd} identity. By formulating the problem in this way some errors extant in the literature have been uncovered. In particular, the proper calculation of the downwash on the body, and from it, corrected pressure formulae are shown.

The wake model incorporates the effects of local curvature at the edges of the wake sheet. The coupling with the large circulation of the tip vortices makes this important. To avoid the problem of multiple time scales inherent in vortex flows, a simple panel amalgamation scheme is introduced which extends the two-dimensional implementation. This permits the use of comfortably large time steps.

In comparing PUF5's performance to experiments, one is generally encouraged. The wake modelling appears effective. The most apparent inadequacies are readily addressed. Several features could be added to the code to enhance its accuracy. Some are planned for immediate implementation. One expects that thickness effects, particularly cavitation, will be straightforward to implement. A far-wake model is one such feature. A simple source disk representation can be used for conventional flows. Flows with a strong sideways component, as during a turn, will require a more careful treatment. One obvious deficiency of the model is the lack of representation for the hub and shaft. The absence of the potential field they produce leads the root vortices to migrate too far outboard. Coupling a hub representation to a free-wake model will involve repeated re-panelling of the hub surface to allow the adjoining wake panels to respond to the varying inflow.

Another feature which must be added is leading edge separation. One thinks immediately of extending the wake model to allow its separation from the tip- and leading-edges. However, doing so involves all the issues associated with the close approach of the vortices to the body surface. A simpler approach may be to implement the leading edge suction analogy of Polhamus [41;64,65].

The code has been structured to permit easy adaptation. Currently, it is being coupled to MIT's propeller duct model. Eventually, one wants to treat the effective wake problem more carefully. The treatment given here leaves open the opportunity to couple the vortex lattice representation for compact vortical regions with a finite difference Euler or Navier-Stokes representation of the background flow.

Bibliography

[1] D. A. Anderson, J. C. Tannehill, and R. H. Pletcher. *Computational Fluid Mechanics and Heat Transfer.* Hemisphere Publishing, 1984.

[2] H. Aref and E. P. Flinchem. Dynamics of a vortex filament in a shear flow. *Journal of Fluid Mechanics*, 148:477 - 497, 1984.

[3] R. J. Arms and F. R. Hama. Localized-induction concept on a curved vortex and motion of an elliptic vortex ring. *The Physics of Fluids*, 8(4), April 1965.

[4] G. K. Batchelor. *An Introduction to Fluid Dynamics.* Cambridge University Press, 1967.

[5] A. Betz. *Handbuch der Physik*, chapter Tragflugel und Hydraulische Machinen. 1927.

[6] A. Betz. Schraubenpropeller mit geringstem energieverlust. *K. Ges. Wiss. Gottingen Nachr. Math.-Phys. Klasse*, 193–217, 1919.

[7] R . J. Boswell and M. L. Miller. *Unsteady propeller loading — measurement, correlation with theory, and parametric study.* Technical Report Report 2625, David Taylor Research Center, October 1968.

[8] B. Canteloube and C. Rehbach. Calcul des integrals de la methode des singularites. *La Recherche Aerospatiale*, (1), January-February 1986.

[9] A. J. Chorin and P. S. Benard. Discretization of a vortex sheet, with an example of roll-up. *Journal of Computational Physics*, 13, 1973.

[10] G. G. Cox. Corrections to the camber of constant pitch propellers. *Quarterly Transactions of the Royal Institution of Naval Architects*, 103:227 - 243, 1961.

[11] D. E. Cummings. *Vortex interactions in a propeller wake.* Technical Report 68-12, Dept. of Naval Architecture and Marine Engineering, Massachusetts Institute of Technology, June 1968.

[12] F. Durst, A. Melling, and J. H. Whitelaw. *Principles and Practice of Laser-Doppler Anemometry.* Academic Press, 2nd edition, 1981.

[13] J. W. English. *The application of a simplified lifting surface technique to the design of marine propellers.* Technical Report SH R.30/62, National Physical Laboratory, 1962.

[14] O. M. Faltinsen and B. Pettersen. Application of a vortex tracking method to separated flow around marine structures. *Journal of Fluids and Structures*, 1, 1987.

[15] P. T. Fink and W. K. Soh. A new approach to roll-up calculations of vortex sheets. *Proceedings of the Royal Society, London, A*, 362, 1978.

[16] R. E. Froude. On the part played in the operation of propulsion by differences in fluid pressure. *Institution of Naval Architects*, 30, 1889.

[17] O. Frydenlund and J. E. Kerwin. The development of numerical methods for the computation of unsteady propeller forces. *Norwegian Maritime Research*, 5(2), 1977.

[18] H. Glauert. *The Elements of Aerofoil and Airscrew Theory.* Cambridge University Press, 1948. reissued by Dover.

[19] S. Goldstein. On the vortex theory of screw propellers. In *Proc. R. Soc. London Ser. A*, 1929.

[20] T. R. Govindan, R. Levy, and S. J. Shamroth. *Computation of the tip vortex generation process for ship propeller blades.* Technical Report R83-920021-F, Scientific Research Associates, Inc., April 1984.

[21] A. Graber and A. Rosen. A parametric investigation of a free wake analysis of hovering rotors. *Vertica*, 12(1/2), 1988.

[22] D. S. Greeley and J. E. Kerwin. Numerical methods for propeller design and analysis in steady flow. *SNAME Transactions*, 90, 1982.

[23] A. G. Greenhill. A theory of the screw propeller. *Institution of Naval Architects*, 29, 1888.

[24] J. L. Guermond. About collocation methods for marine propeller design. In *Propellers '88 Symposium*, Virginia Beach, VA, September 1988. paper no. 8.

[25] R. Guilloton. Calcul des vitesses induites en vue du trace des helices. *Schiffstechnik*, 4:101–109, 1957.

[26] N. D. Ham. Aerodynamic loading on a two-dimensional airfoil during dynamic stall. *AIAA Journal*, 6(10), 1968.

[27] H. W. M. Hoeijmakers and A. Fokkerweg II. Computational vortex flow aerodynamics. *AGARD-CP-342*, 1983.

[28] H. W. M. Hoeijmakers and W. Vaatstra. A higher order panel method applied to vortex sheet roll-up. *AIAA Journal*, 21(4), April 1983.

[29] T. Hoshino. Application of the quasi-continuous method to unsteady propeller lifting-surface problems. *Journal of the Society of Naval Architects of Japan*, 158:51 —71, 1985.

[30] B. Hunt. *Numerical Methods in Applied Fluid Mechanics*, chapter The Mathematical Basis and Numerical Principles of the Boundary Integral Method for Incompressible Potential Flow over 3-D Aerodynamic Configurations. Academic Press, 1980.

[31] J. Katz and B. Maskew. Unsteady low-speed aerodynamic model for complete aircraft configurations. *Journal of Aircraft*, 25(4), April 1988.

[32] J. E. Kerwin. Private communication.

[33] J. E. Kerwin. Marine propellers. *Annual Review of Fluid Mechanics*, 18:367–403, 1986.

[34] J. E. Kerwin. *The solution of propeller lifting surface problems by vortex lattice methods.* Technical Report, Massachusetts Institute of Technology, 1961.

[35] J. E. Kerwin, W. B. Coney, and C. - Y. Hsin. Optimum circulation distributions for single and multi-component propulsors. In *Twenty-First American Towing Tank Conference*, pages 53–62, 1986.

[36] J. E. Kerwin and C. S. Lee. Prediction of steady and unsteady marine propeller performance by numerical lifting-surface theory. *SNAME Transactions*, 86, 1978.

[37] K.-H. Kim and S. Kobayashi. *Pressure distribution on propeller blade surface using numerical lifting surface theory.* Technical Report DTNSRDC-84/072, David Taylor Research Center, January 1985.

[38] S. Kobayashi. Propeller wake survey by laser-doppler velocimeter. In *Laser Anemometry in Fluid Mechanics*, pages 195 — 209, Ladoan-Instituto Superior Tećnico, Portugal, 1984.

[39] R. Krasny. Computation of vortex sheet roll-up in the trefftz plane. *Journal of Fluid Mechanics*, 184, 1987.

[40] Sir Horace Lamb. *Hydrodynamics.* Dover, sixth edition, 1932.

[41] C. E. Lan. *Extensions of the concept of suction analogy to the prediction of vortex lift effects.* Technical Report CP 2416, NASA, 1986.

[42] C. E. Lan. A quasi-vortex-lattice method in thin wing theory. *Journal of Aircraft*, 11(9), September 1974.

[43] F. W. Lanchester. *Aerodynamics.* London, 1907.

[44] A. J. Landgrebe. *An analytical and experimental investigation of helicopter rotor performance and wake geometry characteristics.* Technical Report USAAMRDL Technical Report 71-24, U. S. Army Air Mobility Research and Development Laboratory, Fort Eustis, VA, 1971.

[45] C. S. Lee. *Prediction of steady and unsteady performance of marine propellers with or without cavitation by numerical lifting surface theory.* PhD thesis, Massachusetts Institute of Technology, May 1979.

[46] J. T. Lee. *A potential based panel method for the analysis of marine propellers in steady flow.* Technical Report 87–13, Dept. of Ocean Engineering, Massachusetts Institute of Technology, July 1987.

[47] H. W. Lerbs. Moderately loaded propellers with a finite number of blades and an arbitrary distribution of circulation. In *SNAME Transactions*, 1952.

[48] T. A. Loukakis. *A new theory for the wake of marine propellers.* Technical Report 71-1, Dept. of Naval Architecture and Marine Engineering, Massachusetts Institute of Technology, May 1971.

[49] B. Maskew. Subvortex technique for the close approach to a discretized vortex sheet. *Journal of Aircraft*, 14(2), February 1977.

[50] J. H. McCarthy. Steady flow past non-uniform wire grids. *Journal of Fluid Mechanics*, 19:491 - 512, 1964.

[51] J. E. McCune and T. S. Tavares. Unsteady 3d aerodynamics of slender wings in severe maneuver. In *AIAA* 1^{st} *National Fluid Dynamics Congress, AIAA-88-3544*, Cincinnati, Ohio, July 1988.

[52] L. M. Milne-Thomson. *Theoretical Aerodynamics.* Dover, fourth edition, 1966.

[53] D. W. Moore. *The discrete vortex approximation of a vortex sheet.* Technical Report AFOSR-1084-69, Cal. Inst. of Tech. Report, 1971.

[54] D. W. Moore. A numerical study of the roll-up of a finite vortex sheet. *Journal of Fluid Mechanics*, 63, 1974.

[55] J. Moran. *An Introduction to Theoretical and Computational Aerodynamics.* John Wiley & Sons, 1984.

[56] L. Morino and B. Bharadvaj. *Two methods for viscous and inviscid free-wake analysis of helicopter rotors.* Technical Report CCAD-TR-85-02, Boston University, Center for Computational and Applied Dynamics, August 1985.

[57] L. Morino and B. K. Bharadvaj. A unified approach for potential and viscous free-wake analysis of helicopter rotors. *Vertica*, 12(1/2), 1988.

[58] L. Morino, Z. Kaprielian, and S. R. Sipcic. Free wake analysis of helicopter rotors. *Vertica*, 9(2), 1985.

[59] D. M. Nelson. *A lifting surface propeller design method for high-speed computers.* Technical Report 8442, NAVWEPS, 1964.

[60] J. N. Newman. *Marine Hydrodynamics.* MIT Press, 1977.

[61] N. Okamura. Experimental analysis of the flow field around a screw propeller. *IHI Engineering Review*, 16(4):296 - 303, October 1983.

[62] R. Peyret and T. D. Taylor. *Computational Methods in Fluid Flow.* Springer-Verlag, 1983.

[63] P. C. Pien. The calculation of marine propellers based on lifting surface theory. *Journal of Ship Research*, 5(2):1 - 14, 1961.

[64] C. E. Polhamus. Predictions of vortex lift characteristics by a leading edge suction analogy. *Journal of Aircraft*, 8(4):193 - 199, April 1971.

[65] E. C. Polhamus. *A concept of the vortex lift of sharp edge delta wings based on a leading edge suction analogy.* Technical Report TN D-3767, NASA, December 1967.

[66] W. J. M. Rankine. On the mechanical principles of the action of propellers. *Institution of Naval Architects*, 6, 1865.

[67] L. Roberts. On the structure of the turbulent vortex. *AGARD-CP-342*, 1983.

[68] T. Sarpkaya. Computational methods with vortices. The 1988 Freeman Scholar Lecture — Presented to ASME Winter Annual Meeting, November 1988.

[69] W. - Z. Shih. *Effective wake calculations by solving the euler equation.* Technical Report 88-2, Dept. of Ocean Engineering, Massachusetts Institute of Technology, March 1988.

[70] W. - Z. Shih. *Propeller performance and tip vortex pitch studies.* Master's thesis, Massachusetts Institute of Technology, May 1985.

[71] J. H. B. Smith. Improved calculations of leading-edge separation from slender, thin delta wings. *Proceedings of the Royal Society, London, A*, 306, 1968.

[72] J. A. Sparenberg. Application of lifting surface theory to ship screws. In *Proc. K. Ned. Akad. Wet. – Amsterdam, Series B*, pages 286–298, 1959.

[73] M. Strscheletzky. *Hydrodynamische Grundlagen zur Berechnung der Schiffsschrauben.* G.Braun, Karlsruhe, 1950.

[74] H. Takami. *A numerical experiment with discrete vortex approximation with reference to the rolling up of a vortex sheet.* Technical Report SUDAER 202, Dept. of Aero. and Astro., Stanford University, 1964.

[75] L. Ting. Studies on the motion and decay of a vortex filament. In *Advances in Fluid Mechanics, Proceedings, Aachen, 1980*, pages 67–105, Springer-Verlag, 1981.

[76] S. Tsakonas, J. P. Breslin, and W. R. Jacobs. Blade pressure distribution for a moderately loaded propeller. *Journal of Ship Research*, 27(1):39 - 55, 1983.

[77] S. Tsakonas, W. R. Jacobs, and P. H. Rank. Unsteady propeller lifting surface theory with finite number of chordwise modes. *Journal of Ship Research*, 12(1):14 - 45, 1968.

[78] F. L. Westwater. *Rolling up of the surface of discontinuity behind an aerofoil of finite span.* Technical Report 1962, Aeronautics Research Council Reports and Memoranda, 1935.